


SAPIENZA
UNIVERSITÀ DI ROMA

Sapienza University of Rome

Department of Physics
PhD in Physics

Thesis For The Degree Of Doctor Of Physics

Analysis and calibration of hyperspectral infrared satellite images

Thesis Advisor
Prof. Michele Ortolani

Candidate
Andrea Massi
1531386

Academic Year 2023-2024 (XXXVI cycle)

Dedico questo lavoro alla mia guida

Introduction

Geomonitoring can be accomplished by in situ measurements, remote sensing on the ground and remote sensing from satellite. Earth Observation (EO) from satellite, in the visible and infrared spectral ranges, is conducted usually with high geometrical resolution satellites, with high spatial resolution up to 30 cm. This high geometrical resolution is achieved with a broad radiometric sampling (low spectral resolution to gain high geometrical resolution). In the extreme case of a panchromatic image, there is no wavelength selection whatsoever, and the intensity at all wavelengths λ in the sensitivity range of the detectors are summed together. This image has a high geometric resolution but a poor information content (all photons are integrated in a single radiometric band), therefore, panchromatic images are typically used to georeference (bind the satellite images on the globe by fixing ground control points) the images produced by the λ-selective bands. The satellites that acquire images in a few (about 8-12) bands, distributed across the electromagnetic spectrum, are called multispectral satellites. These few bands are distributed in the visible and infrared spectrum but do not fully cover a continuous interval, they are also radiometrically broad, therefore preventing any true spectroscopy approach. Spectroscopy is the science of measuring the intensity of light at different wavelengths for the purpose of determining the quality and quantity of matter present.
As an example of multispectral imager, we report in the table below the detector band characteristics of the satellite Landsat 8 [1] of the NASA :

Band	Bandwidth [μm]	Ground resolution [m]
1 - Coastal Aerosol	0.43 - 0.45	30
2 - Blue	0.45 - 0.51	30
3 - Green	0.53 - 0.59	30
4 - Red	0.64 - 0.67	30
5 - near infrared (NIR)	0.85 - 0.88	30
6 - short wavelength infrared (SWIR) 1	1.57 - 1.65	30
7 - short wavelength infrared (SWIR) 2	2.11 - 2.29	30
8 - Panchromatic	0.50 - 0.68	15
9 - Cirrus	1.36 - 1.38	30
10 - thermal infrared 1	10.60 - 11.19	100
11 - thermal infrared 2	11.50 - 12.51	100

Table 1: *Landsat 8 band designations for the two detectors mounted onboard: the VIS-SWIR Operational Land Imager (OLI) and the Thermal Infrared Sensor (TIRS).*

As one can see, the bands are relatively broad, about 10% of the center λ or more. In the case of Landsat 8, the ground resolution is not extremely high (30 m on ground projection), but this is due to the design choice of covering a large area in a single image acquisition (swath width of 185 km), which means that the satellite covers the entire Earth in only 16 days.

Before starting to explain hyperspectral imaging, another multispectral satellite to make an effective comparison should be analyzed, in particular, the ESA's Sentinel 2 [2], which has the following bands of the detector

Band	Central Wavelength [nm]	Bandwidth [nm]	Geom. resolution (m)
1 - Coastal Aerosol	443	20	60
2 - Blue	490	65	10
3 - Green	560	35	10
4 - Red	665	30	10
5 - Red Edge 1	705	15	20
6 - Red Edge 2	740	15	20
7 - Red Edge 3	783	20	20
8 - Near Infrared (NIR)	842	115	10
8a - Near infrared Narrow	865	20	20
9 - water vapor	945	20	60
10 - Cirrus	1380	30	60
11 - shortwave infrared 1	1910	90	20
12 - shortwave infrared 2	2190	180	20

Table 2: *The spectral bands and resolutions of Sentinel-2 Multi-Spectral Instrument (MSI) sensor.*

As it can be seen, the ground resolution of Sentinel 2 is generally better than Landsat 8, reaching 10 m for a few bands, with a smaller swath width of 100 km: this is again a specific design choice, not related to any physical limit. All bands have spectral bandwidth $\geq$ 15 nm and there is no continuous coverage of the electromagnetic spectrum from the blue to the infrared.
It is possible to use the images provided by these λ-selective bands to produce false-color images and classifications (e.g. a normalized difference of two different bands) which may be able to provide highlights of some areas not easily distinguishable in the corresponding true-color images

Now that we have defined what a multispectral satellite is, the hyperspectral satellite used for this work, the "PRecursore IperSpettrale della Missione Applicativa" (PRISMA) satellite of the Italian Space Agency (ASI) can be introduced. PRISMA has a swath width of 30 km and a ground resolution of 30 m: at first sight, it is an extremely inefficient satellite, because it loses (or equates) against both Landsat 8 and Sentinel 2 in both parameters. However, it has a very strong point: it acquires a very large number (239) of narrow bands (9 nm bandwidth) in a continuous range of λ between 400 nm and 2500 nm, enabling spectroscopic studies.
This type of imaging, where each pixel contains a continuous spectrum of λ which can be interpolated and analyzed as a spectral curve (known as spectral signature), is called *hyperspectral imaging*.

Using the PRISMA satellite in the Short Wavelength Infrared (SWIR) region, it is therefore possible to carry out a spectroscopy of the targets within the satellite images, further reducing the gap between the suite of measurements that can be carried out in the laboratory and those carried out by satellites. This is a goal that multispectral satellites cannot accomplish. In fact, multispectral data are not spectroscopy, as it is not possible to detect e.g. vibrational features having only 6 or 12 bands from violet to thermal infrared, while the PRISMA satellite provide continuous spectra usable for characterization and recognition of the structure of matter.
Hyperspectral imaging enables the identification of narrow spectral signatures, like the slope of an electronic transition in a mineral or molecule (e.g. chlorophyll), or the vibrational lines of crystal lattices and molecules, which are chemically specific. The spectral curve of targets, in the visible (VIS) range, can be fairly associated with Earth colorimetry, sensing only a few broad electronic transitions, if any. The vibrational resonances appear instead in the infrared range as narrow quasi-Lorentzian profiles in the Earth reflectance spectra, and their chemically-specific center wavelength can be determined from spectroscopic analysis.

In this work, we focus mostly on minerals. Unfortunately it is not sufficient to increase the spectral resolution of a satellite to be able to perform the same measurements conducted in the laboratory, due to the challenges and technical difficulties typical of satellite imaging compared to the controlled conditions of a laboratory: the presence of the atmosphere, the dependence on sunlight as the only source of radiation, the roughness and orientation of the projection of a pixel on the ground, compared to a laboratory sample that can be mirror-polished and suitably oriented, and the need to install reliable semiconductor sensing technology that does not require cryogenic liquids.
All these effects combined mean that the region measurable by the satellite effectively stops at 2500 nanometers (2.5 microns in wavelength), i.e. at wavelengths much shorter than the typical vibrations in the Long Wavelength Infrared (LWIR) (5 to 20 microns and beyond) where the fundamental vibrations occur.
It should be noticed that the enlargement of the ground pixel projection, to maintain a high signal to noise ratio, could mix too many spectral signatures, both linearly and nonlinearly combined inside each pixel of the satellite image, leading to poor information quality.
The proposed research (spectroscopy from satellite) could be conducted anyway because the vibrational infrared signals (analyzable in the laboratory) in some minerals are promoted to higher energies thanks to promotion phenomena at frequencies higher than the fundamental one. According to the theory of combination bands and overtones, the hydroxyl groups attached to the crystal lattice of silicates, carbonates and sulfates can give a vibrational signal in the SWIR at wavelengths dependent on the crystal lattice structure.

If the attempt to perform satellite infrared spectroscopy is successful, the commercial and environmental applications of this technology in the field of satellite remote sensing would be countless. First of all, it would be possible to apply it in mineral prospecting in remote and extensive territories (mineral mapping) and with great savings in energy and work on the ground. It becomes possible to analyze the state of health of vegetation and agricultural land by identifying the vibrational lines of chlorophyll and water.
In addition to these main applications, this document has added applications of more specialized

interest such as: the mapping of moraines of recently melted glaciers, the mapping of areas covered by volcanic beaches in areas where vegetation is sparse, the mapping of ground movements which brought previously covered subsoil minerals to the surface, the study of the crystalline quality of the construction materials of ancient monuments, and their possible vegetation cover.

The structure of this thesis is as follows: in Chapter 1 we describe the data analysis and calibration problems that the PRISMA mission aims at solving, together with the theory and principles underlying hyperspectral satellite missions prior to and expected to follow the PRISMA mission. In Chapter 2 we enlist the SWIR spectra of most common Earth minerals, which defines the geology background of this thesis. In Chapter 3 we show the hardware (in particular, the design of the PRISMA satellite) and the software (including the software developed in-house by the company NHAZCA srl that co-financed this PhD project) used to produce the original spectroscopy results of this thesis. In Chapter 4 the original results of several experimental campaigns are finally described and discussed. After the chapters, there is a final section that discusses possible future works that can be performed based on the studies conducted in this thesis.

Contents

Chapter 1

Infrared Spectroscopy from a Satellite

This work is an attempt to merge knowledge from physics of the solid state, satellite imaging and geomonitoring.
This effort is valuable because of the recent introduction of hyperspectral imaging satellites. These satellites are able to make the spectral signature of a source of reflected solar infrared radiation on Earth through high spectral sampling of the signal. This is made possible thanks to the phenomena of overtones and combination bands that promote the characteristic photon-phonon interactions (fundamental chemical bond vibrations) that take place in the long-wave infrared (LWIR) 5 - 30 μm up to the operative spectral range of hyperspectral satellites in the short-wave infrared (SWIR) 1 - 2.5 μm.

1.1 Hyperspectral Imaging in the SWIR

Hyperspectral imaging studies the reflectance of the source in a high spectral resolution. The collection of these reflectances, through the spectral operative range of the detector, makes the spectral signature of the source.
Historically, hyperspectral imaging starts from the visible range because it is easier to access and collect photons at this energy level through an optical detector (often with a prism, or a grating, displaced in front of the objective, that separates the signal in each channel of reflectance which constitutes the spectral signature). With the evolution of spectroscopy and physics of solid state, it has become clear that the characteristic signal of the source resides at lower energy (LWIR) where the interaction of photons with phonons appears.
In this way it is possible to efficiently recognize and analyze different kinds of materials in laboratory, however from the satellite it is not possible to access the spectral region beyond the SWIR range. The reasons for this are due to a problem of: i) atmospheric presence (the atmosphere abundantly absorbs radiation at these lower energies), ii) ground resolution (the projection of the detector pixels on the ground must increase to improve the signal-to-noise ratio, but this could result in mixing many different sources in the pixel, which is a severe limitation for almost all Earth Observations). Even though the satellite detector can analyze signals in the SWIR range (wavelengths from 1100 to 2500 nm), one must consider that the detector of the hyperspectral mission of this work is a passive sensor, so it analyzes the intensity of sunlight when it is reflected from the source. Differently from

laboratory, where we have total control of the light source reflected from the sample, in EO we have no control of the illumination in hyperspectral imaging from a satellite as we are forced to use sunlight as illumination. As we can see in figure 1.1 (taken from [3]) sunlight at sea level is well approximated by a blackbody at temperature of 5525 K.
As expected from the Planck's formula in wavelength in eq. 1.1 (where E_λ is the spectral radiance, h the Planck constant, c the speed of light, λ the wavelength, K the Boltzmann constant and T the temperature in Kelvin)

$$E_\lambda = \frac{2hc^2}{\lambda^5} \frac{1}{e^{\frac{hc}{KT\lambda}} - 1} \tag{1.1}$$

the signal in the SWIR spectral range (from $\lambda = 1100$ nm to $\lambda = 2500$ nm) is very low compared to the signal in the visible spectral range.

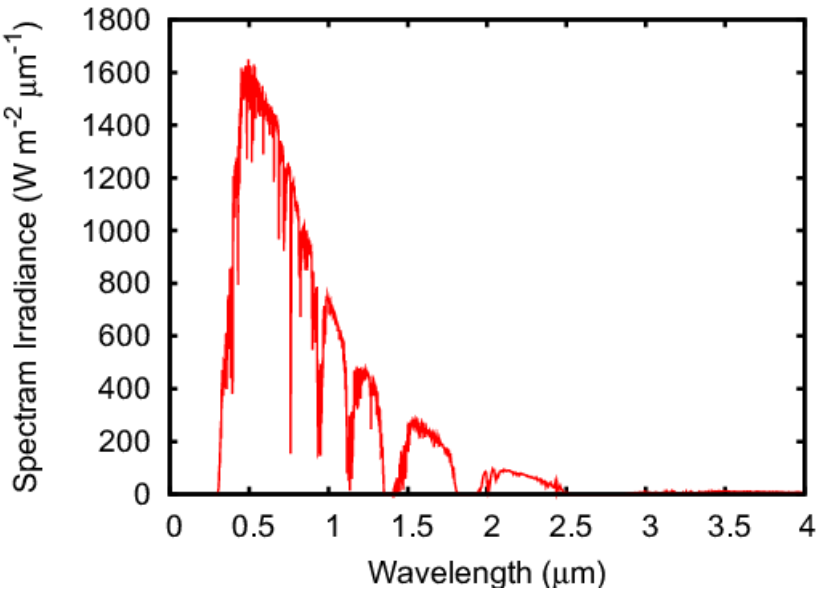

Figure 1.1: *This figure illustrates the solar radiation spectrum for direct light at sea level. The sun emits light with a distribution similar to what would be expected from a blackbody at 5525 K (5252 °C), which corresponds approximately to the surface temperature of the sun. When light passes through the atmosphere, some of it is absorbed by gases with specific absorption bands. The additional light is scattered by Rayleigh scattering, which explains the blue color of the atmosphere. Image from [3].*

1.2 Overtones and Combination Bands

A crystalline structure can be identified optically by analyzing spectral features in the LWIR (wavelengths longer than 5000 nm). In this work, given the fact that satellite detectors do not cover this spectral range but stop at the end of SWIR, we use the energy promotions of these signals due to overtones phenomena and combination bands.
In figure 1.2 it is possible to see the pure signal of the calcium carbonate ($CaCO_3$) at 7016 nm [4] (outside the operative range of PRISMA that stops at 2500 nm) that produces overtones in the crystal lattice, resulting in a signal at $7016/3\ nm = 2339\ nm$ [5].

In vibrational spectroscopy, an overtone band is the spectral band that occurs in a vibrational

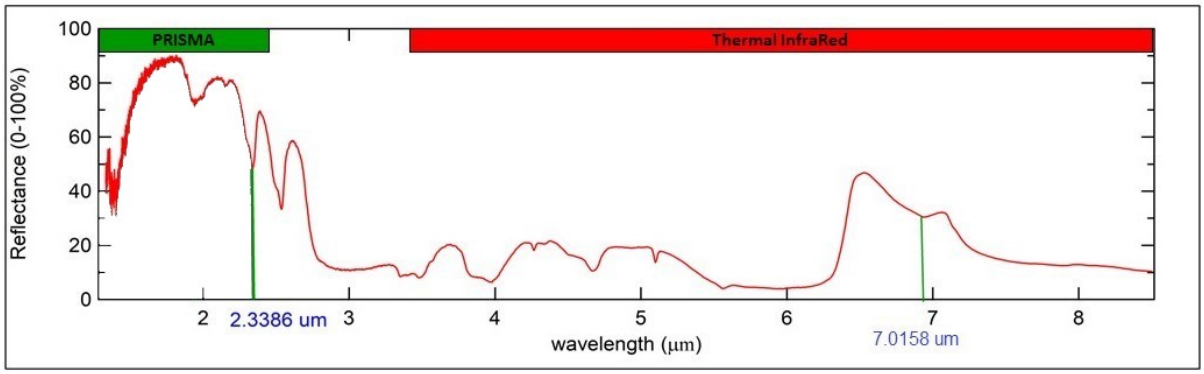

Figure 1.2: *Spectral signature of travertine limestone extracted in laboratory by a Fourier Transform Infrared Spectrometer (see section 3.2)*

spectrum of a molecule when the molecule makes a transition from the ground state ($\nu = 0$) to an excited state ($\nu = n$, with n natural number), where ν is the vibrational quantum number obtained by solving the Schrödinger equation for the molecule. In table 1.1 we can, for example, report the overtones of the Hydrochloric Acid (HCl) in the gaseous phase.

Transition	Term	$\nu_{obs}[cm^{-1}]$	$\nu_{harmonic}[cm^{-1}]$	$\nu_{anharmonic}[cm^{-1}]$
$0 \longrightarrow 1$	Fundamental	2.886	2.886	2.885
$0 \longrightarrow 2$	First Overtone	5.668	5.772	5.665
$0 \longrightarrow 3$	Second Overtone	8.347	8,658	8.339
$0 \longrightarrow 4$	Third Overtone	10.923	11.544	10.907
$0 \longrightarrow 5$	Fourth Overtone	13.397	14.430	13.370

Table 1.1: *Table of Overtones of the diatomic HCl gas phase.*

Generally, to study the vibrational spectra of molecules, it is assumed that the vibrations of chemical bonds are approximated as simple harmonic oscillators (see figure 1.3). Therefore, in the Schrödinger equation, a parabolic potential is used to resolve the vibrational energy eigenstates and their eigenvalues, making these energy states quantized. When electromagnetic radiation is beamed onto a sample, molecules can absorb energy from the radiation and change their vibrational energy

state. However, molecules can absorb energy from radiation only under certain condition, a change in the electric dipole moment of the molecule occurs when it vibrates. This change leads to the transition of the dipole moment of the molecule, from the lowest to highest energy state, respecting the selection rules.
It was experimentally found that the intensity of the overtone band is very low compared to the fundamental band, validating the harmonic approximation, as we can see both from figure 1.3 and the reference [5].
Another phenomenon, in addition to the overtones bands, that raises the vibrational spectral line to the SWIR, is due to the combination bands.
Combination bands are observed when two or more fundamental vibrations are excited simultaneously and consist in the sum of two frequencies involved. The Oxygen-Hydrogen groups (hydroxyl groups OH) contained in the crystal structure of minerals have a stretching vibrational mode that can be excited simultaneously with the pure phonons of the crystal lattice to which they are attached.

In chapter 2 we will list a collection of minerals that show vibrational features in the SWIR spectral range due to the overtones bands or combinations bands.

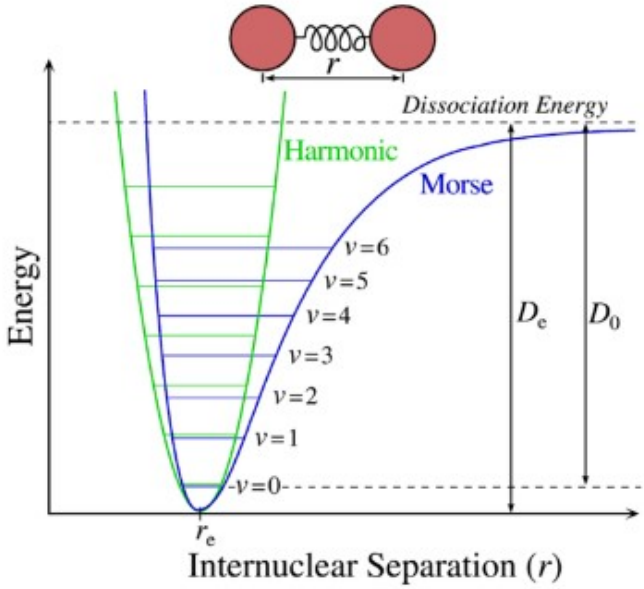

Figure 1.3: *The approximation of the harmonic oscillator (green parabola) superimposed on the anharmonic oscillator (blue curve) on a potential energy diagram. Energy(r) is the potential energy of a diatomic molecule, while r is the radius between the centers of the two atoms. To the left is compression of the bond, to the right is extension. Created by Mark Somoza, March 26, 2006.*

In addition to the result with minerals (described in chapter 2), there are two other relevant examples of overtones and combination bands. The first is represented by the atmospheric absorption bands in the SWIR region (1600 and 1900 nm) for which the atmosphere is completely opaque (this is related to the second overtone of CO_2). The second is represented by the combination of stretching and bending of OH groups in water vapor, that partially overlaps with the second order overtones of CO_2.

1.3 Technical challenges of satellite hyperspectral imaging

One of the most ambitious projects of the PRISMA satellite is enabling the possibility to perform infrared spectroscopy in the laboratory, with the satellite data.
Analyzing the vibrational line (given by the interactions of the mineral exposed to the sunlight) promoted to the SWIR range (due to the phenomena of overtones and combination bands), we try to perform a spectroscopy of the matter in the SWIR range (a spectroscopy in the LWIR range is possible only in laboratory and not from satellite). From recognition of the vibrational spectral features, characteristic of the structure of the crystal lattice of rocks, it is possible to isolate and classify these sources in the hyperspectral imaging of the Earth from satellite.
Of course, if it could be possible to analyze the spectral signature also in the LWIR spectral region, the classification of rocks would be more performing, but it is impossible to maintain a high SNR through the atmosphere with an acceptable geometrical resolution for rocks localization.
Also, it has to be noticed that even if PRISMA acquires continuously from 400 to 2500 nm, there is atmosphere between the source and the detector and, differently from the laboratory, this cannot be removed to extract the spectral signatures. For this reason not only the atmospheric windows prevent the signal from reaching the detector in the 1361 - 1449 nm and 1803 - 1950 nm spectral range, but there are also some other positions (like the features on 1469 nm and 2010 nm) in which a possible vibrational feature of a rock is totally covered by the atmosphere contribution (mainly absorption from carbon dioxide and water).

With this achievement, it is clear that the technical challenge of PRISMA is the spectrometer, since it must face with natural complications that are not present in the laboratory (such as the limitation of using the Sun blackbody as illumination, or the presence of an atmosphere that absorbs the signal in certain ranges of the electromagnetic spectrum) and must attempt to obtain a signal-to-noise ratio at a sufficient level to perform infrared spectroscopy.
To understand why an array of mercury cadmium telluride (HgCdTe) photodiodes composes the PRISMA detector, or how the prism separates the signal into the various wavelengths, the basic principles to understand are i) the detector and ii) the prism.

In the next section we will therefore begin to introduce the concept of the photoelectric effect to explain the photodetectors and, subsequently, understand why the PRISMA detector in the SWIR region is made up of an array of photodiodes.
We will then conclude the chapter with the explanation of the resolving power of a prism to understand why it is mounted on the PRISMA satellite (the presence of the prism in the apparatus is the main reason for the name of the satellite).

1.4 Introduction to optical detectors

The photoelectric effect, discovered by Albert Einstein in 1905, describes how electromagnetic radiations can transfer energy to the electrons in atoms of a material, potentially releasing an electron, and leaving behind a hole. The kinetic energy of the ejected electron is determined by the equation

$E = h\nu - \phi$, where E is the kinetic energy, h is Planck's constant, ν is the frequency of the incident photon, and ϕ is the work function of the material. In the photoelectric effect, photons with sufficient energy can eject electrons from a surface of conducting material if they have sufficient energy to overcome the work function. These ejected electrons can then travel a certain distance, often in a vacuum, and be collected at an anode. The photovoltaic effect is a subcategory of the photoelectric effect. In this effect, photons with enough energy are absorbed by a semiconductor material, creating an electron-hole pair as an electron is promoted from the valence band to the conduction band. These charge carriers, both electrons and holes, can generate a current in a properly designed device with a built-in electric field, and the measurement of the generated electron flow is used to determine the intensity of the acquired optical signal.

In a typical spectroscopic system, a point detector or, more frequently, an array detector, is positioned after a dispersing element. For example, using a diffraction grating that separates the signal into different wavelengths or energy bands, it is possible to measure the intensity of light at each of these wavelengths. This sequential process allows the reconstruction of an entire spectrum. The information obtained is typically a count of incident photons on the detector for each wavelength or energy level. However, the conversion efficiency of photons to electrons and holes is not constant or even linear for all materials across the visible - infrared electromagnetic range. Each detector has a specific conversion curve, which is why it is critical to select the right detector for a particular application. Numerous parameters influence detector performance, including active material, electronic amplification, operating temperature number and size of pixels.
A good detector should exhibit high sensitivity in the frequency range of interest and have the ability to rapidly convert the optical signal to an electrical one while maintaining good signal-to-noise ratio and fidelity.
The relationship between pixel size, charge storage capacity, and voltage applied is a crucial consideration for detectors.

Photodetectors can be categorized into two main types: Point detectors and Array detectors. Point detectors consist of a single detector element and are generally used to measure light at a single wavelength or a narrow band of wavelengths. They are particularly suitable for applications where precise wavelength selection is required. Array detectors, on the other hand, use a matrix of individual sensing elements to simultaneously capture multiple signals over a broader wavelength or energy range. These detectors are advantageous when acquiring a full spectrum or when rapid data acquisition is essential.

Array detectors mounted on the EO satellites are made of semiconductor p-n junctions. In particular in the PRISMA satellite, the material of which the detector is made, in the VIS range, is made up of Cadmium Zinc Telluride (CdZnTe), while in the SWIR range, the material is made up of HgCdTe, a chemical compound that we will analyze in detail in section 1.6. In other satellites, they are often made of Silicon, for VIS range, or Indium Gallium Arsenide (InGaAs) for the SWIR range.

1.5 Array Photodetector

Array photodetectors have become essential when multiple spectral or spatial information needs to be acquired simultaneously, e.g. capturing an entire spectrum at the same moment. Different technologies are available for array photodetectors, Photodiode Array (PDA), complementary metal-oxide semiconductor (CMOS), and Charge-Coupled Device (CCD) detectors. These array photodetectors are commonly used in state-of-the-art spectroscopic instruments because they offer reliability, speed, and long-term stability.

One key advantage of array photodetectors is their ability to read out multiple channels in parallel, which allows a significant amount of data to be acquired within the time frame of a single measurement. This parallel readout capability enables spectroscopic EO.

1.5.1 PDA

Since photodiodes are characterized by very small dimensions, it is possible to arrange multiple photodiodes (each of which acts as a single detector) in the form of an array, to build a single device, which is called Photo Diodes Array (PDA), a sketch of a PDA is reported in figure 1.4.

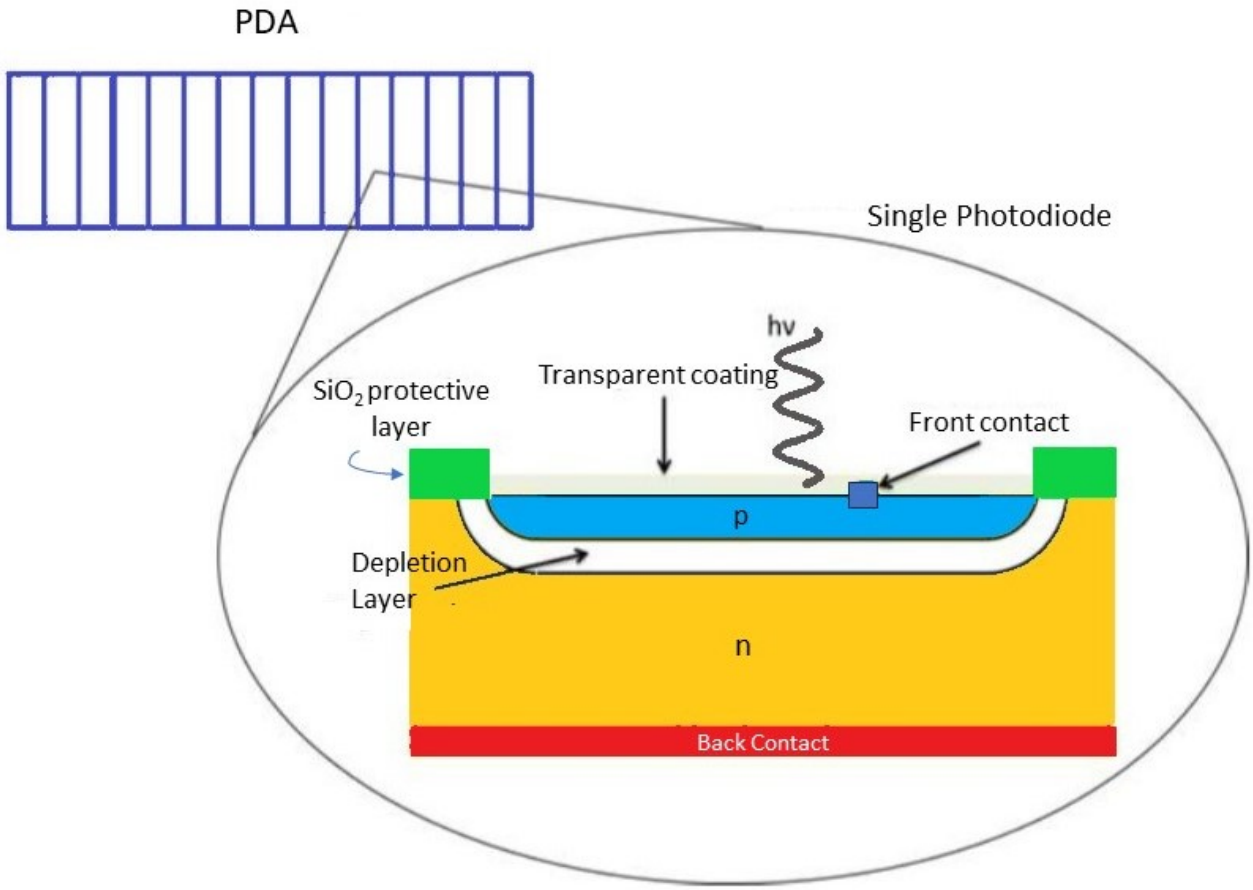

Figure 1.4: *Schematic view of a PDA.*

A PDA is typically a series of detectors lined up in a row. Other geometries can be used, but the linear shape allows for easy and compact detection and encoding of spatial data. Each element is a reverse-biased diode. The incident photons generate charges that exhaust the present charge and the state remains fixed until the next reading cycle. During the read cycle, the state of each photodiode is read and each diode is recharged (the current needed to recharge the diode is actually what we measure). Since the amount of depleted charge depends on the number of photons hitting the detector, and the position of each of them is fixed, each element of the array contains information on the intensity and position of the signal (therefore using a monochromator, like a prism, it is possible to correlate each detector position at a specific wavelength). The spectral response of the array is the same of the single photodiode. For example, for a silicon PDA the working range goes from 200 nm to 1100 nm, with maximum sensitivity at around 650 nm. There are several advantages to using a PDA instead of a single photodiode detector. First, rapid sample fluctuation, that means rapid changes in the sample during measurement, can be analyzed based on an entire spectrum instead of a single wavelength. This can sometimes be decisive: a fluctuation can occur at one moment and not the next. Furthermore, by using a PDA, a systematic system error would impact the entire spectrum and could be easily detected and eliminated. A PDA is the best choice when the goal is to acquire an entire spectrum in the shortest time possible.
In a PDA, coverage and resolution compete, since pixels have fixed positions and sizes. Spectrum acquisition is usually carried out by dispersing the spectrum of interest over the sensitive area of the detector. The higher the dispersion chosen, the better the resolution, but we get less coverage. Therefore, in a multi-channel detector the coverage is given by

$$Coverage\ [nm] = Dispersion\ [nm/mm] \times Width\ of\ detector\ [mm] \tag{1.2}$$

while the resolution is determined by the total coverage and the number of diodes.

$$Resolution\ [nm] = Coverage\ [nm]\ /\ Number\ of\ points \tag{1.3}$$

In the case of PRISMA, the influence of the monochromator (a prism) must be considered, for this reason, the resolution of prism, will be discussed in this work, in the section 1.9.

1.5.2 CCD

CCD is a type of multichannel silicon detector in which individual points are arranged in arrays, typically forming a 2D matrix. CCD detectors are widely used in professional applications where high-quality image data is essential.
Each pixel in a CCD sensor is defined by three electrodes, although only one is required for the actual "potential well". The other two electrodes are needed to transfer the charge. Each electrode overlays the photosensitive semiconducting silicon (p-n junction). A thin silicon oxide layer is deposited between the silicon surface and the electrodes to provide insulation, creating a capacitor. These capacitors are biased to maintain negative potentials around the potential well. This configuration allows electrons generated by incoming photons to be stored in the potential well.
The CCD sensor is then used to read out these stored charges and shift them for conversion into digital values. This process is performed by shifting the charges of each pixel between successive

stages, one at a time. This process can be further detailed in three phases (as seen in Figure 1.5):

Phase 1 (Electron-hole pair generation): Initially, before exposure to light, the pixel is biased in a way that pushes holes away from the substrate, and no mobile electrons are near the surface. When a photon strikes the pixel, it generates electron-hole pairs in the depletion region. The electric field then separates the positive and negative charges, directing electrons to the surface and pushing holes toward the substrate. It's important to note that photovoltaic generation is a nonlinear process, and the generated charge is not linear with respect to wavelength.
Phase 2 (Charge storage): After the electron-hole pairs are generated and separated, the electrons are stored in the potential well. This storage of charge is a crucial step in capturing and preserving the image data.
Phase 3 (Transfer a charge packet from one pixel to the following): After the electrons are generated and confined within the potential well due to the applied positive potential, the process continues with transferring a charge packet from one pixel to the next. This transfer of charge is accomplished by changing the applied potential to different electrodes sequentially. Since the pixels are arranged in columns, the charge accumulated in one row can be transferred to the pixels in the next row at the same time.

Once the charge packets have been transferred through the columns, they are ready for conversion and amplification, typically through an analog-to-digital converter (ADC). This step involves converting the analog charge values stored in the potential wells into digital values that represent the image data. Additionally, CCDs can include amplification stages to enhance the signal before conversion to improve the overall signal-to-noise ratio. This process allows for the accurate capture and storage of image information in a CCD sensor.
Once the charge packets have been sequentially transferred to an output converter, they are then sent to an electrical amplifier. The output signal from the amplifier will be linearly proportional to the amount of charge generated at the photon impact in any pixel. This linearity is a fundamental property of CCD detectors, which makes them well-suited for applications where precise and accurate measurements of light intensity are required. The linear relationship between the input light signal and the output electrical signal is a key feature of CCD technology that contributes to its widespread use in scientific imaging and other applications where high-quality image data is essential.

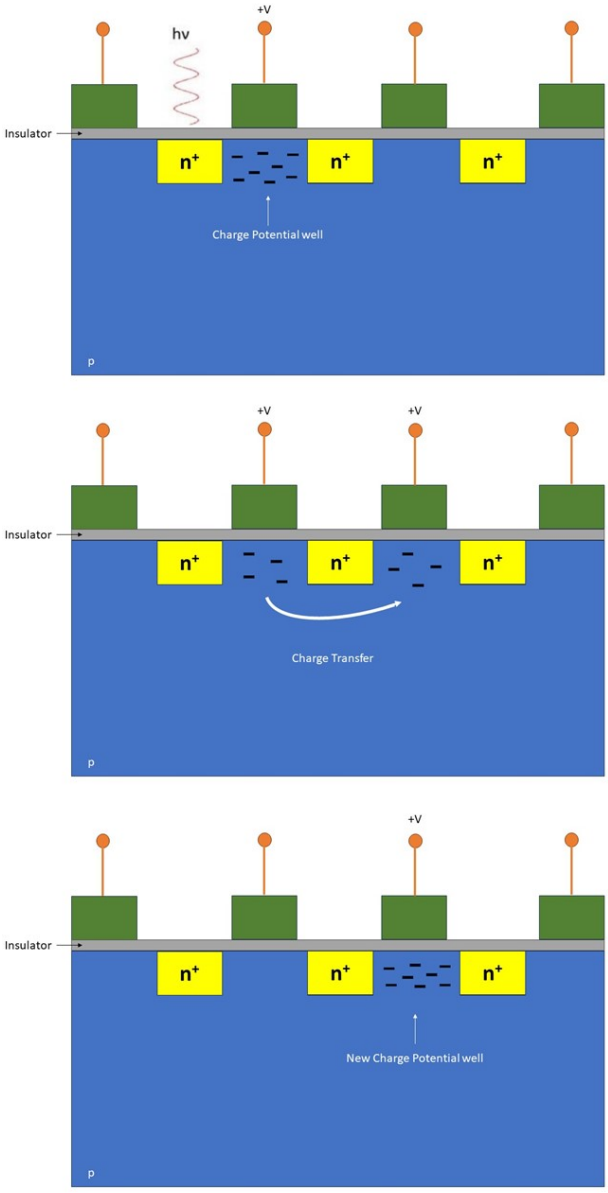

Figure 1.5: *Scheme of charges generation in a CCD and their transfer along bins.*

In CCD detectors, each pixel can be read out individually, providing high-resolution data, or they can be binned together. Binning involves combining the charges from multiple adjacent pixels, typically through software processing, to obtain a more intense signal. This process can enhance the Signal-to-Noise (S/N) ratio, making it easier to detect weaker signals. However, it comes at the cost of reduced spatial resolution because the pixel data are effectively merged.
CCDs come in various architectures and configurations to suit different applications and requirements. The choice of CCD architecture depends on factors such as sensitivity, dynamic range, speed, and resolution needed for the specific application.

1.5.3 CMOS

The CMOS photodetector employs a charge amplifier directly integrated within each pixel (referred to as an active pixel). In contrast to CCDs, it features a solitary amplifier for each photodiode.

Moreover, all the electronic components, including digital logic, clock drivers, and A/D converters, can be incorporated into the same device. The entire pixel array is covered by a grid of metal interconnects to manage timing and readout signals, along with an additional metal interconnect for each column to handle the output signal. The latter is linked to a set of decode and readout electronics, which are positioned outside the pixel array for each column, as depicted in Figure 1.6. This design permits the use of a standard XY addressing technique to read each individual pixel. Historically, this approach was associated with elevated noise levels due to the challenge of achieving precise uniformity among all individual amplifiers (resulting in fixed pattern noise) and the difficulty of controlling dark current at this scale. However, advancements in CMOS technology have led to numerous improvements in CMOS sensors. Initially, noise reduction has been significantly achieved by modifying the amplifier design. Additionally, the size of an individual pixel has been drastically decreased, with the minimum transistor feature size improving from 0.5 μm to 0.18 μm, and even further to 0.09 μm and smaller, resulting in enhanced resolution.

When comparing CCD and CMOS technology, it becomes evident that CMOS offers several advantages due to its integration and low power consumption. While in the past, CCDs outperformed CMOS in terms of noise and dark current levels, this is no longer entirely true with the introduction of new CMOS sensors.

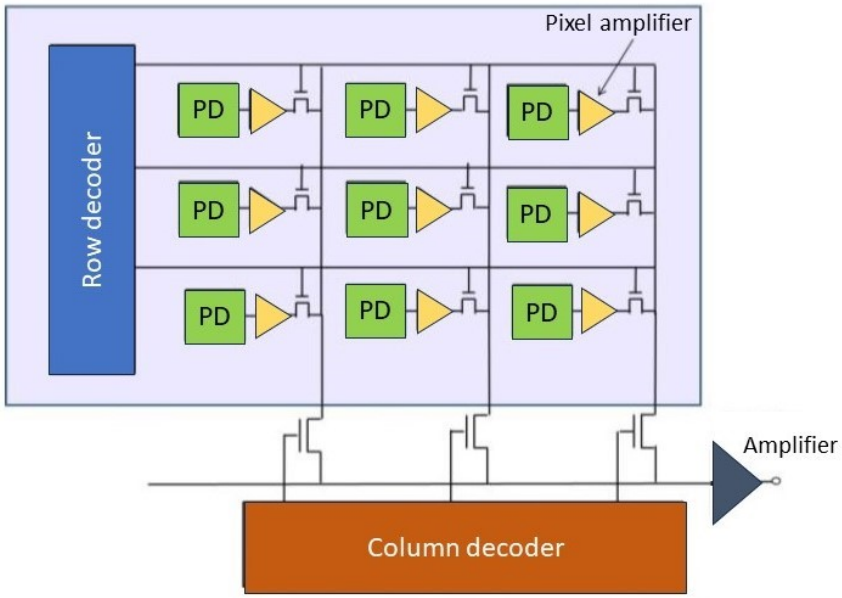

Figure 1.6: *Scheme of a classic CMOS structure.*

At first glance, it might seem advantageous to have smaller pixel dimensions because smaller pixels could potentially lead to higher achievable resolution. However, upon closer examination, this is not necessarily true. In modern spectroscopy, high resolution can often be achieved by choosing a longer spectrometer or a dispersive grating with a higher groove density to disperse light more effectively. This is typically easier than reducing the pixel dimensions of the detector.

1.6 Mercury Cadmium Telluride

To detect signals in the SWIR, as in the case of the PRISMA satellite, it is not possible to use silicon as the material, but it is necessary to use Mercury Cadmium Telluride, which is a chemical compound with a tunable bandgap spanning from the shortwave infrared to the very long wave infrared regions.
Having to use this material, instead of other like silicon, poses a great limitation because it is not possible to build CCD or CMOS entirely composed of HgCdTe. It is for this reason that we are forced to use the HgCdTe detector as an array of p-n junctions made of HgCdTe that is soldered on top of the silicon CMOS read-out circuit to extract spectral signatures in the SWIR region.
The amount of cadmium (Cd) in the alloy can be chosen to tune the optical absorption of the material to the desired infrared wavelength. CdTe is a semiconductor with a bandgap of approximately 1.5 electronvolts (eV) at room temperature. HgTe is a semimetal, which means that its bandgap energy is zero. Mixing these two substances allows one to obtain any bandgap between 0 and 1.5 eV, as we can see from figure 1.7 (left). To be precise, the energy bandgap (E_g) is given by the following formula

$$E_g(x,t) = -0.302 + 1.93\,x + (5.35 * 10^{-4})(1 - 2\,x)t - 0.81x^2 + 0.832x^3 \tag{1.4}$$

where x is Cd concentration in the HgTe semiconductor and t the temperature of the material.
HgCdTe has a zincblende structure with two interpenetrating face-centered cubic lattices offset by (1/4,1/4,1/4) a_0 in the primitive cell. The cations Cd and Hg are statistically mixed on the yellow sublattice while the Te anions form the gray sublattice in the image 1.7 (right).

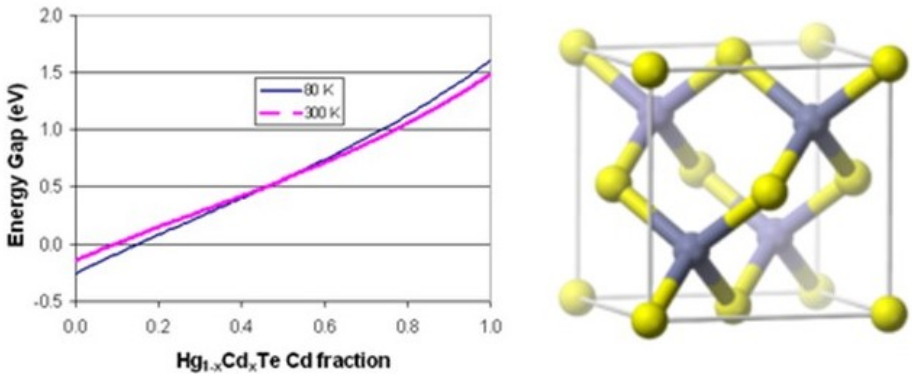

Figure 1.7: *(Left) The variation of energy gap with the cadmium fraction present in the semiconductor as explained by equation 1.4, blue solid curve is at a constant temperature of the material at 80 K, while violet solid curve is at room temperature of 300 K. Created by Jaraalbe, November 27, 2005 (Right) Image of a zincblende unit cell. Created by Benjah-bmm27, May 6, 2007.*

HgCdTe is a soft material due to the weak bonds Hg forms with tellurium transparent in the infrared at photon energies below the energy gap. It is a softer material than any common III-V semiconductor. The Mohs hardness of HgTe is 1.9, CdTe is 2.9 and HgCdTe (with the following fractions: Hg = 0.5 and Cd = 0.5) is 4.
The thermal conductivity of HgCdTe is low; at low cadmium concentrations it is as low as $0.2W/(Km)$.
The specific heat capacity is $150\,J/(kg\,K)$.
In PRISMA satellite, as we will see in the next session, the nominal temperature of SWIR focal

plane is controlled at a stable value in the range 160 to 180 K.

1.7 Cooling impact

The operating temperature of a detector is indeed a critical factor that can significantly impact its performance, especially concerning noise and dark current leakage. Dark current is primarily caused by thermally generated electrons within the detector. The likelihood of generating thermal electrons is directly proportional to the operating temperature, so cooling systems play a crucial role in enhancing a detector's efficiency.

Since the source signal we are interested in this work resides in the SWIR region and the detector is mounted on a satellite, we are more interested in a system that can be remotely controlled to lower or raise the temperature of the Visible-Near Infrared (VNIR) and SWIR detectors to allow measurements in the operating temperature range. As we can see from the figure 1.8, the temperature at which the detectors are kept is between -83 and -100°C.

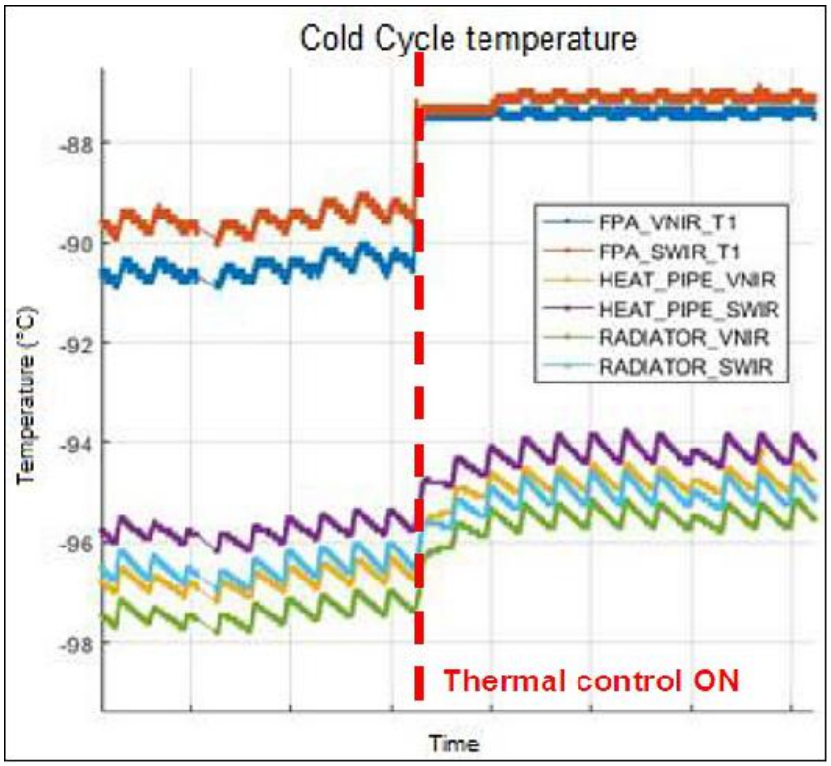

Figure 1.8: *VNIR and SWIR Focal Plane Assemblies (FPA) cold chain temperature control loop performances. As we can see, the thermal monitoring is active on both detectors (FPAs), radiators and the link between them (heat pipes) for each line (VNIR and SWIR).(image credit: Leonardo SpA, ASI).*

For a cooling solution that does not require human presence in situ, thermoelectric cooling can be employed. This method utilizes the thermoelectric effect with different Peltier junctions to "pump" away heat and maintain a lower operating temperature. While not as efficient as liquid nitrogen cooling in reducing dark current, thermoelectric cooling is more accessible and does not

require the frequent refilling of a liquid nitrogen vase of Dewar.

A Peltier junction, or Peltier cooler, is a thin device composed of two separate legs made of heavily doped degenerate semiconductor materials: n-type and p-type, which are connected by a thin copper lamina, as depicted in Figure 1.9. When an electrical potential is applied across these two semiconductors, an electric current flows, and heat is transferred from the lamina above to the lamina below, leading to a cooling effect. It should be noted that by reversing the potential, the reverse effect can be obtained by pumping heat from the lower plate to the upper plate leading to a heating effect that could be necessary for a satellite when, for example, it is in the shadow of the Earth, and the temperature of the detector could go below its operating temperature.

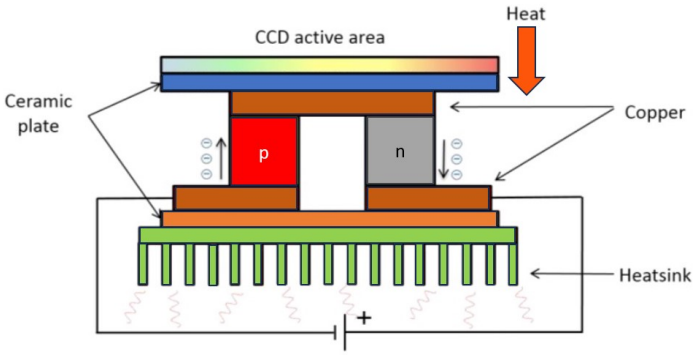

Figure 1.9: *Scheme of a Peltier system.*

1.8 Theoretical limit for photovoltaic detectors and photoconductive detectors

In this section, the fundamental characteristics of a photodetector are mentioned (responsivity, quantum efficiency and noise equivalent power) in order to introduce the concept of specific detectivity. In this way it is possible to show, in one figure, the theoretical performance of a series of infrared detectors and justify the choice of HgCdTe as the material for the detector mounted on the PRISMA satellite.

Responsivity (R) indicates the efficiency of a sensing system in converting input signals into output signals. In the case of a photodetector, it quantifies the electrical response corresponding to the optical input it receives. Typically, the responsivity of a photodetector is indicated in volts per watt of incident radiant power. This measurement varies based on factors such as the wavelength of the incoming radiation and the intrinsic characteristics of the sensor, including the band gap of the photodetector material.
A simple formula for the responsivity of a photodetector, where an optical signal transforms into an electric current (known as a photocurrent), is

$$R = \frac{S}{PA} \quad [\mathrm{V/W}] \tag{1.5}$$

where S is the signal output [V], P the incident energy [W / cm^2] and A is the detector active area [cm^2].
Output signals from photovoltaic detectors are usually extracted as photocurrent, so the R given in terms of the wavelength of the optical signal λ, (R_λ), is expressed in units of A/W.
When light at a given wavelength λ enters a photovoltaic detector, the photocurrent I is expressed by the following equation

$$I = \eta q \frac{PA}{h\frac{c}{\lambda}} = \frac{\eta q P A \lambda}{hc} \quad [A] \tag{1.6}$$

where η is the quantum efficiency indicating the fraction of photon flux that contributes to I when a photodetector is irradiated by photons of a particular wavelength, q is the electron charge, h is the Planck constant and c is the speed of light.

The Noise Equivalent Power (NEP) is the quantity of incident light equal to the intrinsic noise level of a detector. In other words, this is the quantity of incident light when the signal-to-noise ratio (S/N) is 1 in a one hertz output bandwidth (Δf) and its formula is

$$\text{NEP} = \frac{PA}{\text{S/N}\sqrt{\Delta f}} \quad [W/\text{Hz}^{1/2}] \tag{1.7}$$

Detectivity ($D*$) is used to characterize the performance of a photodetector and it is equal to the reciprocal of NEP normalized per square root of A

$$D* = \frac{\sqrt{A}}{\text{NEP}} \quad [cm \cdot \text{Hz}^{1/2}/W] \tag{1.8}$$

To show the theoretical limit of D* we need to consider the noise that occurs when detecting infrared radiation. This noise may come from the infrared detector itself, from its operating circuits or from background fluctuation. Supposing that noise from an infrared detector and its circuits can be ignored in comparison with the noise caused by background fluctuation, the detection limit is determined by only the noise from the background fluctuation. This is called "Background Limited Infrared Photodetection (BLIP)". The BLIPs of photovoltaic detectors and photoconductive detectors are given as follows:

$$D^* \; of \; photovoltaic \; detector: \; D^*_\lambda = \frac{\lambda\sqrt{\eta}}{hc\sqrt{2Q}} \quad [cm \cdot \text{Hz}^{1/2}/W] \tag{1.9}$$

$$D^* \; of \; photoconductive \; detector: \; D^*_\lambda = \frac{\lambda\sqrt{\eta}}{hc\sqrt{Q}} \quad [cm \cdot \text{Hz}^{1/2}/W] \tag{1.10}$$

where Q is the flux of the background radiation.
Figure 1.10 shows the BLIP of background radiation at 300 K when the FOV (field of view) = 180°. As we can see from the figure 1.10 HgCdTe is the only one with a weak dependence of the responsivity on λ in the SWIR range, excluding InSb which however is less reliable.

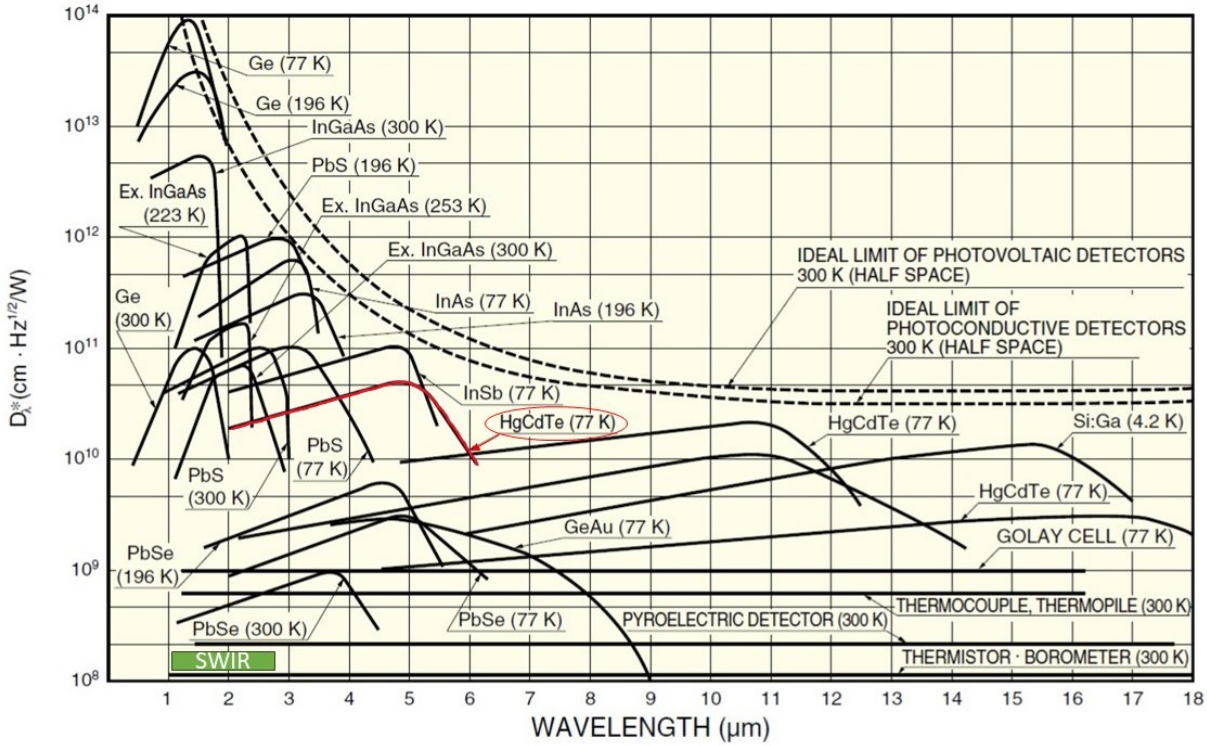

Figure 1.10: *Detectivity curves for various available IR detectors plotted vs. wavelength. Calculated ideal detectivity limits are indicated by dashed lines. The curve of HgCdTe is emphasized to highlight the fact that is sensitive to the SWIR range (in this figure is indicated by a green rectangle). Image taken from [6].*

1.9 Prism Resolving Power

In the PRISMA satellite the detector is a PDA (see section 1.5.1) composed of HgCdTe (see section 1.6). Beyond the signal (that as explained is low in the SWIR range) the resolution in wavelength of the device is based on the prism resolution that has the task to divide the signal in the different channels of analyses. In this case, a prism is used to split the sunlight reflected in 239 distinct bands.

The ability of a prism to resolve two nearby spectral lines is known as resolving power of the prism. It is measured by $\lambda/d\lambda$, where $d\lambda$ is the smallest wavelength difference that can be only resolved by the wavelength λ. In figure 1.11 it is possible to see the scheme that defines the geometry of the resolution of a prism.

For a plane wave front BP of light, we can consider wavelength λ and $\lambda + d\lambda$ as the light incident on the prism ABC, which is placed on the position of minimum deviation. CQ and CQ' are the emergent wavefront for wavelength λ and $\lambda + d\lambda$ respectively, while δ and $\delta + d\delta$ represent their angle of deviation, μ and $\mu + d\mu$ instead are the refractive indices corresponding to wavelength λ and $\lambda + d\lambda$ respectively.

According to Fermat's principle, the optical path between the incident and emergent wavelength for any wavelength must be the same. Hence, for the wavelength λ it is possible to write

$$PA + AQ = \mu BC \tag{1.11}$$

Similarly, for the wavelength λ and $\lambda + d\lambda$ we have

$$PA + AQ' = (\mu - d\mu)BC \tag{1.12}$$

From eq.1.11 and 1.12, we obtain

$$AQ - AQ' = d\mu\, BC \tag{1.13}$$

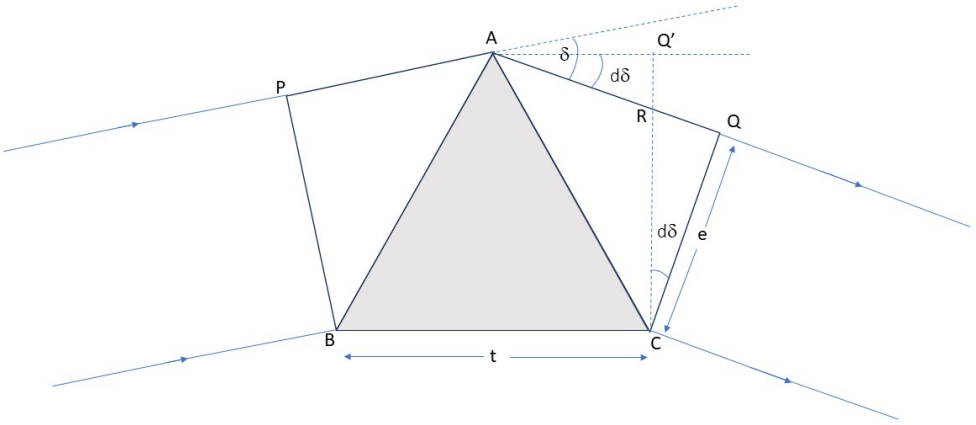

Figure 1.11: *A sketch of the resolution power of a prism*

.

but, from figure 1.11, $AQ - AQ' = RQ$ therefore $RQ = d\mu BC$.

Again from figure 1.11 we obtain

$$\begin{aligned} RQ &= CQ\, d\delta \\ CQ\, d\delta &= d\mu\, BC \end{aligned} \tag{1.14}$$

The emergent beam has a rectangular section. The section may also be considered as a rectangular aperture of width e which is the width of the emergent wavefront CQ.
Hence,

$$e\, d\delta = t\, d\mu \Longrightarrow d\delta = \frac{t\, d\mu}{e} \tag{1.15}$$

Where, t is the width of the base of the prism.
Therefore, the diffraction pattern for each wavelength is equivalent to that due to a rectangular aperture of width e. According to the Rayleigh criterion, if two spectral lines are just resolved, then the principal maximum of one should fall on the principle maximum of the other. It means that the angular separation $d\delta$ between the principal maxima of λ and $\lambda + d\lambda$ must be equal to the angle $d\theta$ between the principal maximum and first minimum of λ. The angle $d\theta$ is given by the Fraunhofer diffraction at a single slit.

$$\begin{aligned} e\ sin\ d\theta &= \lambda \\ e\ d\theta &= \lambda \\ d\theta &= \frac{\lambda}{e} \end{aligned} \tag{1.16}$$

For just resolution $d\delta = d\theta$. So, from eq. 1.15 and 1.16, we get

$$\begin{aligned} \frac{t\ d\mu}{e} &= \frac{\lambda}{e} \\ t\ d\mu &= \lambda \end{aligned} \tag{1.17}$$

Hence, the resolving power of the prism,

$$\frac{\lambda}{d\lambda} = t\ \frac{d\mu}{d\lambda} \tag{1.18}$$

It shows that the resolving power of a prism is directly proportional to the width of the base of the prism, and also proportional to the rate of change of refractive index with wavelength.
As we call $d\mu/d\lambda$ dispersive power, we can say that the resolving power is given by the base of the prism multiplied by the dispersive power of the prism.

Since the HgCdTe array mounted on the satellite was to detect only in the 1100-2500 nm range, a prism is sufficient, hence the choice to use a prism and the name of the satellite itself. As we will see in the next section, AVIRIS and Hyperion, for example, use gratings and not prisms to disperse light into different directions through diffraction instead of refraction allowing a linear dispersion to the formula of resolving power of gratings : $n\lambda = d(sen\theta - sen\theta\ ')$ where n is the order of diffraction, d the distance between grooves, θ the angle of the incident light from the grating normal and $\theta\ '$ the angle of the diffracted light from the grating normal.

1.10 Missions

In this subsection we expose the previous missions about hyperspectral imaging before the launch of PRISMA and the future missions that are in program in the next future.
The era of hyperspectral remote sensing began with the development at the Jet Propulsion Laboratory of the Airborne Imaging Spectrometer (AIS) [7].
The widely used Airborne Visible/Infrared Imaging Spectrometer (AVIRIS) represents the second generation of NASA hyperspectral sensors ([8] - [9]).
AVIRIS was flown for the first time in 1986 (first airborne images) and has been fully operational since 1989. It uses scanning optics and a group of four spectrometers to image a 677 pixel swath width simultaneously in 224 contiguous spectral bands. In airborne and satellite detectors, the swath width indicates the geometrical width of an array of pixel detector projected on the ground during its movement, in this case from an altitude of 20 km, the operating altitude of AVIRIS, means a 12 km of width projection on the ground, which constitutes a 20×20 m of projected ground pixel

resolution.
The detector of AVIRIS consists of 4 different spectrometers that operate at different spectral ranges, their characteristics are illustrated in table 1.2

Parameter	Value	Parameter	Value
Spectrometer A		Detectors of Spect. A	
Spectral range:	360 - 670 nm	Type:	Line array
Number of bands:	32	Number of elements:	32
Bandwidth:	9.7 nm (FWHM)	Material:	Silicon
Grating:	117.65 lines/mm	Integration time:	87.5 µs
Spectrometer B		Detectors of Spect. B	
Spectral range:	660 - 1280 nm	Type:	Line array
Number of bands:	64	Number of elements:	64
Bandwidth:	9.5 nm (FWHM)	Material:	Silicon + InGaAs
Grating:	128.2 lines/mm	Integration time:	87.5 µs
Spectrometer C		Detectors of Spect. C	
Spectral range:	1260 - 1880 nm	Type:	Line array
Number of bands:	64	Number of elements:	64
Bandwidth:	10.0 nm (FWHM)	Material:	Indium Antimonide
Grating:	128.6 lines/mm	Integration time:	87.5 µs
Spectrometer D		Detectors of Spect. D	
Spectral range:	1880 - 2500 nm	Type:	Line array
Number of bands:	64	Number of elements:	64
Bandwidth:	10.0 nm (FWHM)	Material:	Indium Antimonide
Grating:	128.6 lines/mm	Integration time:	87.5 µs

Table 1.2: Characteristics of the four detectors mounted onboard on AVIRIS.

Another mission that is considered very important for its contribution in the hyperspectral imaging before the launch of the PRISMA satellite is Hyperion (decommissioned on March 2017) [10].
The design of the satellite includes a telescope, two grating spectrometers with supporting focal plane electronics, and a cooling system.
This satellite has acquired images by a pushbroom movement, that means that data are collected in each pixel of the satellite image during its movement. In this case, like PRISMA, a four-dimensional hypercube is generated because the satellite acquire the first array of pixel of the image as a three dimensional cube $X \times \lambda \times R$ with X that is position of the satellite image pixel along X axis and $R(\lambda)$ the spectral signature contained in the pixel, and continues to generate data by sliding the three-dimensional cube along the Y axis of the satellite image. With this process, it is possible to obtain a $X \times Y$ satellite image of which each pixel contains a spectral signature $R(\lambda)$.
A dichroic filter in the system reflects the band from 400 to 1000 nm to one spectrometer (VNIR) and transmits the band from 900-2500 nm to the other spectrometer (SWIR).
A focal plane array provides separate VNIR and SWIR detectors. The SWIR detectors are cooled by a cryocooler. The SWIR overlap with the VNIR from 900 to 1000 nm permits cross-calibration between the two spectrometers. Both spectrometers use a JPL convex grating design in a 3-reflector Offner configuration. The VNIR spectrometer uses silicon-diode detectors fabricated in the silicon substrate of a ROIC to provides a 10 nm spectral bandwidth over a range of 400-1000 nm. The SWIR spectrometer has HgCdTe detectors, cooled to 120 K. The SWIR spectral bandwidth is 10 nm. The telescope is a three-mirror astigmatic design, the high-resolution hyperspectral imager is capable of resolving 220 spectral bands (from 0.4 to 2.5 μ m) with a 30-meter resolution. All the mirrors in the system are constructed from coated aluminum, as well the structure holding the optical elements, so that the mirrors and housing all expand and contract at the same rates.

Before conclude this section describing the successor of PRISMA, PRISMA Second Generation (PRISMA2G), it is necessary to introduce some concepts of satellite imaging in order to clarify the improvement of this hyperspectral mission of the future.
As explained in the introduction, one of the biggest problem of the hyperspectral satellites respect the multispectral satellites consists in a lower spatial resolution. Whereas in multispectral imaging a few but radiometrically extended bands are used, hyperspectral imaging uses a much higher number of bands but also necessarily much narrower since the electromagnetic range they must cover remains unchanged. Therefore, to increase the amount of photons collected from each band, one possible solution is to enlarge the ground projection of the detector pixel mounted on the satellite. The result is a satellite image (raster) that is, however, due to the fact that it is composed of larger pixels and therefore a smaller amount of pixels for the same area framed by the satellite, at a lower geometric resolution. This mode of acquisition that generates an image of $X \times Y$ dimensions without holes and projected onto the globe is called “Stripmap.”
However, this is not the only way to increase the signal-to-noise ratio. An alternative method that allows results with relatively high spectral resolution but without losing geometric resolution is to increase the exposure time. This can be done during pushbroom (as explained in this section, it is the acquisition of data by satellite motion and it is necessary to produce the hypercube $X \times Y \times R \times \lambda$) by curving the satellite during its trajectory, so that it frames the same point

on the ground for more time. The image that is generated in this way will be composed of small areas (spots) that will no longer be of low geometric resolution but will be separated from each other by non-acquisition gaps (no data) and will no longer result in a continuous $X \times Y$ image, but will instead generate a $X \times Y$ matrix with hyperspectral data spots and acquisition gaps. This acquisition method is called "Spotlight".
PRISMA2G will perform the passage of the spectral resolution to 10 meters (thanks to the new "Spotlight" way of acquisition that increase the exposure time producing spot images instead of the classic rasters produced with "Stripmap" at 30 m of ground resolution).
This new function pioneers for hyperspectral technology, and will increase the quality and quantity of the data collected, and the new mission will be able to send back about 3 terabytes of hyperspectral images per day, effectively more than 10 times the capacity of its predecessor.

Chapter 2

Geology Background

In the VNIR spectral range, hyperspectral imaging could retrieve useful information that is widely used in Earth Observations (both as pure data and as data fusion with other remote sensing data). Some of these results will be discussed in Section 4.7 in which a hyperspectral imaging technique is used on a green site of a cultural heritage (Appia Antica Regional Park) to perform a colorimetry of the vegetation to measure and establish its health.
However, information on this spectral range could not give any information about structural crystal lattice and for this reason the main work of this thesis does not involve the works on the VNIR range of hyperspectral satellite. They involve instead works about the SWIR spectral range, in which it is possible to observe vibrational features of minerals, as we will now explain.
The signals of the reticular vibration of rocks due to the sunlight exposure, resides in the LWIR spectral range. Even if this signal is very important and characteristic of the sample considered (it could be decisive in operations like localization and identification of rocky areas in satellite image, mineral mapping), it is not possible to perform any kind of analyses in this spectral range (due to the atmospheric absorption and geometrical resolution explained before).
Anyway, it is possible to analyze these signals when they are promoted to higher energy (moving to the SWIR spectral range) due to the phenomena (see subsection 1.2) of overtones of pure phonons or combination bands between pure phonons and hydroxyl groups attached to the crystal lattice.

In figure 2.1 (taken from [11]) we can see a collection of rocks that show vibrational features in SWIR spectral range due to the overtones bands and combinations bands.

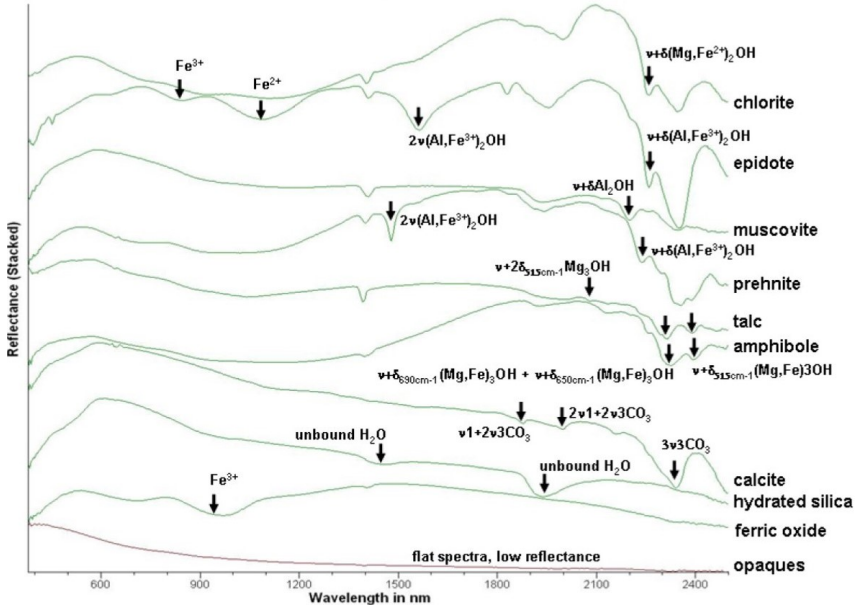

Figure 2.1: *A collection of rocks with vibrational spectral features in SWIR. In the notation: ν represents stretching of the OH group in respect to the structure, that is indicated in brackets, δ denotes bending, $\nu + \delta$ indicates the combination of stretching and bending, 2ν indicates the first overtone of the stretching fundamental, and 3ν refers to the second overtone of the stretching fundamental. Image taken from [11].*

The context of this thesis is about Earth Observations, with a particular focus on the detection and identification of rock species due to the spectral features in the SWIR range (obtained from overtones and combination bands of the pure signal in the LWIR range).
The objective of this section is to provide an overview of the functional groups present in rock-forming minerals, which give rise to diagnostic absorption features in the SWIR.
Functional groups are clusters of molecules that play a crucial role in fundamental vibrations within the mid and far-infrared spectra, consequently influencing combinations and overtones in the short-wave infrared range (1000 - 2500 nm). They serve as a key to understanding absorption features by establishing connections between absorption patterns and the chemical composition, as well as the crystallographic structure of a mineral.

Absorption bands associated with bending and stretching vibrations of key rock-forming minerals, including hydroxylated silicates, carbonates, and sulfates, manifest in the mid and far-infrared spectral range. In di-octahedral phyllosilicates, exemplified by white mica, stretching fundamentals are situated approximately between 3642 cm^{-1} (2746 nm) and 3581 cm^{-1} (2793 nm), while bending vibrations occur around 924 cm^{-1} (10823 nm). Shortwave infrared absorption features primarily stem from overtones of stretching vibrations and combinations of stretching and bending vibrations. Calculations for combinations of the stretching and bending fundamentals of the $Al_2 - O - H$ feature, crucial for di-octahedral phyllosilicates like muscovite, paragonite (4566 cm^{-1} or 2190 nm), and phengite (4505 cm^{-1} or 2220 nm), align with experimental results (refer to [12] for a summary). The first overtone of the $Al_2 - O - H$ feature appears in the 7100 cm^{-1} (1400 nm) region, exhibiting a shift to longer wavelengths compared to the double frequency of the stretching fundamental vibrations due to the anharmonic behavior of the OH-group ([13]).
In the range of solar reflected light (0.3-3 μm), numerous minerals exhibit distinctive absorption bands attributed to vibrational overtones, electronic transitions, charge transfer, and conduction

processes. For a comprehensive understanding of the origins of these absorption features, [14] provides an excellent review. The spectral characteristics of minerals have undergone extensive examination (e.g., [15],[16] and [17]). In the literature, there has been a focus on studying the nonlinear effects arising from mineral mixtures (e.g., [18]; [19]; [20] and [21]).

The term "high spectral resolution" should be interpreted within the specific context of this study. While the resolution employed in satellite measurements (9 nm for PRISMA) may not be considered high when evaluated against all standards of laboratory (less than 0.6 nm), it stands out when compared to reflectance spectra commonly published in the geological communities. The maximum resolution reported in this study is akin to what can be achieved in reflectance with standard commercial Fourier Transform Infra-Red (FTIR) spectrometers.
This study serves as a survey focusing on narrow absorption features in minerals. Given the impracticality of showcasing spectra for all minerals within the constraints of a single paper, a representative fraction is presented to provide an illustrative overview.
Broad absorption bands observed in the visible and near-infrared regions are commonly attributed to electronic transitions, such as ligand field and metal-metal charge transfers (for a comprehensive review of absorption processes, see [14]). The absorptions originating from OH^-, H_2O, and CO^{2-}, noticeable in the 0.9 to 2.5 μm range, result from overtones and combinations of fundamentals that manifest at longer wavelengths.
Successive higher overtone or combination absorption bands inherently possess strengths approximately 30-100 times weaker than their respective lower overtone, combination, or fundamental vibrations bands. However, in reflectance, where a lower absorption coefficient allows photons to penetrate more material, the observed band strength tends to be enhanced (e.g., [22]; [23]). Band saturation effects introduce scattering conditions that can result in combinations and overtones exhibiting stronger apparent band depths than the fundamentals (e.g., [22]; [21]).

2.1 Water and Hydroxyl in Minerals

The water molecule exhibits three infrared-active fundamental vibrations absorptions that are shown in table 2.1 in units of Frequency, Wavelength, Energy and Pulsation.

	Frequency (ν)[cm^{-1}]	Wavelength (λ) [nm]	Energy ($h\nu$)[eV]	Pulsation (ω)[Hz]
Conversion between quantities	1000	10000	0.12	$2.99 * 10^{13}$
Symmetric OH stretch	3651	2738	0.45	$1.09 * 10^{14}$
Asymmetric OH stretch	3755	2663	0.46	$1.12 * 10^{14}$
H-O-H bend	1595	6269	0.19	$4.78 * 10^{13}$

Table 2.1: *Table of conversion and of the three infrared-active fundamental vibrations absorptions of the water molecule. The first row indicates the conversion between the different units of Frequency, Wavelength, Energy and Pulsation.*

In its free state, there is a symmetric OH stretch, denoted as ν_1, at 3651 cm^{-1}, an asymmetric OH stretch, ν_3, at 3755 cm^{-1}, and an H-O-H bend, ν_2, at 1595 cm^{-1}. In H_2O gas, these absorptions manifest as multiple closely spaced bands due to combinations with rotational modes. Moreover, in the SWIR, combination bands reveal rotational fine structure on the milliangstrom scale.
In liquid water, rotational fine structure is absent, and the bands shift to $\nu_1 = 3219cm^{-1}$, $\nu_3 = 3445cm^{-1}$, and $\nu_2 = 1645cm^{-1}$. In ice, the bands undergo further shifts to $\nu_1 = 3221cm^{-1}$, $\nu_3 = 3400cm^{-1}$, and $\nu_2 = 1650cm^{-1}$. These shifts in band positions are attributed to hydrogen bonding. The absence of rotational fine structure in both the liquid and solid phases is attributed to the molecule's inability to rotate.
In the SWIR, the isolated water molecule exhibits absorptions at 1.875 μm ($\nu_2 + \nu_3 = 5333cm^{-1}$), 1.454 μm ($2\nu_2 + \nu_3$), 1.379 μm ($\nu_1 + \nu_3$), 1.135 μm ($\nu_1 + \nu_2 + \nu_3$), and 0.942 μm ($2\nu_1 + \nu_3$) [15].
In minerals, water exhibits combination and overtone bands near these positions. Water can be physically adsorbed on the surfaces of mineral grains or occupy specific lattice sites (e.g., beryl), or it can be an integral part of the crystal structure (e.g., gypsum). The water bands may appear sharp, as observed in well-ordered sites in beryl, or broad due to multiple or poorly ordered sites, as seen in montmorillonite. The presence of a band at 1.9 μm indicates the presence of molecular water in the sample. Conversely, the absence of a 1.9 μm band but the presence of a 1.4 μm band indicates the presence of only OH-groups, which is often a component of the crystal structure of a mineral.
There is a common notion that the OH stretch typically occurs around 2.78 μm (3600 cm^{-1}). The first overtone generally manifests itself near 1.4 μm ($2\nu_{OH}$ 714 cm^{-1}), while the second overtone occurs close to 0.95 μm ($3\nu_{OH}$ or 10500 cm^{-1}).
In layered silicates, the range of the OH stretching vibration is reported to be 3400-3750 cm^{-1} (2.94 - 2.67 μm). The frequency of the OH vibration is correlated with the specific site it occupies. For instance, in common chain, ribbon, and ring silicates, the absorption band position is linked to the

electronegativity difference between Mg and another cation when the cation substitutes into the Mg site [24].
The fine structure in the OH stretching region was initially observed by [25] in the transmission spectra of natural talc. Four closely spaced bands were identified and interpreted as arising from mixed (Mg, Fe) talc. These bands are attributed to hydroxyl groups linked to Mg_3, $Mg_2 + Fe$, $Fe_2 + Mg$, and Fe_3. Similar bands are observed in other minerals containing (Fe, Mg) and hydroxyl. Apart from absorption related to the OH stretch, hydroxyl-bearing minerals exhibit absorptions due to OH librations in the range of 400 - 1200 cm^{-1} (25-8 μm), and translation vibrations of OH near 300-700 cm^{-1}. In-plane librations (bending) are detailed in Table 2.2.

Species	Wavelength [μm]	Frequency [cm^{-1}]
Al_2OH	11-9.8	909.1-1020.4
$Fe^{3+}AlOH$	11.2	892.8
$MgAlOH$	11.9	840.3
$Fe^{3+}OH$	12.2	819.6
$Fe^{2+}Fe^{3+}OH$	12.5	800
$MgFe^{3+}OH$	12.5	800
Mg_2OH	17-15	588.2-666.7

Table 2.2: *Table of hydroxyl bending in most common layered silicates.*

Combination vibrations involving the OH stretch and metal-OH bend are observed in the 2 - 2.5 μm region (5000-4000 cm^{-1}). It is generally recognized in the literature that if a band occurs near 2.2 μm (4500 cm^{-1}), it is attributed to AlOH; at 2.3 μm (4300 cm^{-1}), it is associated with MgOH [14].
Understanding the positions of the fundamentals is crucial. Minerals displaying fine structures in the OH stretching region are expected to exhibit fine structure in the overtone regions as well. The overtone regions may be more complex due to the involvement of vibrational and translational modes. However, overtones generally tend to be more intense than a combination of overtone and combination bands because more modes are involved.

Fine structure is not as prominently detected in the bending regions of fundamentals as observed in the OH-stretching fundamental vibrations region. Bending vibrations typically have a broader width than the OH stretches. A combination of OH stretch and metal-OH bend may not necessarily exhibit the fine structure observed in the OH stretch region, as the broader bending modes can potentially obscure the details of the combination stretch-bend absorption bands.

2.2 Phyllosilicates

For the rest of the chapter, minerals that present vibrational characteristics in the SWIR will be described.

Di- and tri-octahedral phyllosilicates represent a significant group of rock-forming minerals that exhibit distinctive absorption features in the SWIR. These phyllosilicates are categorized into five major groups based on their layer structure: i) Di-octahedral 1:1 phyllosilicate ("7Å phase"): e.g., kaolinite, ii) Tri-octahedral 2:1 phyllosilicate ("9Å phase"): e.g., talc, iii) Di-octahedral 2:1 phyllosilicate ("10Å phase"): e.g., muscovite, phengite, celadonite, iv) Tri-octahedral 2:1 phyllosilicate ("10Å phase"): e.g., biotite, v) Tri-octahedral 2:1:1 phyllosilicate ("14Å phase"): e.g., chlorite.
This classification is partially derived from [26], which summarizes four principal layer types of phyllosilicates: 1/1, 2/1, and 2/1/1 patterns (Figure 2.2, Figure 2.3). It is extended by considering the number of octahedral sites filled in the respective phyllosilicates, providing important information about the infrared functional groups contained.

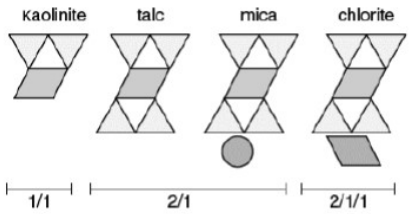

Figure 2.2: *Schematic representation of the four layer types of phyllosilicates 1/1, 2/1 and 2/1/1 patterns [26]. Grey triangles represent tetrahedral layer; gray rhombus represent octahedral layer; gray circle represent interlayer cation. Image taken from [11].*

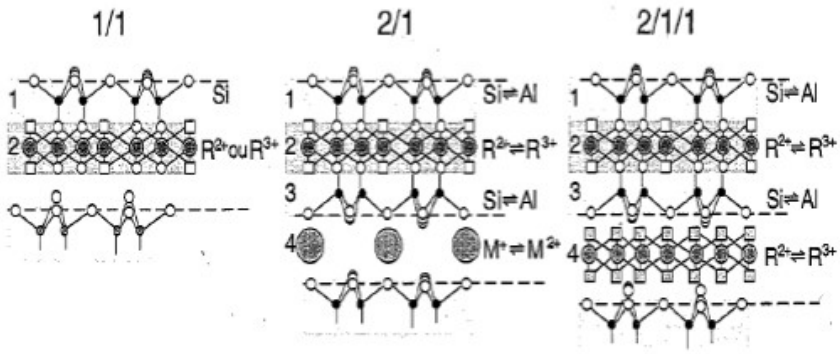

Figure 2.3: *Cationic planes of three different layer types of phyllosilicates (from [26]). 1/1 minerals have two cationic planes, one tetrahedrally coordinated (1) and one octahedrally coordinated (2). 2/1 minerals contain three cationic planes ("9Å phases"), and an additional fourth cationic layer (interlayer sheet) when the structure is not electrically neutral ("10Å phases"). The difference between the di-octahedral (e.g. muscovite) and tri-octahedral (e.g. biotite) "10Å phases" is represented by the vacant third cation site in the di-octahedral phyllosilicates. 2/1/1 minerals have two tetrahedrally and two octahedrally coordinated layers. The octahedral layer 4 is also often referred to as the "brucite-layer", whereas the combination of layers 1, 2 and 3 is referred to as the "talc-layer". Image taken from [11].*

The five layer types and the various combinations of these types in interlayered phyllosilicates contribute to a diverse array of absorption bands in the SWIR.
Discussion here focuses on the combination bands related to the main functional groups of di- and tri-octahedral phyllosilicates in the SWIR.
Kaolin group minerals, serving as the primary representatives of di-octahedral "7Å-phases," exhibit a distinctive doublet with a prominent feature fixed at approximately 4530 cm^{-1} (2209 nm) and a secondary feature at around 4630 cm^{-1} (2160 nm) [27]. This doublet can be deconstructed into four absorption bands, where the three shorter wavelength ones are associated with the stretching vibration of the inner hydroxyl groups ($\nu + \delta Al_2OH_i$, hydroxyl groups bonded to the tetrahedral layer, see Figure 2.2), and the major long-wavelength one is linked to the stretching vibration of the outer hydroxyl group ($\nu + \delta Al_2OH_o$) [27]. Variations in the shape of this characteristic doublet correspond to changes in the structure and crystallinity of kaolin group minerals [28].
Kaolin may also exhibit a weak to medium absorption feature at 4468 cm^{-1} (2238 nm) related to $\nu + \delta(AlFe^{3+})2OH$, with intensity increasing as the ferric iron content rises.
Talc belongs to the group of tri-octahedral 2:1 phyllosilicates ("9Å phase"). The general composition of talc can be expressed as $Si_4O_{10}M_3(OH)2$, with exclusive occupancy of the M-sites by Mg in the talc endmember and substitution of Mg by ferrous iron in minnesotaite. In pure talc, a characteristic doublet is observed in the 2320 nm wavelength region, comprising the combination of stretching at 3676 cm^{-1} (2720 nm), with bending at 650 cm^{-1} (15384 nm) and 690 cm^{-1} (14492 nm), respectively. The resulting absorption bands are located at 2300 and 2279 nm, respectively, overlapping with the Mg-rich endmembers of the actinolite (see figure 2.9 left) and hornblende series due to their structural similarity. Additionally, the third major absorption band of talc at about 4200 cm^{-1} (2380 nm) ($\nu + \delta(M)_3OH$ where $\delta(M)$ refers to the bending of frequency $515cm^{-1}$) overlaps with Mg-rich amphiboles such as tremolite. To distinguish talc from these amphiboles, a weak triple feature (2077/2127/2172 nm), characteristic of talc, can be utilized.

Di-octahedral 2:1 phyllosilicates ("10Å phase") constitute a significant group encompassing white

micas (e.g., paragonite, muscovite, phengite, celadonite) as well as smectites (e.g., montmorillonite). The predominant absorption feature in these AlOH-bearing phyllosilicates arises from ($\nu+\delta Al_2OH$). Octahedral Al can undergo substitution by Fe^{2+} or Mg (R^{2+} in Figure 2.3), and the associated charge imbalance is compensated by the exchange of tetrahedral Al with Si.
A remarkable fact is that interlayer cations in mica (Figure 2.3) do not influence the position of the combination features [12]. Therefore, the differentiation between Na-micas (e.g., paragonite) and Na-void micas (e.g., muscovite) is not feasible with non-laboratory-based infrared spectrometers. Smectites exhibit a similar shift in the Al-O-H absorption band, where beidellite represents the Al-rich smectites, and montmorillonite represents the Al-poor smectites. However, smectites and mica-like minerals with the same octahedral composition display a different location of the OH-absorption bands—located at shorter wavelengths (approximately 2200) for smectites and longer wavelengths (around 2220) for illite ([29] - [12]). Therefore, in the interpretation of AlOH-bearing samples, the mineral should be initially identified as mica before determining the octahedral composition. Another diagnostic absorption feature of white micas is situated at 4255 cm^{-1} (2350 nm) (Figure 2.4), absent in smectites and thus useful for distinguishing between the two mineral groups. This absorption feature becomes more prominent with increasing contents of ferrous iron or Mg.

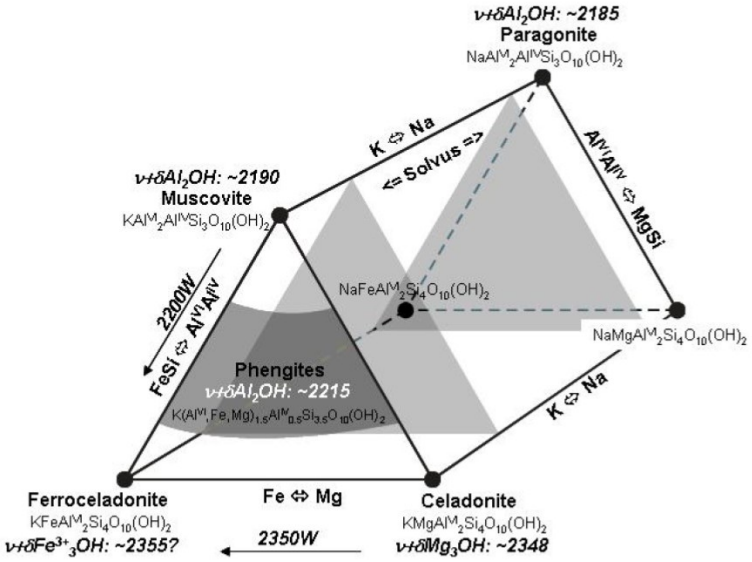

Figure 2.4: *The mineral space of mica-like di-octahedral 2:1 phyllosilicates ("10 Å phases") is characterized by the locations of major absorption features, with values obtained from various sources, including [30], and content of this section. The major absorption features are highlighted in italic. Image taken from [11].*

Di-octahedral 2:1 phyllosilicates, exemplified by muscovite, differ from tri-octahedral 2:1 phyllosilicates (e.g., biotite) by having a vacant third cation site. In contrast, both tri-octahedral 2:1 phyllosilicates ("10Å phase") and tri-octahedral 2:1:1 phyllosilicates ("14Å phase"), such as chlorites, exhibit characteristic absorption features at approximately 4444 cm^{-1} (2250 nm) and 4274 cm^{-1} (2340 nm). In chlorites, the $\nu+\delta(Mg, Fe^{2+})_2OH$ (interlayer OH-related vibrations or brucite-layer) shifts from about 2248 nm to 2261 nm from the clinochlore to the chamosite endmember, respectively. Additionally, the $\nu + \delta(Mg, Fe^{2+})_3OH$ (inner OH of 2:1 talc layer) at around 2350 nm can shift based on the Mg content of chlorite. In contrast to chlorites, the shorter wavelength feature in biotite is attributed to $\nu + \delta([AlFe^{3+}], [AlMg])_2OH$.

Kaolinite, as shown in figure 2.6 (left) and figure 2.10 (left), exhibits a well-known doublet absorption near 2.2 μm. Similarly, halloysite, depicted in figure 2.6 (left) and figure 2.10 (left), also displays a similar doublet.
In halloysite, the absorption bands near 2.2 μm occur at nearly the same location as in kaolinite: 2.16 and 2.207 μm (4630 and 4531 cm^{-1}). The position of the longer band varies within the samples measured, ranging from 2.207 to 2.206 μm. However, the 2.16 μm band is too broad, making it challenging to accurately define its band center and observe small shifts. Near 1.4 μm, the broad component of the doublet absorption is shifted to around 1.390 μm (7190 cm^{-1}) or slightly shorter, to 1.388 μm (7205 cm^{-1}) in some halloysite samples compared to kaolinite. The other absorption shifts shortward to between 1.414 and 1.413 μm (7072 and 7077 cm^{-1}). Both of these halloysite absorptions are broader than the corresponding kaolinite bands.
The observed variation in the halloysite band positions and widths may reflect the degree of disorder. The degree of disorder in kaolinites has been shown to cause band shifts in this mineral. For additional discussion, refer to [29].

Illite, as seen in figures 2.9 (right) and 2.10 (left), muscovite, depicted in figures 2.9 (right) and 2.10 (left), and montmorillonite (Figures 2.5 (left)) exhibit similar absorption bands without fine structure.
Illite and muscovite feature additional absorption bands near 2.35 and 2.45 μm, which are absent in montmorillonite. The 2.45 μm (4080 cm^{-1}) absorption in illite is poorly defined, and the shorter band is located at 2.34 μm (4270 cm^{-1}). Therefore, it is possible to distinguish the three minerals from each other. For example, montmorillonite has no 2.34 or 2.35 μm absorptions, illite has a band at 2.34 μm, and muscovite has one at 2.35 μm. However, a resolution of about 0.005 μm (or better) is required to distinguish illite from muscovite.
In remote sensing, the 2.2-μm band is often weak, and the other absorption bands may be below detection limits. In such cases, the three minerals cannot be reliably distinguished.

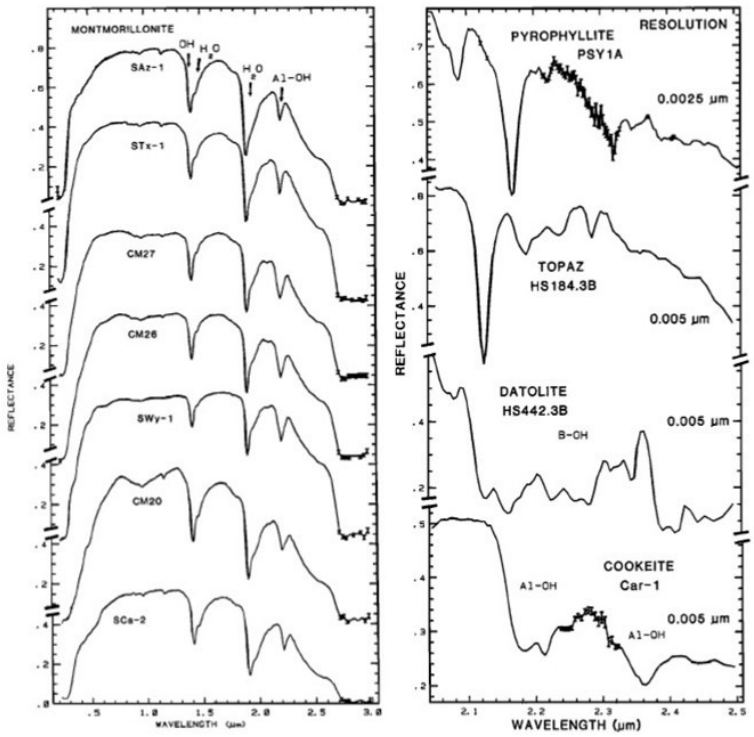

Figure 2.5: *(Left) Absorption features in montmorillonite near 2.2 μm. (Right) SWIR Absorption features in pyrophyllite, topaz, datolite and cookeite. Image taken from [31].*

2.3 Sorosilicates

Of the family of sorosilicates, we can consider the epidote. The epidote series constitutes a solid solution range extending from clinozoisite ($Ca_2Al3Si3O_{12}(OH)$) to pistasite ($Ca_2Fe^{3+}Al_2Si_3O_{12}(OH)$). Each OH-group in epidote is connected to two M-sites, and these sites are occupied by varying amounts of Al and Fe3+. In the literature, two major hydroxyl bending fundamentals are situated at 1045 cm^{-1} (9569 nm) and 975 cm^{-1} (10256 nm), respectively (for references, see [32]). The combination of these bending fundamentals with the primary stretching vibration positioned at 3365 cm^{-1} (nm) [33] occurs at 4410 cm^{-1} (2267 nm) and 4255 cm^{-1} (2350 nm), respectively.
The first overtone of the main stretching fundamental vibrations in epidote is situated around 6450 cm^{-1} (1550 nm). [34] utilized the wavelength position of this first overtone ($2\nu(Al, Fe^{3+})2OH$) to make inferences about the distribution of epidote series minerals in hyperspectral drill core data from the Eastern Goldfields. Specifically, they distinguished between clinozoisite ($\geq$ 1552 nm) and epidote ($\leq$ 1552 nm).
Some OH absorption bands in minerals occur at longer wavelengths. For instance, O-H absorptions near 3450 cm^{-1} (2.9 μm) are observed in jarosite (Figure 2.6 Right panel), and at 3550 cm^{-1} (2.82 μm) in tourmaline (Figure 2.7 Left). Additionally, three bands at 1.357, 1.409, and 1.548 μm are likely OH overtones. Notably, the two bands at 2.254 and 2.339 μm (4437 and 4275 cm^{-1}) are attributed to the combination of OH stretches with a Fe-OH bend, and they are remarkably intense features.

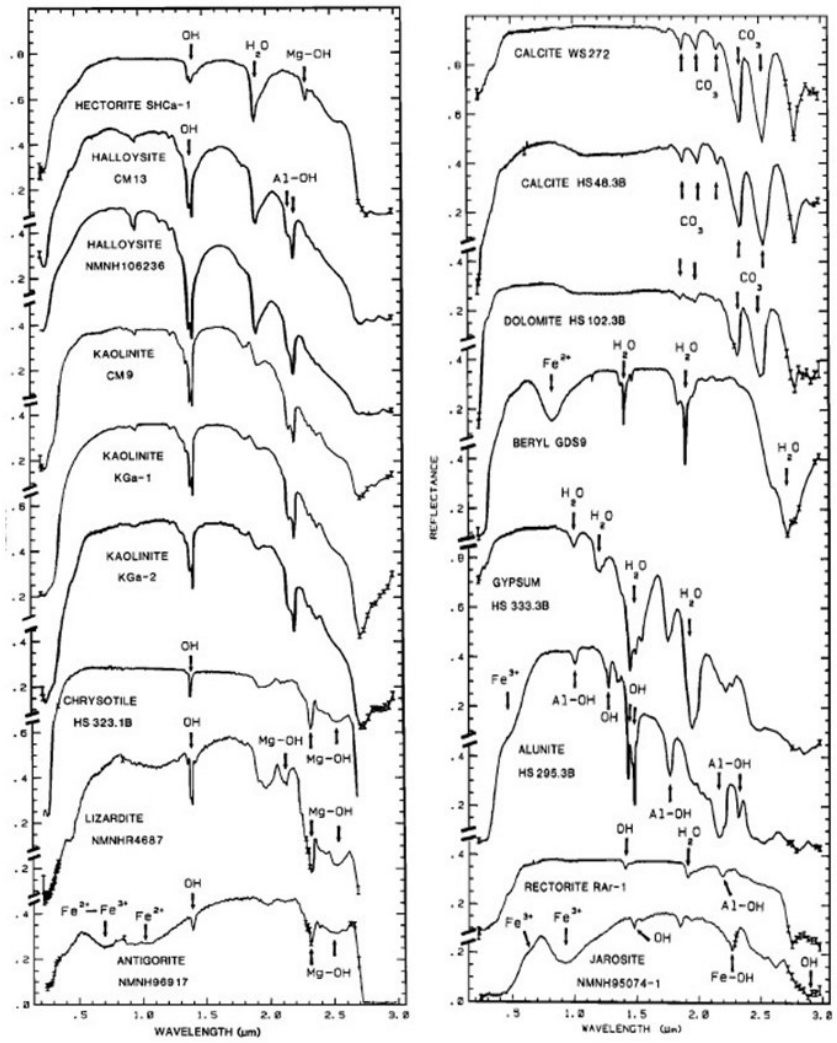

Figure 2.6: *(Left) Reflectance spectra at the standard 1X resolution ranging from 0.2 to 3.0 μm for hectorite, halloysite, kaolinite, chrysotile, lizardite, and antigorite. (Right) Reflectance spectra at the standard 1X resolution ranging from 0.2 to 3.0 μm for calcite, dolomite, beryl, gypsum, alunite, rectorite, and jarosite. Image taken from [31].*

2.4 Inosilicates

Amphiboles are the exclusive inosilicates considered in this document and are categorized into various amphibole series based on internationally accepted recommendations: i) actinolite series (e.g., tremolite, actinolite), ii) hornblende series, iii) alkali amphiboles (e.g., riebeckite), iv) Fe-Mn-Mg amphiboles (e.g., cummingtonite).
However, this classification may not always be fully applicable when interpreting SWIR absorption features. Major SWIR absorption features of amphiboles occur in the 2320 nm and 2380 nm wavelength region, overlapping with di- and tri-octahedral phyllosilicates containing ferric iron, as well as talc and kaolinite.

In the actinolite (figure 2.9 left) and hornblende series, the first main absorption feature at 4348 cm^{-1} (2320 nm) can be decomposed into eight bands. These bands are attributed to combinations of hydroxyl stretching fundamentals ranging from 3673 cm^{-1} (2723 nm) (νMg_3OH) to 3625 cm^{-1} (2759 nm) ($\nu Fe_2 + 3OH$), with two major bending fundamentals located at 690 cm^{-1} and 650

cm^{-1}.

A doublet around 2320 nm can be observed, for example, in Mg-rich endmembers of the actinolite series, while actinolites with an intermediate Mg number exhibit a broad feature in the same wavelength range. The second main absorption feature, located around 4200 cm^{-1} (2380 nm), is possibly related to the combination of the main hydroxyl stretching fundamentals with a bending vibration at 525 cm^{-1}. The positions of these two major absorption features are primarily linked to the abundance of Mg and Fe^{2+} occupying the M1 and M3 sites. These are the only cation sites connected to the OH group responsible for the respective absorption bands [35].

As mentioned earlier, some minerals exhibit four bands in the OH stretching region, corresponding to OH linked to Mg_3, Mg_2Fe, $MgFe_2$, and Fe_3. In the case of tremolite, actinolite, and talc, they all display an absorption near 1.392 μm (7184 cm^{-1}), attributed to Mg_3. Tremolite, being the Mg endmember in the tremolite-ferroactinolite solid solution series, does not exhibit OH bands involving Fe. The band around 1.398 μm (7153 cm^{-1}) is due to Mg_2FeOH, and the bands near 1.404 μm (7120 cm^{-1}) are associated with MgFe2OH. These samples do not contain enough iron to prominently display the Fe_3-related band, except extremely weakly, and it occurs near 1.412 μm (7082 cm^{-1}).

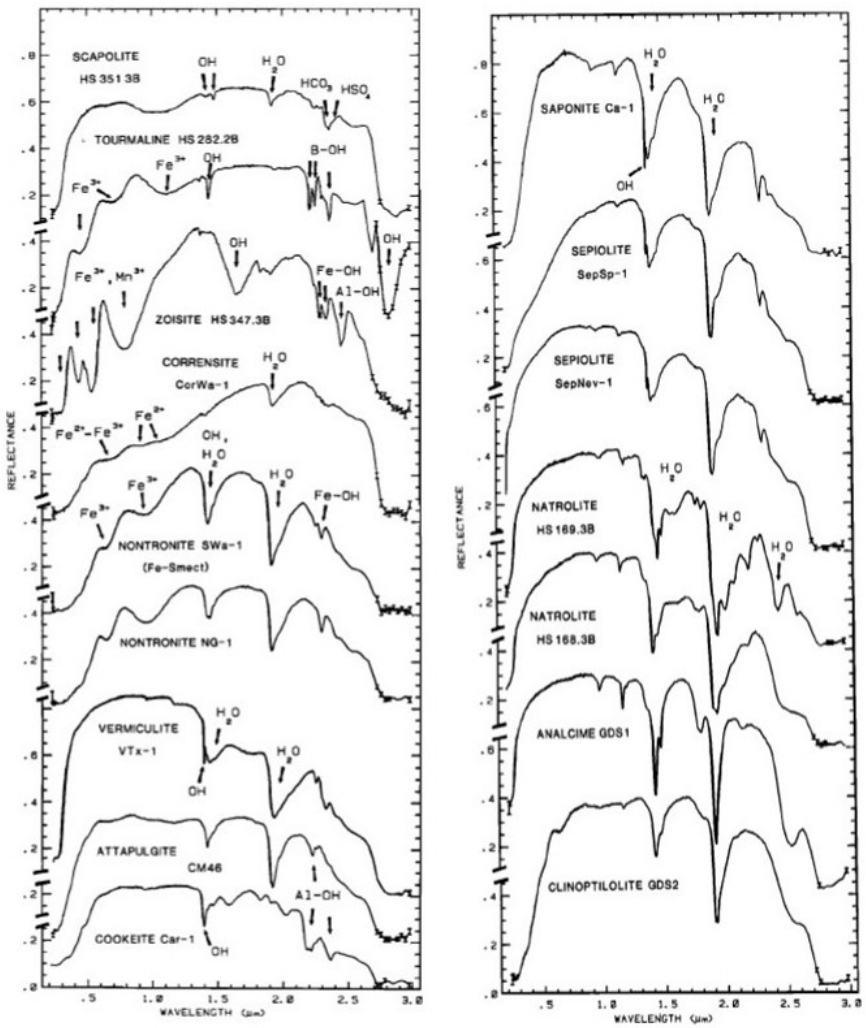

Figure 2.7: *(Left) Reflectance spectra at the standard 1X resolution ranging from 0.2 to 3.0 μm for scapolite, tourmaline, zoisite, corrensite, nontronite, vermiculite, attapulgite, and cookeite. (Right) Reflectance spectra at the standard 1X resolution ranging from 0.2 to 3.0 μm for saponites, sepiolite, atrolite, analcime, and clinoptilolite. Image taken from [31].*

2.5 Carbonates

Carbonates exhibit several diagnostic absorption features in the SWIR, which undergo significant changes in location and shape, primarily depending on the amount of Mg, Fe, and Mn replacing Ca. Figure 2.8 illustrates a composition space of major carbonate minerals. The main diagnostic absorption feature in the SWIR ($3\nu\ CO_3$; for a summary, see [36]) is positioned between 4273 cm^{-1} (2340 nm) and 4348 cm^{-1} (2300 nm) and displays a characteristic left-hand asymmetry (Figure 2.1), indicating a secondary, smaller feature on the short-wavelength limb, likely centered in the 2230 - 2275 nm wavelength region. With an increasing amount of Mg and Fe, the $3\nu\ CO_3$ shifts to shorter wavelengths ([36]). The $3\nu\ CO_3$ feature and its secondary associated feature can be simulated by a mineral mixture comprising materials featuring $\nu + \delta[Al, Fe^{3+}]$ / $[Mg, Fe^{2+}]2OH$ (e.g., di- and tri-octahedral phyllosilicates) and $\nu + \delta[Mg, Fe^{2+}]3OH$ (e.g., amphiboles).
Figure 2.1 also emphasizes two other medium to weak but diagnostic absorption features in calcite, located at around 5025 cm^{-1} (1990 nm) and 5350 cm^{-1} (1870 nm), respectively.

These two features always appear as pairs in carbonates and, although decreasing in intensity with increasing Mg or Fe content, they also exhibit a blue-shift with the increasing replacement of Ca by Mg and Fe. Due to their overlap with the major OH/H_2O feature at around 1900 nm, these features can be obscured but prove to be very useful when the true nature of a left-hand absorption feature in the 2340 nm region is questionable.

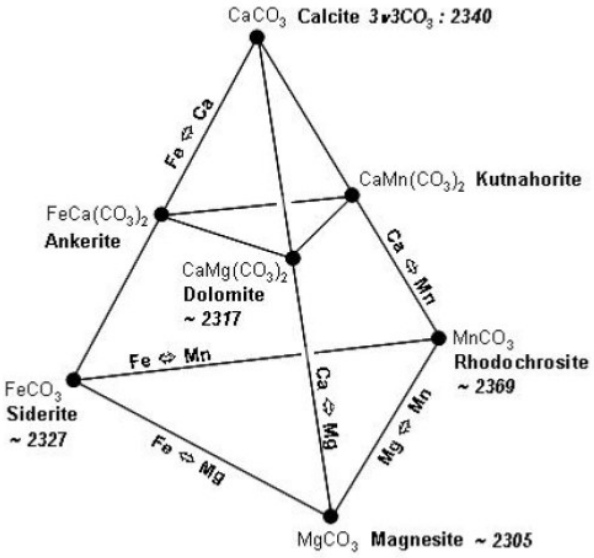

Figure 2.8: *The composition space of major carbonates is depicted, illustrating exchange vectors that relate end members for these minerals (modified after Spear, 1993).Image taken from [11].*

In carbonates, the observed absorptions are attributed to the planar CO_3^{-2} ion. There are four vibrational features in the free CO_3^{-2} ion: the symmetric stretch $\nu_1 = 1063\,cm^{-1}$ the out-of-plan bend $\nu_2 = 879\,cm^{-1}$, the asymmetric stretch $\nu_3 = 1415\,cm^{-1}$ and the in-plane bend $\nu_4 = 640cm^{-1}$. Combination and overtone bands of the CO_3 fundamentals occur in the short wavelength IR. The two strongest are $\nu_1 + 2\nu_3$, at 2.50-2.55 μm (4000-3900 cm^{-1}) and $3\nu_3$, at 2.30-2.35 μm (4350-4250 cm^{-1}; e.g., see the calcite in Figure 2.6 right).

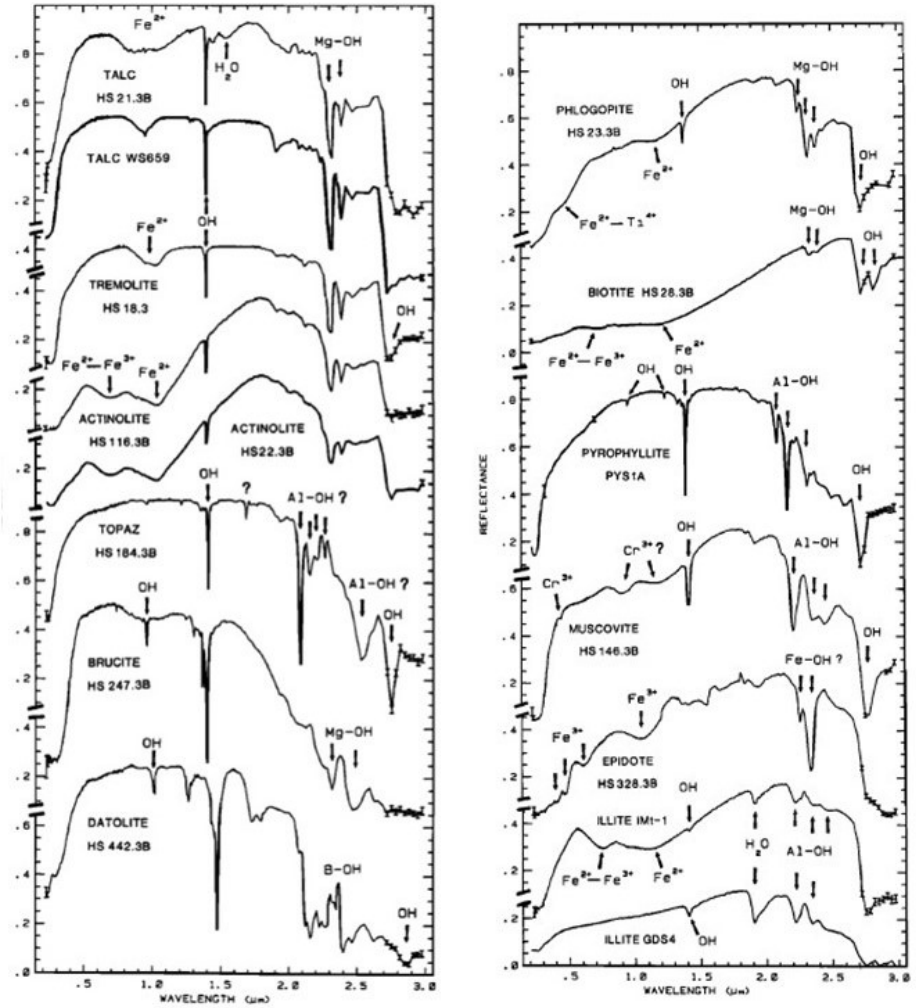

Figure 2.9: *(Left) Reflectance spectra at the standard 1X resolution from 0.2 to 3.0 μm for talc, tremolite, actinolite, topaz, brucite, and datolite. (Right) Reflectance spectra at the standard 1X resolution from 0.2 to 3.0 μm for phlogopite, biotite, pyrophyllite, muscovite, epidote, and illite. Image taken from [31].*

2.6 Sulfates

The main diagnostic absorption feature of sulfates that does not overlap with SWIR functional groups of other major rock-forming minerals is located in the 5748 cm^{-1} (1740 nm) region in the case of gypsum and alunites, and in the 5405 cm^{-1} (1850 nm) region in the case of jarosite. Absorption features overlapping with SWIR functional groups of other minerals are the S-O related ones located at around 2170, 2220, and 2280 nm [37], and overtones and combinations related to Fe-O-H at 1480 nm and 2250 nm. Similar to other mineral groups, the wavelengths of these features can shift considerably across the SWIR, depending on their composition.

An example of sulfates is Alunite. Alunite (Figure 2.6 right) has two widely separated OH stretching frequencies, 3486 cm^{-1} (2.87 μm) and 3513 cm^{-1} (2.85 μm). Although the fundamentals are not fully resolved in Figure 2.6 right, a characteristic doublet is shown in the 1.4 μm overtone (7100 cm^{-1}) region. Absorptions in the spectrum of alunite from 1.7 to 2.6 μm (5900-3800 cm^{-1}) are combinations with bending (librational) and translational modes with the OH stretches. These bands do not show the fine structure of the 1.4 μm complex because the libration and translation

bands have a greater width than the OH stretches. [16] assigned the 1.77 μm absorption (5650 cm^{-1}) to a combination comprised of the second overtone of the Al-OH bend, ν_{AlOH}, whose fundamental vibrations occurs near 1050 cm^{-1} (9.5 μm), plus the OH stretch (ν_{OH}). While the computation gives reasonable agreement with the observed 1.77 μm position, the assignment is not consistent with all Al-OH-bearing minerals; only sulfates show a band in this region. [16] also assigned the 2.17 μm (4610 cm^{-1}) absorption to the OH stretch plus the Al-OH bend and the 1.0 μm (10000 cm^{-1}) band to the third overtone of the OH stretch. However, the 1.0 μm band is too wide for a stretch overtone. It has the shape and width appropriate to be a combination of $2\nu_{OH} + 2\nu_{AlOH}$.

Jarosite and alunite have an overtone OH stretch near 1.475 μm. In jarosite, the OH stretch fundamentals occur at 3430, 3355, and 3260 cm^{-1} (2.915, 2.981, 3.067 μm). The 3355 cm^{-1} band appears the strongest, and O-H librations occur at 790 and 512 cm^{-1} (12.6 and 19.5 μm). The 2.27 μm (4400 cm^{-1}) band in jarosite (Figure 2.10 right) is due to a combination of OH stretch and Fe-OH bend. In jarosite (Figure 2.10 right) and alunite (Figure 2.11 right), the bands do not show as much fine structure as does scapolite.

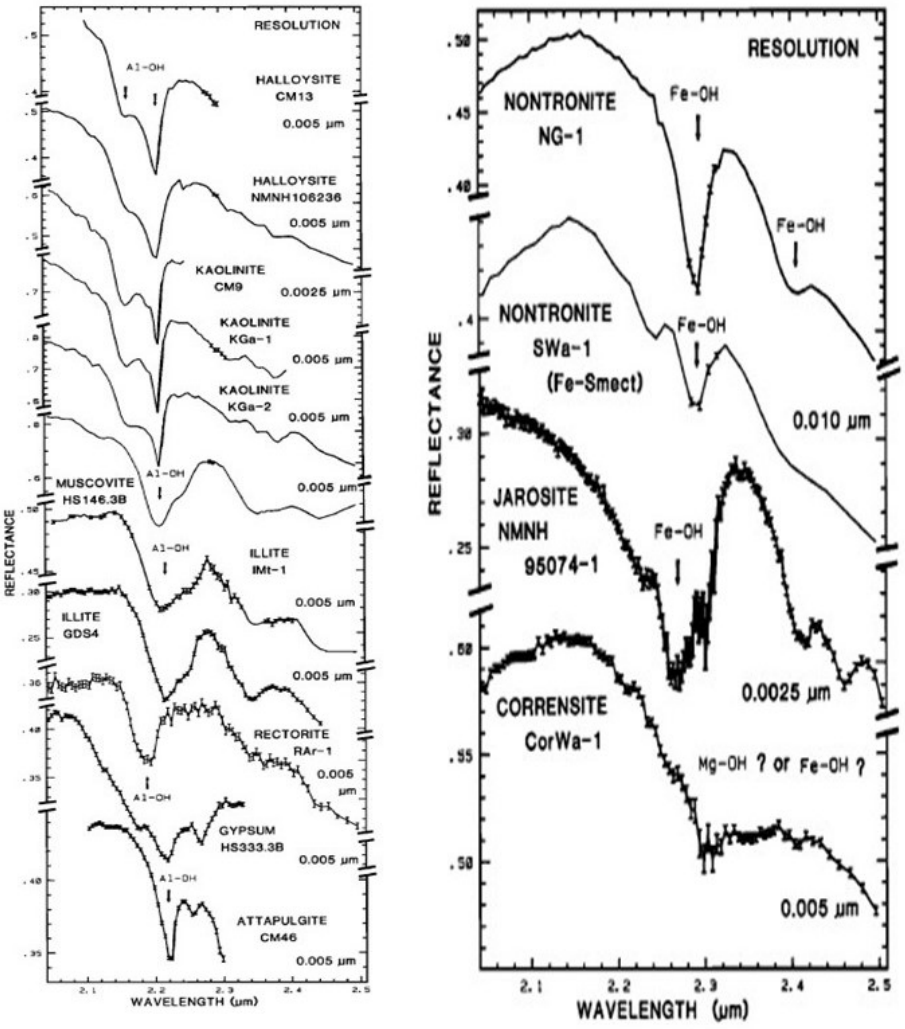

Figure 2.10: *(Right) Absorption features that are relatively sharp and near 2.2 μm. (Left) Absorption features just short of 2.3 μm. Image taken from [31].*

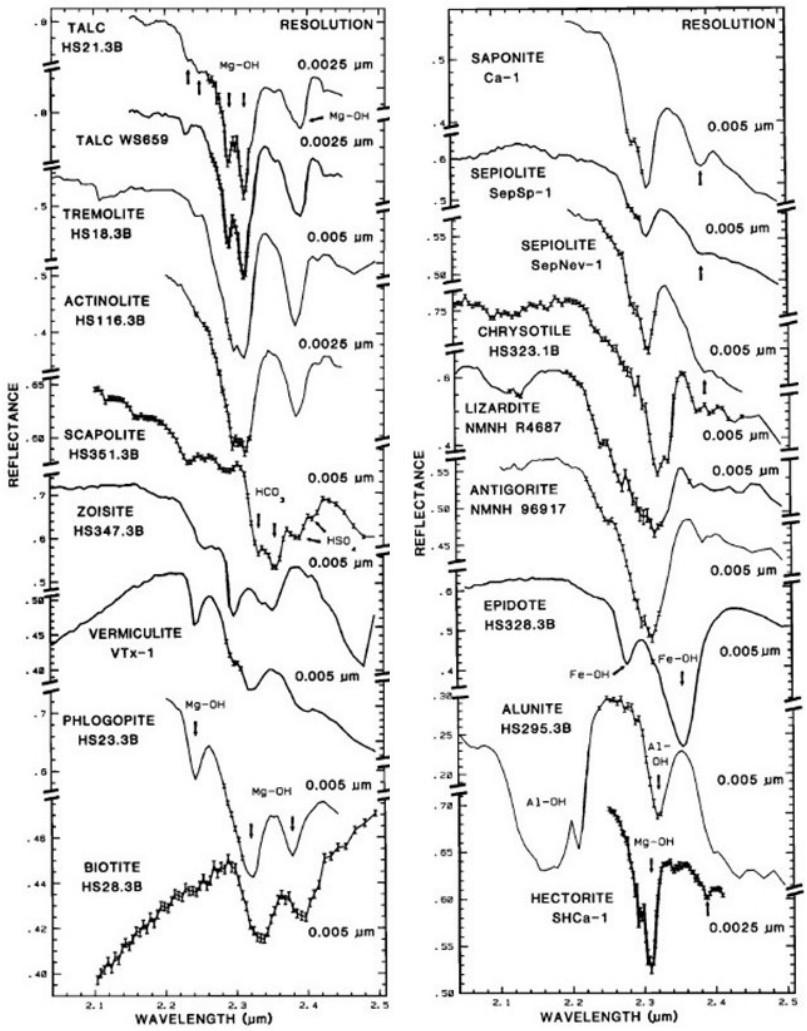

Figure 2.11: *Absorption features showing complex structures just about 2.3 μm. Image taken from [31].*

Chapter 3

Experimental Equipment and Software Tools

3.1 PRISMA

The PRecursore IperSpettrale della Missione Applicativa (PRISMA) mission consists in a Hyperspectral satellite that has the goal to perform Earth Observations (EO) in 239 different bands from 400 nm to 2500 nm.
Until now remote sensing from satellite has been performed in this spectral range with high geometrical resolution satellites (working in the visible range to maintain high the signal to noise ratio) and multispectral satellite (working with fewer bands from visible to short wavelength infrared like Sentinel 2, 13 bands, and Landsat 8, 11 bands with 2 that are in Thermal Infrared).
Hyperspectral imaging is a technology which has recently been developing from satellite for EO. This is due to multiple reasons that make the acquisition of hyperspectral data from satellite problematic for this application, as we are going to explain.
The main geology objective of EO is monitoring hazards and changes of the climate, water, soil and geology in the world. To reach this goal, a certain resolution of the pixel of the detector projected to the source is required. This resolution changes based on the source that the satellite has to analyze, for example it is a severe constraint to analyze severity map of hazards (flooded areas or fire events), or areas that are subjected to important changes (weed invasion, urban development, volcanic eruption). Instead, for what concerns air quality, the geometrical resolution is not so important because gas tend to spread quickly in the medium, differently from the other source discussed above.
Besides the geometrical resolution, it is also important to consider the operative spectral range of the instrument and the spectral resolution. For some analysis the visible spectrum is not enough to establish an effective monitoring on EO, for example to evaluate moisture and hotspots of a source a true-color image could not be the best imaging to conduct the analysis, as these regions of interest (ROI) are not affected by a change of color. To perform this kind of analysis, it is better to move the operative window of the detector to lower energies, like infrared, in order to distinguish the ROI from the background.
The shift to lower energies consequently involves a loss of signal to noise ratio (SNR) which must therefore be compensated by increasing the projection of the pixel on the ground (satellite image downgrade).

Some sources also need a high spectral resolution to perform analysis. In the case of Air Quality, gas may have no color or particular temperature in respect to the background, so to identify a gas in the atmosphere from another, it is necessary to resolve the rotovibrational spectral lines of a particular gas in respect to its background. To accomplish this, a downgrade of the image occurs as fewer photons are available for each channel, so again to maintain a high SNR it is necessary to enlarge the pixel projection on the ground. The finer is the sampling, the more it will be necessary to increase the size of the pixels that will build the satellite image.
In image 3.1 is reported an overview of band distribution and bandwidth of satellites that are representative of their class (very high geometrical resolution with broad bands in the visible, or satellites with very high spectral resolution with spectrometers mounted onboard).

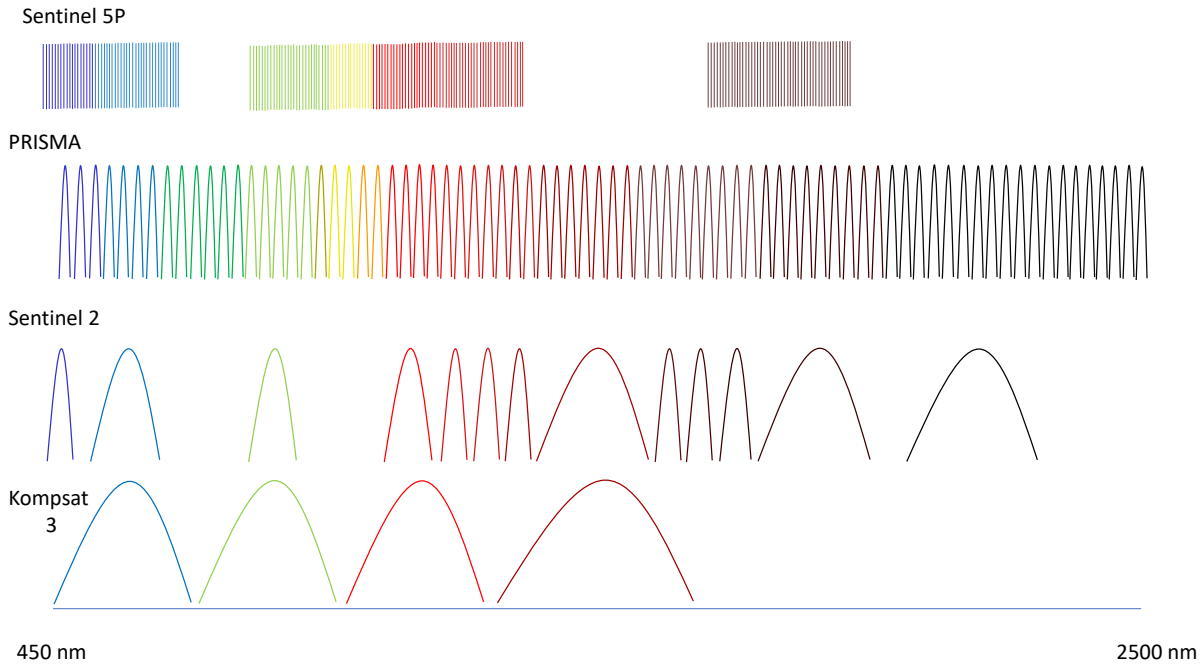

Figure 3.1: In this figure it is possible to see an overview of band distribution and bandwidth of a very high geometrical resolution satellite (KOMPSAT 3), a typical multispectral satellite (Sentinel 2), a hyperspectral satellite (PRISMA) and a satellite with very high spectral resolution (Sentinel 5P).

With these concepts in mind, it is possible to understand vantages and disvantages between multispectral and hyperspectral imaging and what kinds of requirements are needed to analyze a certain source.
In case the boundary of an area is to be drawn (e.g. due to fires or invasive vegetation) and colors in visible range are sufficient to distinguish ROI from the background, the optimal detector for this source is a camera with only three broad channels centered on the red, green and blue bands (this is an RGB image).
For example the satellite Korean Multi-Purpose Satellite 3 (KOMPSAT 3) [38] has a geometrical resolution of 0.55 m for a panchromatic image (an image produced with only one band from 450-900 nm) and 2.8 m for the following bands: blue (450 nm - 520 nm), green (520 nm - 600 nm), red(630 nm - 690 nm) and near-infrared (NIR) (760 nm - 900 nm). KOMPSAT 3 is a perfect example of a multispectral satellite, it has an optimal spatial resolution but to accomplish this result it has radiometrically broad bands so with a low spectral resolution.

Sentinel 5P is instead a classic example of a satellite with a relatively very high spectral resolution. It has a spectrometer mounted onboard that works with a spectral resolution of 0.25 nm in ultraviolet-visible range from 270 to 495 nm, near-infrared range from 675 to 775 nm and short wavelength infrared range from 2305 to 2385 nm but, to reach this fine sampling of the bands, the geometrical resolution is very low, the satellite image is composed of pixels that are larger than 3000 m.
A satellite like KOMPSAT 3 could be perfect to define boundaries of a vegetation cover in a very different colored background (like bushes in a desert), while Sentinel 5P is optimal to perform air quality (like the identification of methane emissions in the air).
PRISMA satellite is located in the middle of these two extremes : it has a geometrical resolution of 30 m and a spectral resolution of 9 nm but acquires without any gap (except the windows given by the atmospheric presence between the source and the detector) the electromagnetic spectrum from visible to short wavelength infrared, so it is perfect to extract spectral signatures of sources that do not require a spectral resolution inferior to the 9 nm of sampling.
Rocks are the optimal target because differently from gas there are no rotational line (a resolution of 9 nm is enough), they do not spread quickly in their background (a resolution of 30 m is good while 3000 m could be insufficient for the localization of the target) and have overtones and combination bands that, as described in section 2, promote to higher energy their characteristics signal in spectral signatures given by the interactions of photons with phonons (analyzing the SWIR range is enough).

To discuss in quantitative terms the compromise between spatial and spectral resolution of the satellite, which represents a key aspect of the spectroscopic apparatus, we decided to show part of the results of another contribution, present in the bibliography as [39]. The part of the article that interests us estimates the information content of a hyperspectral image of the AVIRIS mission (explained in the 1.10 section) in terms of Shannon entropy [40].
Given a particular configuration of spatial and spectral resolution, the entropy of an image provides the average amount of information this apparatus has for that scene. However, since the underlying probability distribution of hyperspectral images is unknown, we cannot calculate the entropy using a closed-form expression and are faced with a multidimensional estimation problem.
One of the possible entropy estimation methods is based on the assumption that the data is distributed as a multidimensional Gaussian.
Assuming a functional model of the data distribution always implies an error in the results. We are mainly only taking second-order relations into account, and thus discarding any higher-order terms. Since multidimensional probability estimation is a difficult problem, assuming this model, we greatly simplify the calculation. Furthermore, although the images are not distributed as multidimensional Gaussians, the assumption is not entirely unrealistic [41]. In reality, the error caused by ignoring higher-order relations in natural images is usually not very large [42].
Given a hyperspectral image in matrix form $\mathbf{X}$, the expression of the entropy of a multidimensional Gaussian distribution ($h(\mathbf{X})$) is the following:

$$h(\mathbf{X}) = \frac{d}{2}(1 + \ln(2\pi)) + \frac{1}{2}\ln|\mathbf{\Sigma}| \tag{3.1}$$

where d is the number of dimensions and $|\mathbf{\Sigma}|$ is the determinant of the covariance matrix.

Figure 3.2 shows a matrix where each element represents the estimated Gaussian entropy of the AVIRIS configuration (224 bands of 10 nm width with central wavelengths from 400 to 2500 nm) for a specific spatial resolution and spectral resolution.

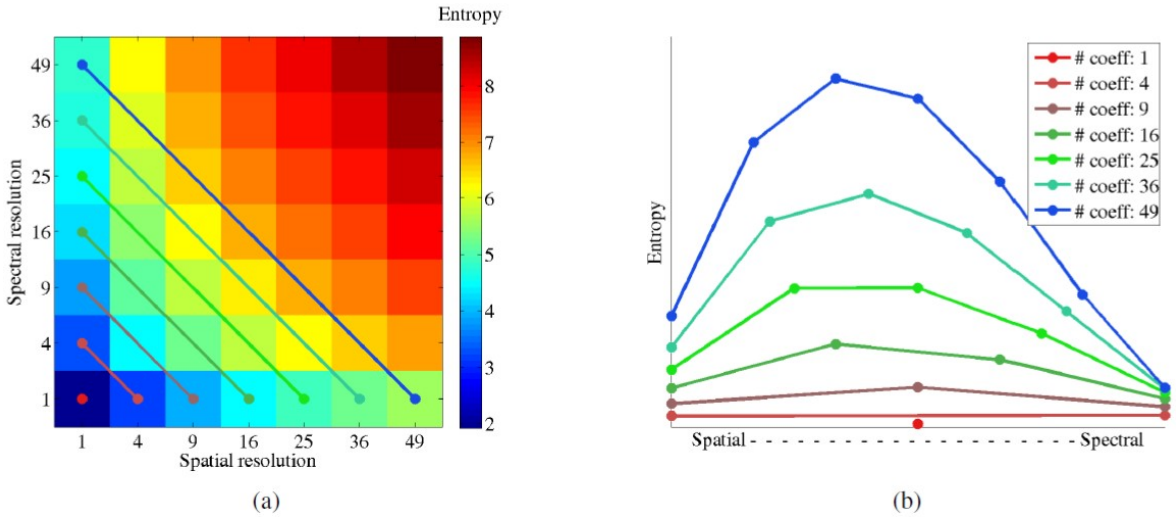

Figure 3.2: Estimation of entropy in AVIRIS using the Gaussian model: (a) Entropy for different spatial and spectral resolution configurations. Entropy values are logarithmic scaled for display purposes. (b) Entropy for a fixed number of coefficients (selected diagonals of the entropy matrix). Image taken from [39].

Note that the error in this measure is determined by the error in the estimation of the covariance matrix, which is not critical when a large number of samples are available.

The Satellite

In this section is described the technical sheet of the PRISMA mission.
PRISMA is a hyperspectral satellite (launched on 22^{nd} March 2019 and should last five years) that analyze planet Earth in a spectral range from visible (406 nm) to short wavelength infrared (2497 nm) with a spectral resolution of 9 nm, resulting in 239 different channels of acquisition (as we can see in the next subsection, the name of the satellite is based from the fact that the incoming reflected sunlight is diffracted by a prism that subdivide the beam in 239 different signals).
From the fact that is not a constellation, that means a group of satellites built in the same way and with the same mission, (this will change in near future with the next mission PRISMA2G as described in subsection 1.10 that will work together with PRISMA) its revisit time (that means the time that elapses from an acquisition on a certain area of the globe before the satellite is ready to reacquire the same area along its orbit) is relatively low (less than 7 days, depending on the zone that is covered during the orbit of the satellite).
The satellite travels around earth in a Low Earth Orbit (LEO) at a distance of 615 km from the planet. Its repeat cycle, which is the time it takes for the satellite to restart its cycle of observations of the earth by finding itself in its initial position, is 29 days after traveling 430 orbits.The time of acquisition of a single satellite image is about 4.31 s and its processing time is about 39 minutes

(this time can vary deeply based on the level of data processing described in subsection 3.1). The dimension of the projection on the ground of a single acquisition of the satellite (that is called footprint) is about 30 × 30 km (this is the size of all PRISMA images analyzed in this work and the size of a single pixel that compose these images is 30 × 30 m).

Payload

In this subsection it is described the payload of PRISMA satellite, its sketches and modules.
In figure 3.3 we can see the sketch of the payload of the satellite that consists in: telescope (with the three mirror anastigmatat configuration of figure 3.4 to avoid any optical aberration), a beam splitter (that makes an in-field separation of the light of the source to separate the signal detected from the panchromatic camera from the signal intended for the VNIR and SWIR detector), a panchromatic camera (used for alignment and georeferencing of the PRISMA acquisition, this single channel that cover the visible spectral range from 400 to 700 nm has a geometrical resolution of 5 m), a dichroic beam splitter (that separates the visible-near infrared component from the short wavelength infrared component), the detector in the VNIR spectral range (60 bands in the spectral range from 400 to 936 nm) and the detector of the SWIR spectral range (172 bands in the spectral range from 936 to 2498 nm).

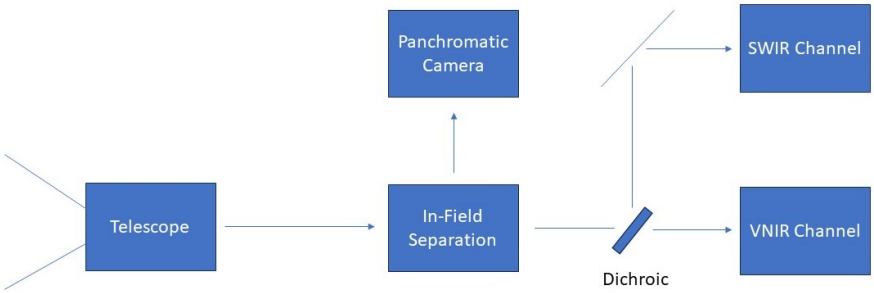

Figure 3.3: *PRISMA sketch: sunlight reflected from earth goes in the telescope, suffers an in-field separation making one part of the beam to be analyzed from the panchromatic camera, the other part experiment another separation but this time in the spectral component due to a dichroic beam splitter, the visible near infrared component pass through the dichroic beam splitter and is directed to the VNIR detector (VNIR hypercube), the short wavelength part of radiation is separated from the VNIR component and is analyzed by the SWIR detector (SWIR hypercube).*

.

In figure 3.4 it is shown in the three mirror anastigmatat configuration.
This configuration allow minimizing all three main optical aberrations (spherical aberration, coma, and astigmatism) in the satellite image (in this way there is no need to consider these aberrations during the data processing corrections).

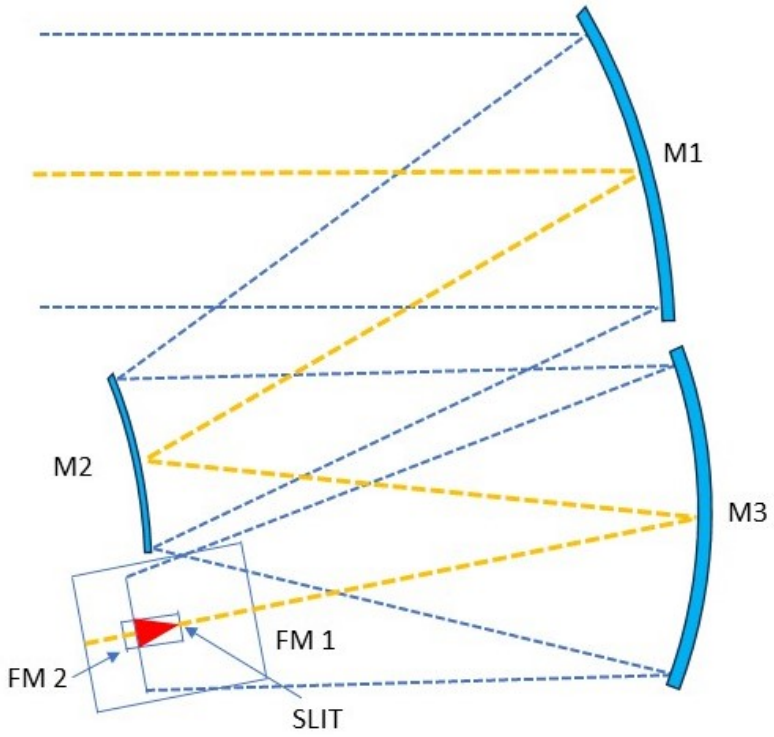

Figure 3.4: *The three mirror anastigmatat configuration mounted onboard on the PRISMA mission. The Dark Yellow solid line simulates a ray of the source that is guided to the slit of the system by using three aspherical mirrors indicated as M1, M2 and M3 in the figure. In this figure are also present the two folding mirrors FM1 and FM2 that guide the ray to the detectors, as showed in the next figure. (Inspired from image: Selex ES).*

.

In figure 3.5 it is possible to observe in detail the structure of rays, from the slit of entrance to the detectors.
As said before, the spectrometer of PRISMA is separated in two different detectors, one is for the visible-near infrared spectral range and the other is in short wavelength infrared spectral range.

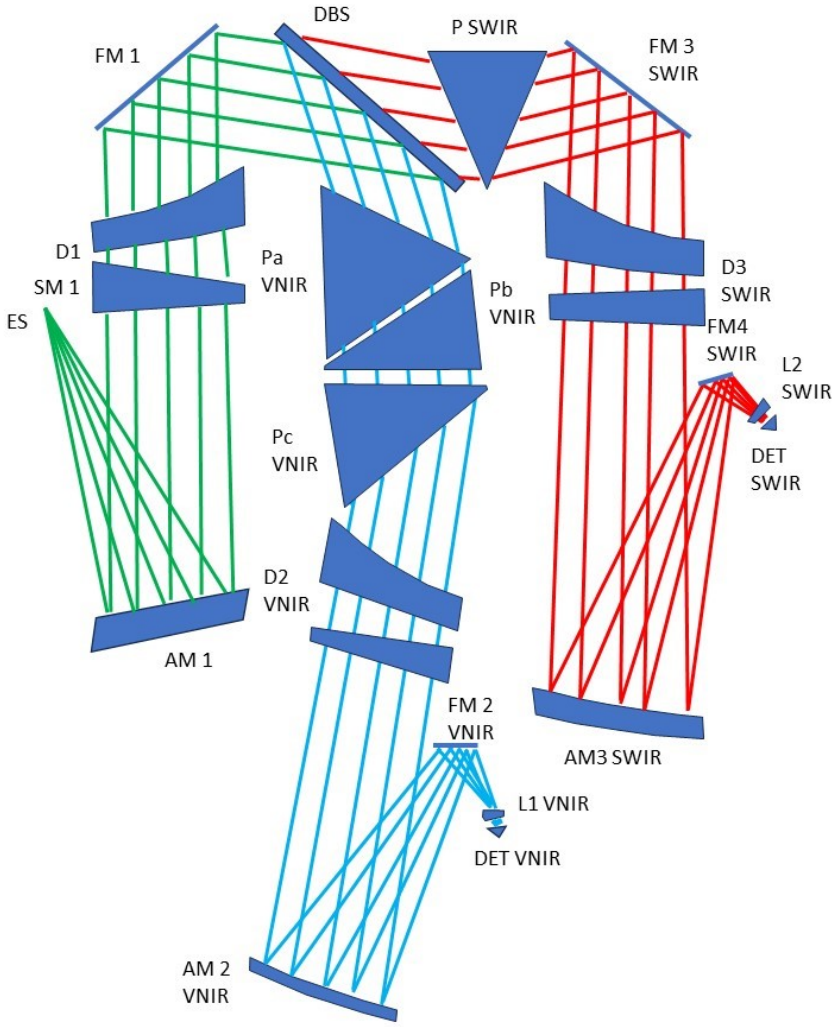

Figure 3.5: *Sketch of the structure of rays from the slit of entrance of the telescope to the VNIR and SWIR hypercubes.(Inspired from image: Selex ES)*

The SWIR detector mounted onboard on the PRISMA satellite is a HgCdTe called Saturn and provided by Sofradir technologies (France). Saturn has a length of 30 mm, and includes 256 lines of 1000 pixels at 30 µm pitch. A different gain is applied to each line, making this detector especially adapted to spectroscopy and hyperspectral imaging, in addition, a complementary technological process allows it to extend the responsivity down to the visible spectrum.

The VNIR detector is constituted by a Saturn VNIR detector with 256 lines of 1000 pixels at 30 µm pitch and a usable spectral band of 0.4 to 1.1 μm. This detector was realized by Sofradir by using the Cadmium Zinc Telluride (CZT) to obtain the sensitivity in the visible spectral range.

The last module that is treated in this subsection is the Internal Calibration Unit (ICU).
The in-flight ICU (Internal Calibration Unit) is designed to allow the support of absolute and relative radiometric calibrations and spectral calibrations. The ICU utilizes an optical path to image the sunlight through a dedicated solar entrance port, seen during the calibration activity by the

primary mirror of the telescope. The calibration unit consists of a solar port cover mechanism, filters and spectral lamps. Dark calibration is implemented by a lightweight shutter placed in front of the optical slit.
The ICU input spectral radiance for calibration is generated by the Sun (ICU_S mode) or by Internal Sources (ICU_{Is} mode), through a dedicated optical path. The objective of the ICU is the illumination of the whole instrument pupil and field of view by the reference radiation passing through the same optical path of the Earth-observed signal: in fact a calibration dedicated optical path (both for the sun and for the internal sources) is realized to impinge the back surface of the main port cover. This is provided with a metallic diffuser, that allows a stationary illumination directly on the telescope primary mirror, filling the whole entrance pupil of the telescope.
Dark frames are periodically acquired by closing the shutter located at the spectrometer entrance slit, allowing the offset background subtraction from the ICU internal sources.

- ICU_S mode: During sun calibration, the sun port cover shall be opened for the time strictly needed to perform the acquisition. The solar radiation enters into the instrument through the sun port, passes a transmission diffuser and then, by means of a flat folding mirror, a dedicated relay optics and the Sun Beam Splitter (optimized to maximize the radiance from the lamp sources), it is redirected towards the internal (back) surface of the main port cover shown in fig 3.6.

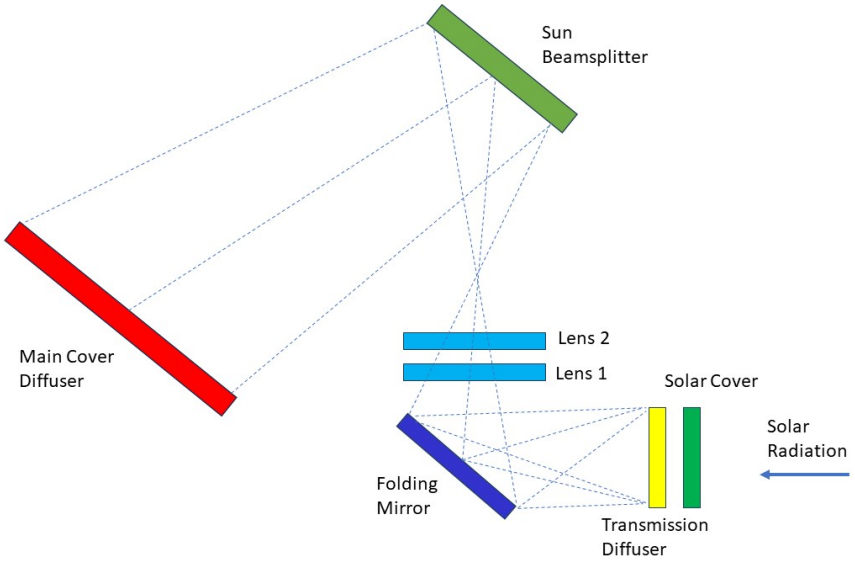

Figure 3.6: *Sketch of the ICU in Sun calibration mode.(Inspired from image: Selex ES)*

- ICU_{Is} mode: ICU unit is provided by radiance calibrated tungsten lamps positioned in dedicated reflecting lamp-housings. The lamp-house aperture supports a transmittance filter having calibrated spectral signatures. The internal calibration sources are composed by two equal groups (main and redundant) of a couple of lamps: one lamp for VNIR and the other for the SWIR channel. The VNIR and SWIR lamps differ on the filter spectral features and on the lamp-housing coating.

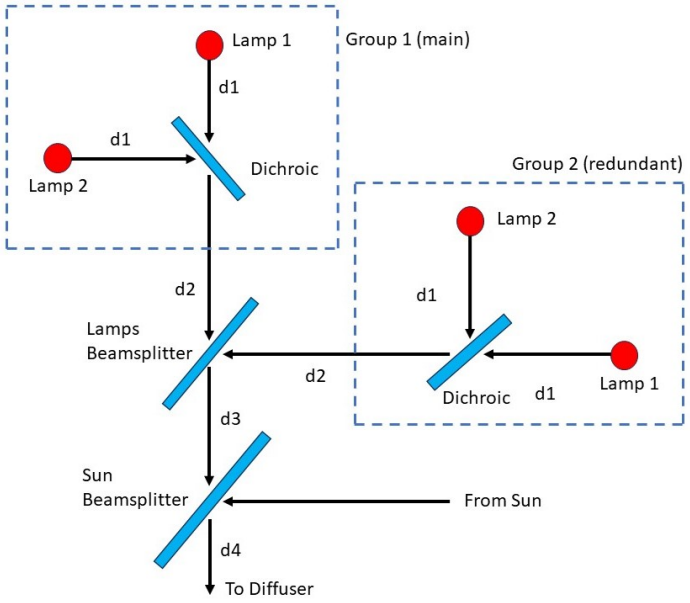

Figure 3.7: *Sketch of the ICU in Internal Source calibration mode.(Inspired from image: Selex ES).*

Data Processing

Now that we have defined modules and functions of the satellite, we have to describe the level data processing of the satellite data that are used in this work.
The level data processing represent the degree of corrections that were performed on the raw data before it was delivered (for example the level L0 is the lowest degree of corrections that represent the raw data while level L2D is the maximum degree of corrections on the raw data with orthorectification, georeferencing etc.).

L0 Level Data Processing

The L0 processor is tasked with generating multiple L0a files based on the contents of the input Decyphered Data File. The Cloud-Coverage percentage is calculated for L0a Earth-Observation files and integrated into the Catalog Metadata of the corresponding L0a file. In addition to the L0a products, the L0 processor is configured to create a LIST file and a Screening Report file. For each file designated for archiving, specific Catalog Metadata is generated. This section offers an overview of the produced items. Figure 33 illustrates a block diagram of the L0 Processing scheme:

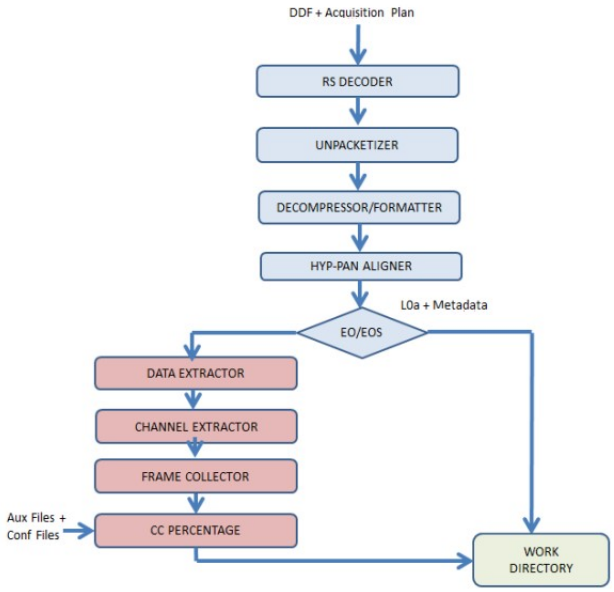

Figure 3.8: *Level L0 data processing workflow. Taken from PRISMA Products Specification Document Issue 2.3 Date 12/03/2020.*

L1 Level Data Processing

The L1 Processor receives, as input, the list of L0a data files for a specific type of Scene Of Interest (SOI), including five files containing the Key Data Parameters (KDP) such as In-Flight Data Parameters (FKDP), Ground Key Data Parameters (GKDP), Characterization Data Parameter (CDP, which are parameters triggerable by an expert user and necessary for processing, such as the number of bands to be used, thresholds for KDP, etc.), and Internal Calibration Unit Key Data Parameters (ICU-KDP) files. Additionally, a set of Auxiliary Data Files is obtained from the Image Data Handling Segment (IDHS) archive.

There are up to 6 different types of SOI, two belonging to the class SOI-A (Earth Observation) and five belonging to the class SOI-B (satellite calibration):
- SOI-A-1: Earth Observation;
- SOI-A-2: Earth Observation Cal-Val;
- SOI-B-1: Internal Calibration Cal-Val;
- SOI-B-2: Sun Calibration;
- SOI-B-3: Moon Calibration;
- SOI-B-4: Flat Field Calibration.

Each type of SOI is always associated with the updating of a sub-set of FKDP parameters typical of the current instance: if the updated FKDP parameters are noticeably different with respect to the input ones, L1 processing can produce a new FKDP updated file, to be sent to the IDHS archive. SOI-A classes are also associated with the generation of the L1 Earth Observation radiance file. The L1 Earth Observation Product contains four layers of data, each referring to a specific type of data, and a fifth layer collecting the information extracted from the Header Packets of the L0a files.

FrameBuilder is the first algorithm of the processor according to which the incoming SOI L0a files are transformed into two lists of Cubes: one for SWIR+VNIR channel, the other one for the PAN channel. Each cube contains a list of frames, ordered according to UTC Time, of the same Sub-Acquisition Type. In the case of HYPER (VNIR+SWIR) channel, the cube has the following axis-meaning: the x axis is aligned with the spectral direction (Band), the y axis is the across track direction (Sample) and the z axis is the along track direction (Line/Frames).
Each (y,z) plane represents a monochromatic image, while each (x,y) plane represents a Frame (which, sliding along the z axis, creates the Raster).
In the case of PAN channel, the image (the spectral direction is absent) has the following axis-meaning: the x axis is the across track direction (Sample), the y axis is aligned with the along track direction (Line).

The KDP Updating basically consists of the following algorithms:
- Dark Updating (performed for each type of SOI);
- Background Updating (performed for each type of SOI);
- Lamp Updating (performed for each type of SOI);
- Lamp Linearity Updating (performed only in case of SOI-B-1);
- Sun Updating (performed only in case of SOI-B-2);
- Moon Updating (performed only in case of SOI-B-3);
- Flat Field Special Updating (performed only in case of SOI-B-4).

In the Earth Observation Processing, that means only for SOI-A, the algorithms are designed to handle the following main steps:
- Radiance Generation: This step involves processing the cubes created by the FrameBuilder of Surface-Obs sub-acquisition type, utilizing the Key Data Parameters to convert the Digital Numbers of L0a Packets into Spectral Radiance.
- Coregistration: The Coregistration algorithm takes the Radiance cubes from both HYPER (VNIR+SWIR) and PAN channels, produced in the previous steps, and generates two new cubes for HYPER and PAN Surface-Obs. These new cubes incorporate spatial coregistration, aligning SWIR and PAN channels with respect to the VNIR channel.
- Mask Generation: This algorithm serves the purpose of generating masks for Cloud Coverage, Sun Glint, and Generic Land Cover. These masks provide valuable information for subsequent analysis.
- End User Binning: This step is executed only in the case of SOI-A-1, where user-defined processing is required. For SOI-A-2, which is an automatic processing scenario, this step is skipped. The End User Binning process involves binning data in spatial and/or spectral dimensions based on input parameters set by the user.

The L1 Earth Observation Product comprises four types of data organized into four layers:
- Radiometrically Calibrated HYPER and PAN Surface-Obs cubes: These are produced by the

Radiance Generation step, providing calibrated spectral radiance information.
- Coregistered HYPER and PAN Surface-Obs cubes: Generated by the Coregistration algorithm, these cubes incorporate spatial coregistration, aligning SWIR and VNIR channels with respect to the PAN channel.
- Cloud Coverage, Sun Glint, and Generic Land Cover masks: These masks are generated in the Mask Generation step, providing valuable information about cloud coverage, sun glint, and land cover.

The architecture diagram of the L1 Processing is depicted below:

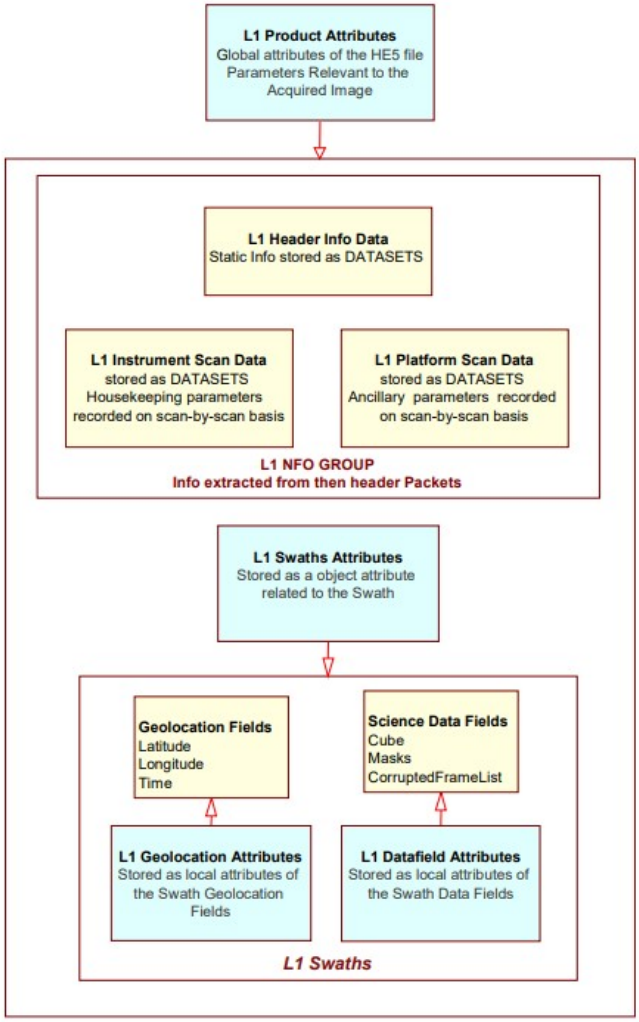

Figure 3.9: *Architecture of the PRISMA Level 1 Earth Observation Products. Taken from PRISMA Products Specification Document Issue 2.3 Date 12/03/2020*

L2 Level Data Processing

The Level 2 processing is responsible for converting measurements of Top-of-Atmosphere spectral radiance into geophysical parameters. These parameters are dependent on the observed pixels and offer insights into:
- The atmosphere-surface radiance/reflectance;

- The properties of the atmosphere above the surface (Aerosol Optical Thickness, Water Vapor and Cloud Optical Thickness).

The steps involved in converting Top-of-Atmosphere spectral radiance (Level 1) to Bottom-of-Atmosphere (Level 2c) are commonly referred to as atmospheric correction.
The transition to Level 2d, a stage involving the assignment of geographical coordinates, is known as geocoding.
The block diagram detailing the processes of Level 2 is provided below:

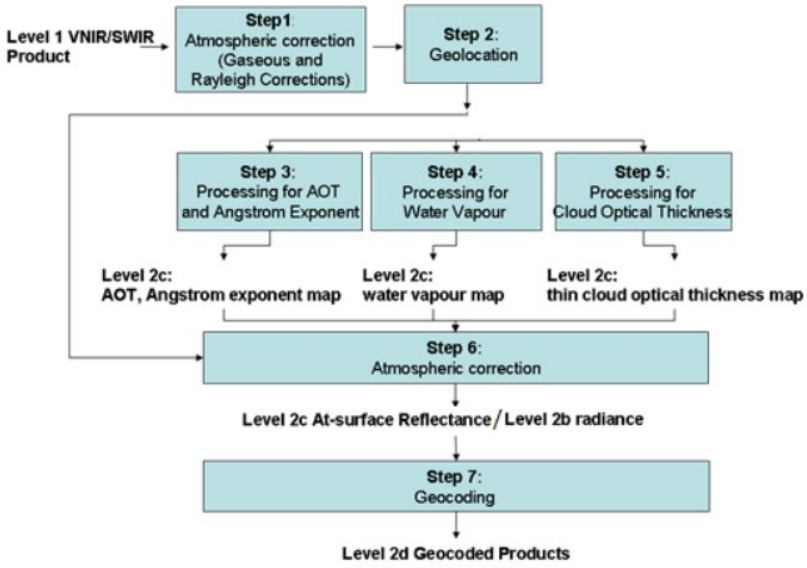

Figure 3.10: *Level L2 data processing workflow.Taken from PRISMA Products Specification Document Issue 2.3 Date 12/03/2020*

As we will describe in subsection 3.3, I used the EnMAP Toolbox software to transform the PRISMA hierarchical file in a raster within the Geographical Informatic System (GIS), this software requires only PRISMA L2D file in input so all PRISMA images that are present in this work are level 2D.

3.2 Laboratory Spectometer

Fourier Transform Infrared (FTIR) spectroscopy relies on the concept of interference between two optical beams that travel along paths of different lengths. Such interference is then measured as a function of the beams path difference (the interferogram) and via Fourier Transform the spectrum (i.e., the intensity as a function of frequency) is retrieved.
The Michelson interferometer can be thought as the prototypical setup for FTIR: it comprises a beam splitter and two mirrors, one fixed and another capable of moving back and forth, as shown in figure 3.11. The light from an IR source is split into two orthogonal beams by the beam splitter. The beam splitter, indeed, partially transmits the light toward the fixed mirror and partially reflects it toward the moving mirror. The two beams are then reflected by the two mirrors and are superimposed at the beam splitter position, generating an interference pattern. The intensity I ($\boldsymbol{\delta}$), collected by the

detector, is a function of the path length difference ($\boldsymbol{\delta}$) that is determined by the different distances at which the two reflecting mirrors are positioned with respect to the beam splitter.
To better explain the working principle of a Michelson interferometer, one can start by considering the case of a monochromatic source and evaluate the interference patterns as a function of the beams path difference $\boldsymbol{\delta}$.
If the distance traveled by the two beams is identical, then $\boldsymbol{\delta} = 0$ (zero path difference). In this configuration, the two beams are in phase when they recombine: they constructively interfere, and the amplitude of the final beam is the sum of the individual amplitudes. These two beams will be in phase with each other whenever their optical path difference is a multiple of the wavelength $\boldsymbol{\delta}$=n$\boldsymbol{\lambda}$, with any integer value n.
Contrarily, if $\boldsymbol{\delta} = (n + \frac{1}{2}\boldsymbol{\lambda})$, the two beams are out of phase and undergo a destructive interference, i.e., the amplitude of the resulting beam is zero. By moving the mirror, there is thus a large change in the intensity of the beam leaving the interferometer, and the intensity passes through maxima and minima (as depicted in figure 3.12). The interferogram is the plot of light intensity versus optical path difference (an example is shown in figure 3.13 left panel).
To get the relation between the interferogram and the spectrum, we can start writing the Fourier Transform of the electric field incident on the beam splitter

$$\boldsymbol{E}(\boldsymbol{r}, t) = \frac{1}{2\pi} \int_{-\infty}^{+\infty} B(\omega)^{\frac{1}{2}} e^{i(\omega t - \boldsymbol{q}\cdot\boldsymbol{r})} d\omega \tag{3.2}$$

We have assumed that $\boldsymbol{E}(\boldsymbol{r}, t)$ has a periodic time dependence. The average intensity at the beam splitter after the two beams are reflected from the mirrors is

$$I(\boldsymbol{r}, t) = \frac{c}{8\pi t} \int_{-T/2}^{+T/2} \left| \frac{\boldsymbol{E}(\boldsymbol{r}, t+\tau)}{2} + \frac{\boldsymbol{E}(\boldsymbol{r}, t)}{2} \right|^2 dt \tag{3.3}$$

where τ is the time difference accumulated due to the beams path difference, and T is the period of time varying electric fields. Employing the expression of $\boldsymbol{E}(\boldsymbol{r}, t)$ (eq. 3.2) into the eq. (3.3), we get:

$$I(\tau) = \frac{I_0}{2} + \frac{c}{16\pi^2 T} \int_{-\infty}^{+\infty} B(\omega) cos(\omega\tau) dt \tag{3.4}$$

where

$$I_0 = \frac{c}{8\pi T} \int_{-T/2}^{+T/2} \boldsymbol{E}(\boldsymbol{r}, t) \cdot \boldsymbol{E}^*(\boldsymbol{r}, t) dt \tag{3.5}$$

The spectrum can be now obtained by computing the Fourier transform of the interferogram $I(\tau)(eq.(3.4))$ as following

$$B(\omega) = \frac{32\pi T}{c} \int_{-\infty}^{+\infty} \left(I(\tau) - \frac{I_0}{2} \right) e^{-i\omega\tau} d\tau \tag{3.6}$$

In the real case, it is not possible to integrate over the whole range $(-\infty, \infty)$ as the maximum time delay between the two beams depends on the maximum displacement of the mirror (L). By using $\tau_0 = 2L/c$ as the maximum time delay, we can rewrite eq.(3.6) as the following:

$$B_r(\omega) = \frac{32\pi T}{c} \int_{-\tau_0}^{+\tau_0} \left(I(\tau) - \frac{I_0}{2} \right) e^{-i\omega\tau} d\tau \tag{3.7}$$

$B_r(\omega)$ is thus the expression of the real spectrum. If we define:

$$C(\tau) = \frac{32\pi T}{c} \left(I(\tau) - \frac{I_0}{2} \right) \tag{3.8}$$

the eq. (3.7) can be rewritten simply as:

$$B_r(\omega) = \frac{32\pi T}{c} \int_{-\infty}^{+\infty} C(\tau) e^{-i\omega\tau} d\tau \tag{3.9}$$

In the case of a delta like spectrum $B(\omega) = B_0\delta(\omega - \omega_0)$, we obtain from eq. (3.9) that $C(\tau) = C_0 e^{i\omega_0\tau}$, with $C_0 = B_0/2\pi$. The real spectrum becomes:

$$B_r(\omega) = C_0 \int_{-\tau_0}^{+\tau_0} e^{-i(\omega-\omega_0)\tau} d\tau = 2C_0 \frac{sin[(\omega - \omega_0)\tau_0]}{(\omega - \omega_0)\tau_0} \tag{3.10}$$

The finite displacement of the mirror broadens, thus, the line shape of an infinitely narrow peak. The width ($\Delta\omega$) of the peak will be approximately $\approx 1/2L$. The theoretical resolution power of the interferometer can be thus defined as:

$$\frac{\omega}{\Delta\omega} \approx 2L\omega \tag{3.11}$$

Hence, the resolution power is directly proportional to the maximum displacement of the mirror (L) and the frequency (ω).
Fig. 3.14 depicts the commercial IR spectrometer employed in the experiments, the Bruker Vertex 70v. The spectrometer was equipped with a blackbody source, with the maximum intensity peak in the mid-IR spectral region (2-20 μm). The detector employed is a Mercury Cadmium Telluride (HgCdTe) which is a photovoltaic detector. The working principle is that when an IR photon is absorbed, an electron moves from the valence band to the conduction band. The electrons in the conduction band generate an electrical current proportional to the IR light intensity. HgCdTe detector is cooled down to $\approx$ 77 K to avoid excitation of electrons by thermal motion, which results in a noisy signal.

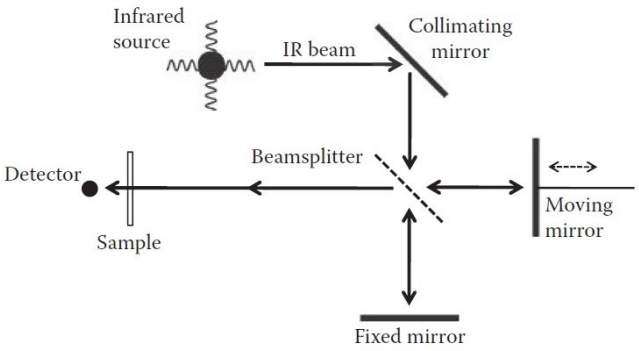

Figure 3.11: *Sketch of the Michelson interferometer [43].*

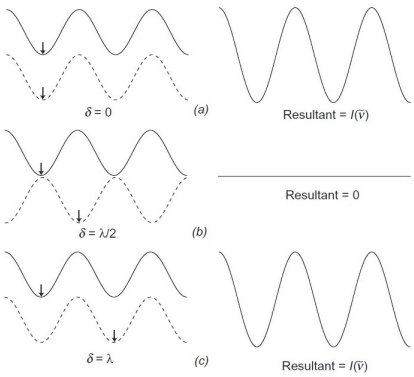

Figure 3.12: *The beam reflected by the fixed mirror (solid line) and the one reflected by the moving mirror (dotted line) at the beam splitter position with optical path difference (a) $\delta = 0$ Zero Path Difference, (b) $\delta = 1/2\lambda$, and (c) $\delta = n\lambda$. (right) The corresponding constructive (top and bottom) and destructive (middle) interference patterns [44].*

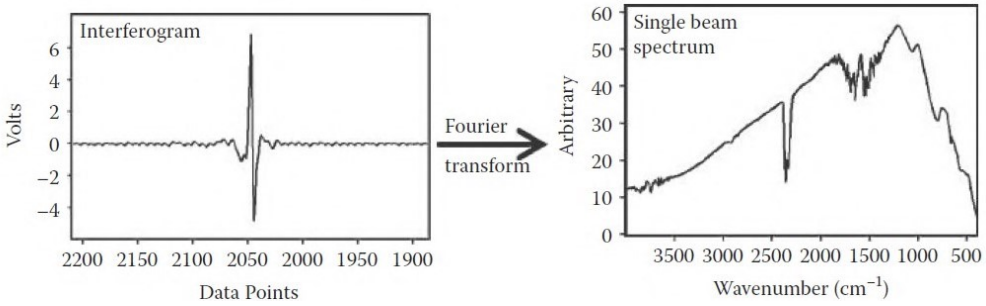

Figure 3.13: *(left) Typical interferogram of a blackbody-type source. (right) The spectrum obtained via Fourier Transform of the interferogram [43].*

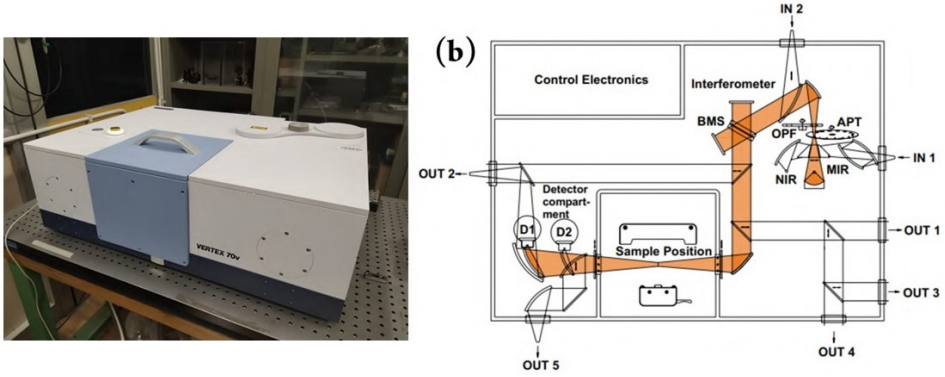

Figure 3.14: *a) Picture of the interferometer Bruker 70v employed in the experiments. b) The corresponding optical scheme.*

.

From the fact that all spectral signatures of this work extracted in laboratory come from solid rocky samples, the mode used in this thesis is always the Reflection mode and not the transmission mode (see figure 3.15).

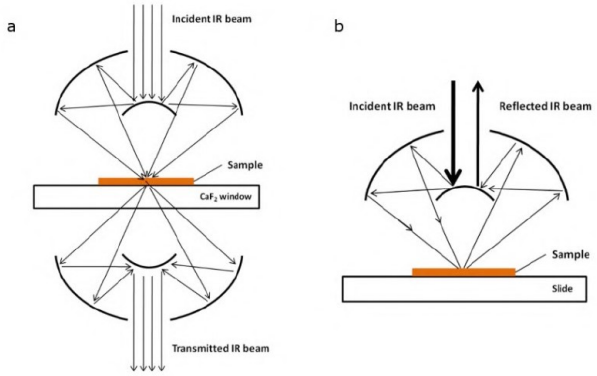

Figure 3.15: *Cassegrain objectives for FTIR microscopy. a) Transmission mode: two faced Cassegrain optics are used as focusing condenser and collecting objective. b) Reflection mode: only one objective is used for both sample illumination and reflected light collection.*

In fig 3.16 we can see a collection of spectra extracted from samples inserted in the FTIR during the doctoral activity.

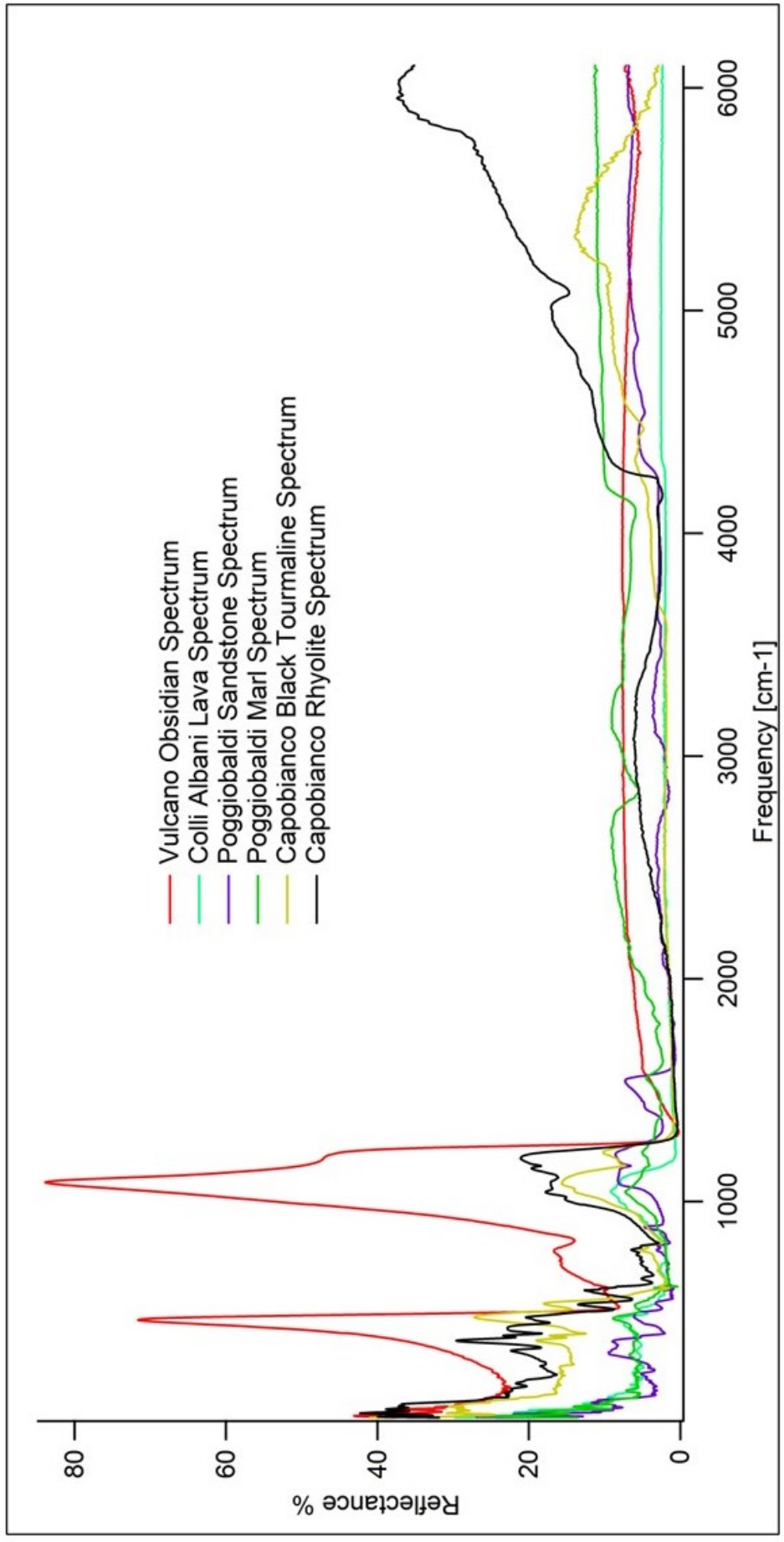

Figure 3.16: *A collection of spectra extracted from samples inserted in the FTIR. (Red solid curve) The spectrum of a fragment of Obsidian from the slopes of Vulcano, it is possible to notice its glassy nature from the high reflectivity signal in the LWIR (more than 85%) and the near absence of features in the VIS-NIR and SWIR, which does not belong to the other samples. (Light cyan solid curve) Spectrum of a fragment of lava from Colli Albani (countryside southeast of Rome). (Violet solid curve) Spectrum of a fragment of sandstone and (Dark green solid curve) spectrum of a fragment of marl both from Poggio Baldi and constitute the main component of the rock escarpment found in the article given in Appendix A. (Dark yellow solid curve) spectrum of a fragment of black tourmaline and (black solid curve) spectrum of a fragment of rhyolite both from the same sample collected from the shores of Capobianco (see section 4.6), the sample in fact presents as a white matrix (rhyolite) within which there are black inclusions (black tourmaline), and laboratory analysis was performed on both components.*

3.3 Softwares

This section describes the software used to manage satellite, terrestrial and laboratory data of the work.

QGIS

The software used to analyze satellite images in the GIS environment is QGIS. This software is also used to perform mathematical operations in all pixels of the raster (like the application of the discrete derivative algorithm in subsection 4.2).
In Figure 3.17 is shown the graphical user interface of a project opened in the QGIS environment.

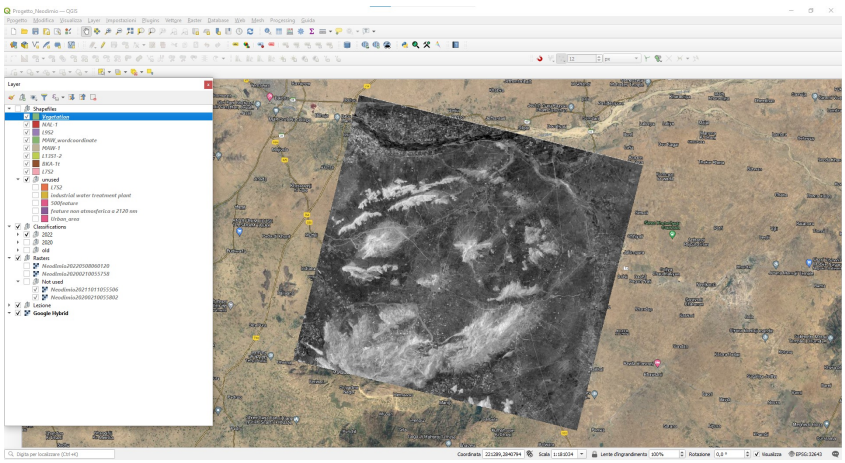

Figure 3.17: *An example of the interface of the QGIS program, in this case we can see how it is managed the data of a project inside the program: on the left there are the layers that can be activated on the general raster of "Google Hybrid satellite image" on the right.*

To import in this environment the hypercubes of PRISMA (provided by ASI from their website) I used the plugin EnMAP toolbox that is a plugin of the GIS environment developed by GFZ (Deutsches Geoforschungszentrum, science lead).
In Figure 3.18 is shown the graphical user interface of the Lipari and Elba island project (section 4.3) in the EnMAP Toolbox plugin.

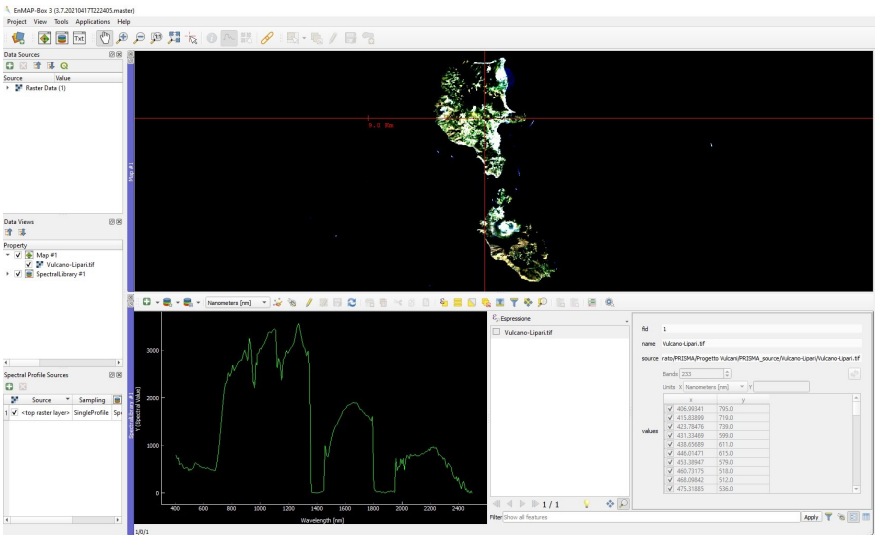

Figure 3.18: *An example of the interface of the EnMAP Toolbox plugin, in this case we can see how it is managed the data of the Lipari and Elba island project (section 4.3) inside the plugin: on the left there are the layers that can be activated in the same way of Fig 3.17. In the center it is possible to see the PRISMA satellite raster image (top panel) and the spectral signature of pixel (or pixels) of the raster in the graphical form of Reflectance vs wavelength and in the column data of X [Wavelength] and Y [Pixel PRISMA value (ADC counter)].*

IGOR

Details of spectral signatures used in this work are analyzed by the IGOR software of Wavemetric inc. This software is also used to perform plots and mathematical operations on spectral features collected manually from the raster.

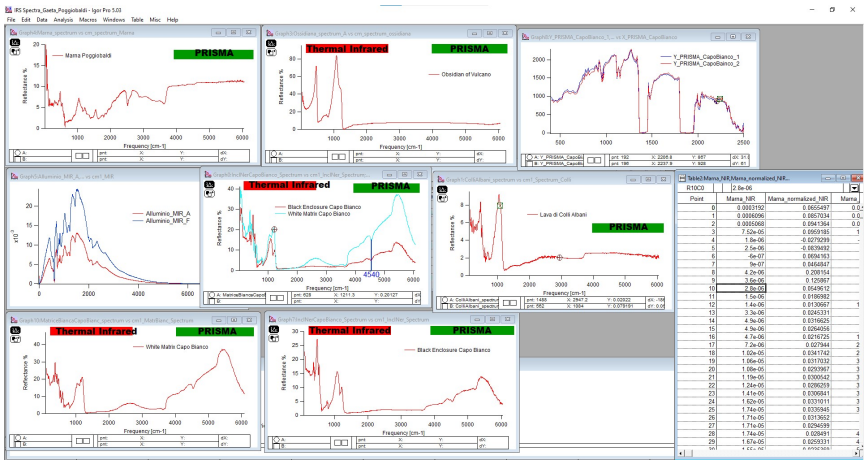

Figure 3.19: *An example of the interface of the IGOR program, in this case we can see how it is managed the data of volcanic rocks analyzed with the FTIR and the satellite PRISMA data of the same locations of the samples.*

To reshape text data of the PRISMA satellite in a format compatible with the IGOR software, the python programming and Microsoft Office excel are used.

IRIS

In some projects of this document (like the case of study of Appia Antica park of section 4.7) a change detection between the Structure Similarity Index Measure (SSIM) of two different images is performed. To accomplish this goal, the IRIS software (developed by NHAZCA srl.) is used. In image 3.20 it is shown the interface of IRIS software. For what concerns the input and output images obtained with this software, it is discussed in details in section 4.7

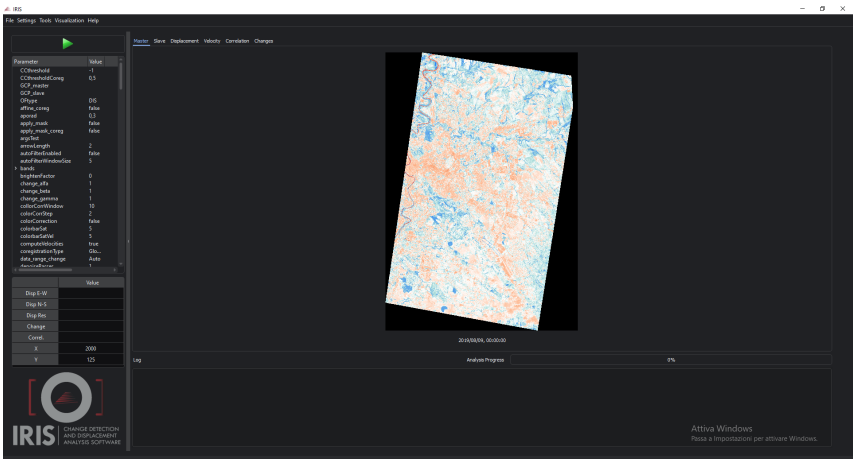

Figure 3.20: *An example of the interface of the IRIS software, in this case it is shown a false-color image of Codigoro (Ravenna, Italy) loaded as Master image.*

Xeneth

Infrared cameras used in section A are controlled by the official software of Xenics industry: Xeneth. In image 3.21 it is possible to see an example of the interface of the software.

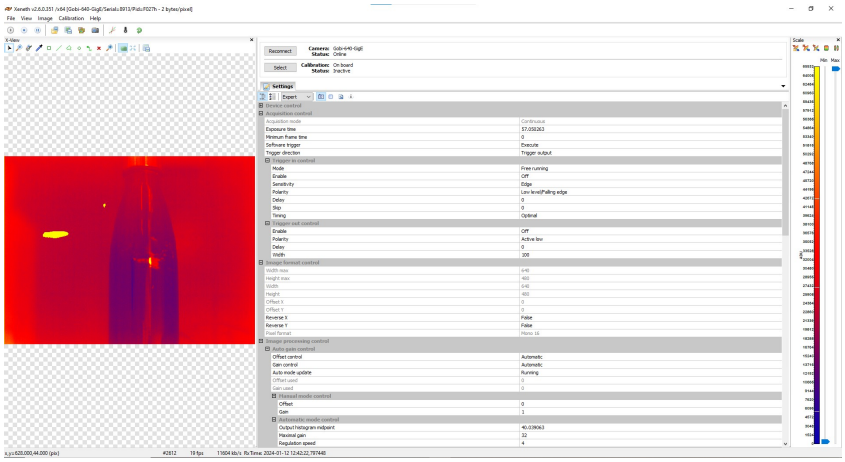

Figure 3.21: *An example of the interface of Xeneth64 (the version of Xeneth at 64 bit for Windows 10 and above) during an acquisition of the Long Wavelength Infrared camera Gobi, the image (on the left) is in false-color and it is possible to change all settings of acquisition (in the center) and the sliders of the chromatic color bar (on the right).*

Chapter 4

Image Analysis

This chapter shows the database of the work and their analysis. Seven different case of studies are considered, each one progress and improvements during the development of the thesis.
The last case of studies (section 4.7) is an exception which does not concern the main topic of the thesis (analysis of vibrational features in the shortwave infrared from a satellite) but rather carries out a hyperspectral analysis from a satellite in another electromagnetic range (the visible - near infrared). Since this experiment led to mostly satisfactory results, it was reported as an additional result of the hyperspectral analyses contained in this thesis.

4.1 Air Quality (Malagrotta rubbish dump)

This first case represents the only one in which PRISMA satellite proved unable to achieve a correct analysis, but we describe it nevertheless, because it is instructive to understand the huge difference between gas-phase spectroscopy and solid-state spectroscopy. This is due to the relative low spectral resolution of the satellite which is unable to resolve the roto-vibrational line of the gasses (except rare cases [45] in which the concentration of methane within the atmospheric column is so high that the signal-to-noise ratio remains high).
A satellite that performs better concerning the analysis of air quality is Sentinel 5P with its TROPOspheric Monitoring Instrument (TROPOMI) detector that consists of a spectrometer with a spectral resolution of 0.25 nm and 5 km of spatial resolution to collect enough photons for this relatively high spectral resolution.
Each pixel of the satellite image is about 5 km projected on the ground, but this is not a problem for atmospheric studies because gases have a high diffusion in their medium (the atmosphere). As we will see in the next subsection this is unacceptable for mineral mapping (rocks do not diffuse with the high rapidity of gas and could be localized on the ground) but with a better spatial resolution (30 m for the PRISMA satellite) it is necessary to have a worse spectral resolution (9 nm as we have said before). This is not a problem as rocks do not experiment rotational bands like gases and for this work we only need to analyze the overtones and the combination bands of the vibrational lines.
In figure 4.1 it is possible to see the spectrum of methane gas included in the HITRAN database. The cyan rectangles represent the broadness of a single PRISMA channel, which emphasizes how difficult it is to perform a classification with broad spectral bands that necessarily goes to mix

contributions due to landfill gas with bands that do not show this contribution.

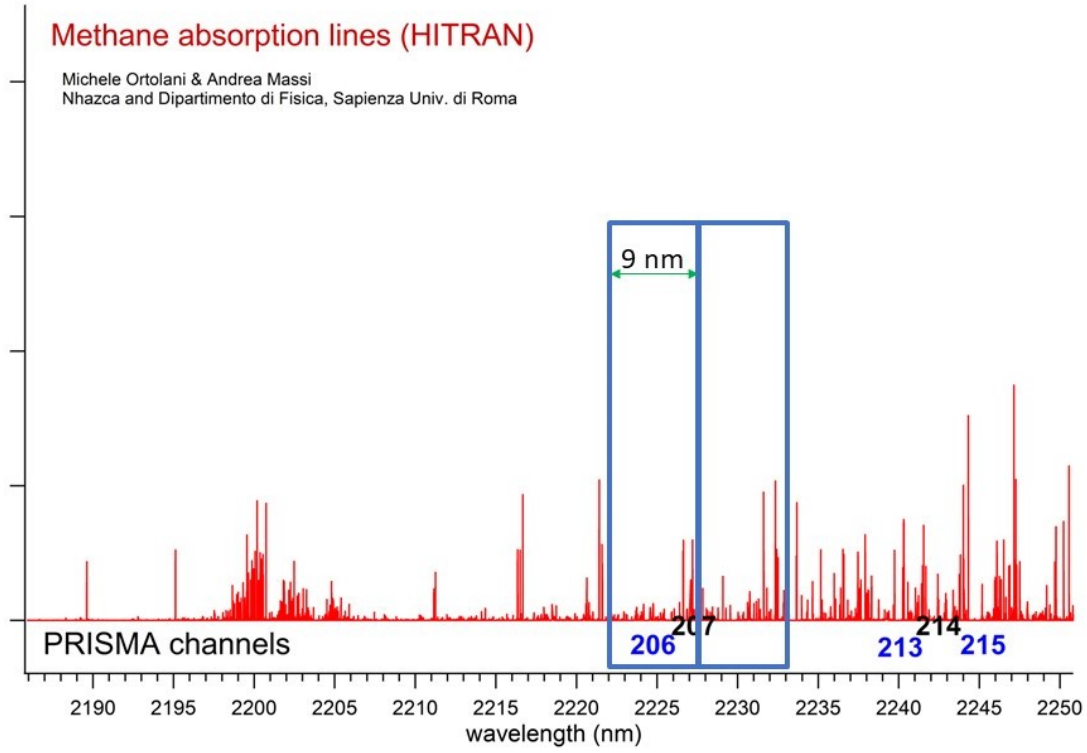

Figure 4.1: *Spectral signature of a sample of methane gas from the HITRAN database. Cyan rectangle represents the broadness of a PRISMA channel, in the figure we have drawn the channel 206 and 207 of the satellite centered respectively at 2225 and 2230 nm*

.

4.2 Moraines/Glaciers (Gran Paradiso)

The Gran Paradiso massif is a mountain massif in the Western Alps located entirely in the Italian territory, between Valle d'Aosta and Piemonte. The case study is chosen for the high lithological uniformity: gneiss, a metamorphic rock, dominates the lithological map in Figure 4.3c (dark red color areas) with some amphiboles, like serpentinite (green color areas in Figure 4.3c). A legend of these colors is present on figure 4.3c-a (top right corner of figure 4.3).
In this work, we have developed a mathematical algorithm that calculates the discrete derivative in a Geographic Information System (GIS) environment. The Discrete Derivative Algorithm (DDA) is applied to each spectrum, in a given datacube, twice: once on the descending slope of a known vibrational spectral line in the reflectance spectrum of gneiss, centered at 2222 nm, formed by 10 subsequent channels starting at 2151 nm (see Figure 4.2), and once on the ascending slope of the same line (9 reflectance data points starting at 2222 nm). The sum of the absolute value of the two derivatives, obtained from a total of 18 channels, is then combined in a vibrational line intensity score, which is then plotted in the map of Figure 4.3e.

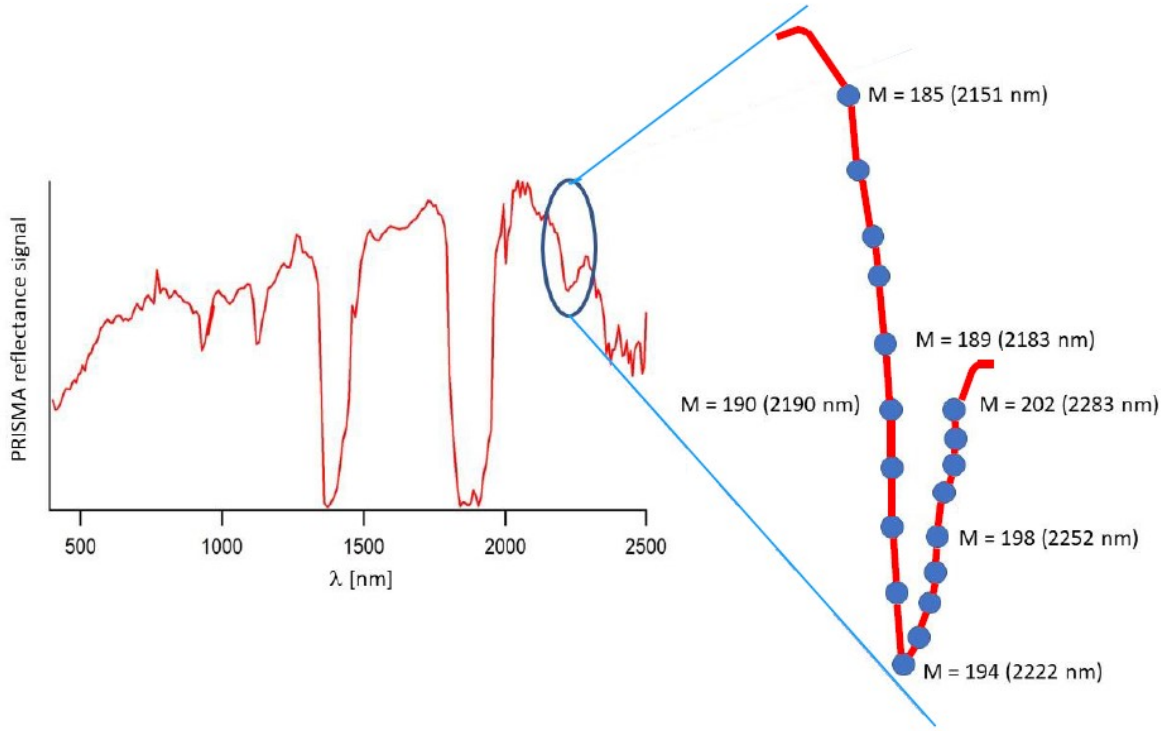

Figure 4.2: *A plot of the discrete derivative algorithm performed on a spectral feature, in this case the feature, zoomed in the right part of the image, is centered on 2222 nm that is the center of the 194^{th} band of the PRISMA satellite*

.

The equation of this classification algorithm is therefore:

$$Classification\ Score = -\left(\sum_{i=(M-4)}^{M-1} \frac{Ch_M - Ch_i}{M-i} + \sum_{j=M+1}^{M+4} \frac{Ch_j - Ch_M}{j-M} \right) + \tag{4.1}$$

$$+ \sum_{i=(N-4)}^{N-1} \frac{Ch_N - Ch_i}{N-i} + \sum_{j=N+1}^{N+4} \frac{Ch_j - Ch_N}{j-N}$$

where, in this case for the feature of fig 4.2, Ch_M is the channel 190 of the satellite centered at 2190 nm and Ch_N is the channel 198 centered at 2252 nm.

The main goal of this analysis is to map moraines in a recently melted glacier area of the Granparadiso area (image in Figure 4.3a). A moraine is a particular form of accumulation of sediments made up of rocky debris transported by the slow but constant sliding motion of a glacier due to gravity.
Figure 4.3e shows our spectral line intensity score, which should correspond to the density of gneiss minerals exposed to air, i.e. not covered by organic soil or snow, which we identify with moraine. For comparison, Figure 4.3d shows the normalized difference (A – B) / (A + B) between the spectral line minimum (point A, 2222 nm) and one point of the reflectance baseline (point B, 2283 nm). This is typically done in multispectral satellite imaging where only a few channels are available, moreover with extremely poor spectral resolution (two example of multispectral satellite are the

satellites Sentinel 2 and Landsat 8 described in the introduction of the thesis). Here, the spectral resolution of the two channels is still high enough to identify most of the moraines in Figure 4.3c, however, the moraine highlighted by the red circle is totally missed by the two-channel map of Figure 4.3d, while it is fully captured in our derivative map in Figure 4.3e. One can see that our derivative algorithm is noisier than the two-channel index, due to the discrete derivative calculation. Also note that glaciers have retreated from 1959, date of the lithological chart in Figure 4.3c, compared to the PRISMA acquisition of 2021. Snow-covered glacier surfaces (white areas in the visible image of Figure 4.3a) are undefined in the two-channel map of Figure 4.3d (division by zero problem due to low SWIR reflectance of snow), while in the discrete derivative method, figure 4.3e, these pixels may be correctly classified as snow (black pixels), and not as moraines (white pixels). In conclusion, our normalized derivative score of Figure 4.3e is noisier than the two channel difference index of Figure 4.3d, but it can be correctly calculated even in the presence of a low reflectance signal. This leads to a more specific usage of the absorption line of the spectral signature (rather than the classical multispectral Normalized Difference Two Points) that in this work is used for improving the mineral mapping (which consists in the recognition and localization of the lithology on the satellite image starting from the analysis of the pixels of the image itself). However, in other tasks it could be used, for example, to monitor minerals concentrations in a time series data and other features that rely on the SWIR region in a more effective way in the Hyperspectral Imaging.

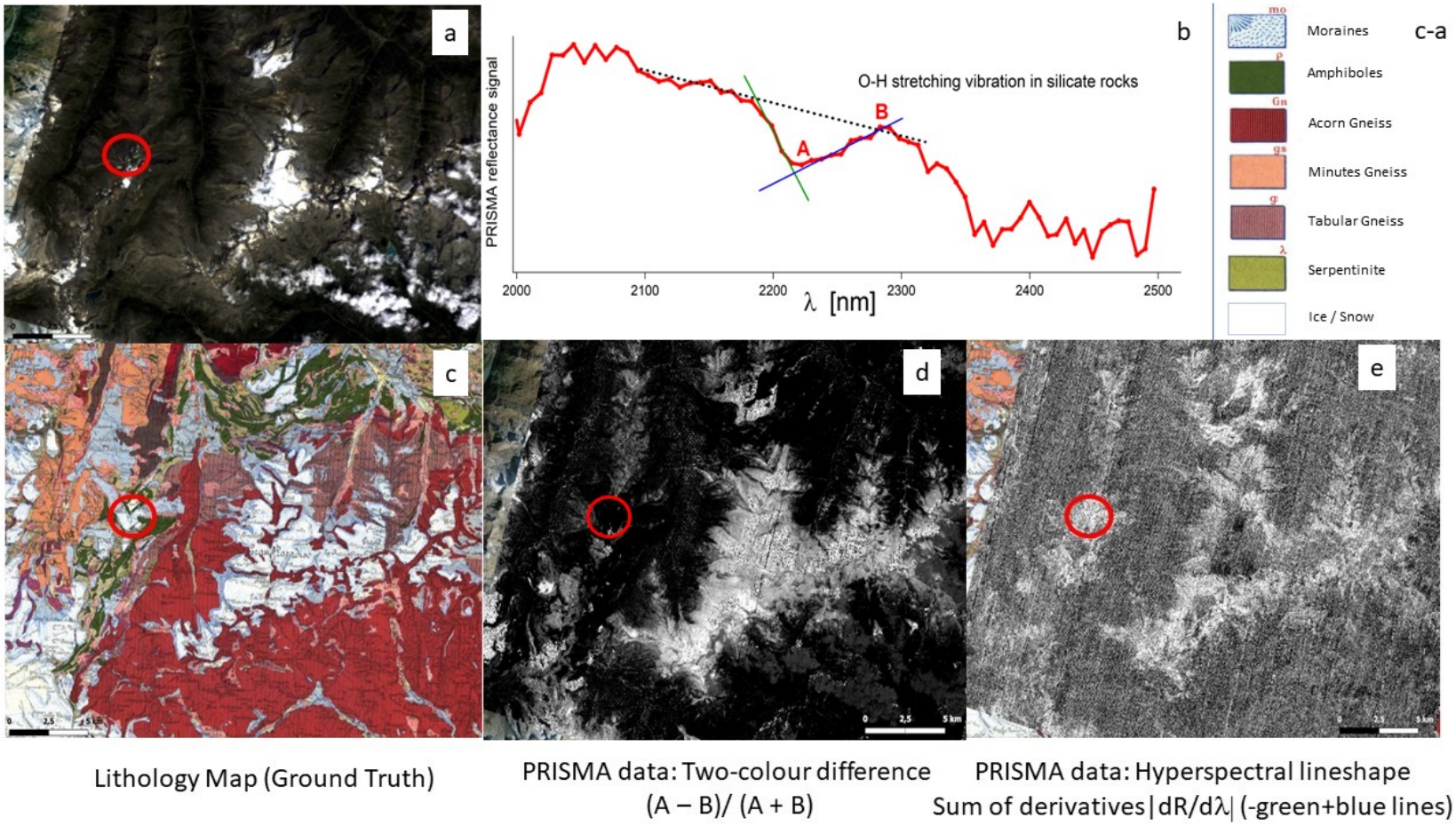

Figure 4.3: *(a) True-color image of the PRISMA datacube, the image is rearranged in the following Red Green Blue (RGB) bands: band 33 (centered at 674 nm) as Red, band 23 (centered at 584 nm) as Green and band 12 (centered at 497 nm) as Blue. (b) Spectral signature of a PRISMA satellite moraine pixel, the green solid line and blue solid line emphasize the left and right slopes respectively of the absorption line. The DDA calculates the discrete derivative of these two slopes to perform the localization of moraines in the satellite image (mineral mapping application). A and B are the channels centered at 2222 nm and 2283 nm respectively and used for the two-point normalized-difference classification. (c) Lithological map at the scale 1 to 100000 used as ground truth. The chart is provided by Istituto superiore per la protezione e la ricerca ambientale (ISPRA) here is the hyperlink to the catalog [ISPRA hyperlink] (d) An attempted two-point normalized-difference classification starting from the same hyperspectral datacube. The algorithm calculate (A - B) / (A + B) for all pixels of the image. Black pixels indicate a low score while white pixels indicate a high score (e) The output of our discrete derivative-based spectral line intensity score. High-score (white) pixels correspond almost perfectly to moraines not covered by soil or snow (white and light blue pixels in the ground truth Figure 2c). The red circle identifies an area that by validation of the lithological map corresponds to moraines (in 1959, year of the lithological chart, this area was covered with snow, but in 2021 from the RGB image of PRISMA the area is not covered anymore) but it is not recognized by the two-point normalized-difference classification, while it is from the discrete derivative algorithm. Making a comparison between figures 4.3d and 4.3e and using figure 4.3a as validation, we can also see that the pixels that are totally covered in snow are correctly recognized as not part of the moraines in fig 4.3e, while they appear confused in 4.3d due to the instability of the formula of two-point normalized-difference for low reflectance value of snow in A and B bands.*

We can conclude this part of the work by stating that: this first result of the thesis based on the spectroscopy analysis of the vibrational feature at 2222 nm highlights the rocky areas discovered by the retreat of the glaciers. This provides an application of mineral mapping in detecting moraines and also useful climate change data, due to the fact that it shows the retreat of the glaciers as a different area covered by the glaciers in the 1959 lithological map and in the PRISMA satellite image acquired in 2021.
This work also provides a comparison between the multispectral methodology (commonly used for earth observations with multispectral satellite data before the arrival of hyperspectral imaging) and the spectroscopy methodology used for hyperspectral satellite data. This reveals how the hyperspectral methodology effectively manages not only the identification of areas of the moraines that the multispectral methodology is unable to recognize, but also distinguishes rock from snow/ice (a feature which is instead quite confusing in the multispectral methodology of the two-point classification due to the instability of the denominator as water/ice pixels have low reflectance in the bands affected by the algorithm).

4.3 Silicates under vegetation (Vulcano and Lipari islands)

In this case study we have tried to perform mineral mapping also for pixels that are partially covered by vegetation (it must be noted that this is the greatest problem of hyperspectral imaging beyond the poor geometrical resolution: vegetation heavily affects the detection of the spectral signatures). Before presenting the algorithm that was developed to achieve this goal, it is necessary to introduce the Red Edge (RE) that we use to recognize vegetation in the satellite image and the presence of rhyolite (RP), which we measure with a score calculated as a discrete derivative as it was done in section 4.2.

As we will see in section 4.7, the absorption of chlorophyll in the red-to-infrared range (so-called Red Edge) is a very clear spectroscopic feature that can be used to emphasize pixels of the satellite image that are covered by vegetation (vegetation mapping). The rhyolite instead, is the most silica-rich of volcanic rocks and for this reason represent an effective target for mineral mapping of volcanic areas (hydroxylated silicates have the spectral signature in the SWIR range deeply affected by the combination bands due to the hydroxyl groups attached to the structure of the rock, usually presented as a tetrahedral structure as seen in chapter 2).
To accomplish this goal a suitable weighted algorithm is developed given by the following formula

$$C_s = (RP_s - Off_{RP}) * \frac{RE_s}{Off_{RE}} \tag{4.2}$$

where C_s is the score that indicates the presence of the rock of interest in the image despite the presence of vegetation, RP_s is the score that indicates the rhyolite presence given by the same discrete derivative algorithm of the previous cases of study, Off_{RP} is an offset that is manually inserted from the fact that even in the case of totally absence of rhyolite spectral feature in the pixel, the value of RP_s is not zero (Off_{RP} is about 2,086 and represents the minimum value of

the RP_s for a pixel that is not in the sea or in anomalous areas), RE_s is the score that indicates the presence of the vegetation given by the discrete derivative calculus of the red edge slope in the spectral signature of a pixel and Off_{RE} is an offset that is manually inserted from the fact that even in the case of totally absence of vegetation in the pixel, the value of RE_s is not zero (the value of Off_{RE} is about 1.266 and it is calculated from the minimum value of Red Edge Score that is not in the sea).
This algorithm has the objective to null the signal if the vegetation cover of the pixel is 100% and emphasize regions that has some characteristics of the spectral signature even if there is a presence (but not the totality) of vegetation.

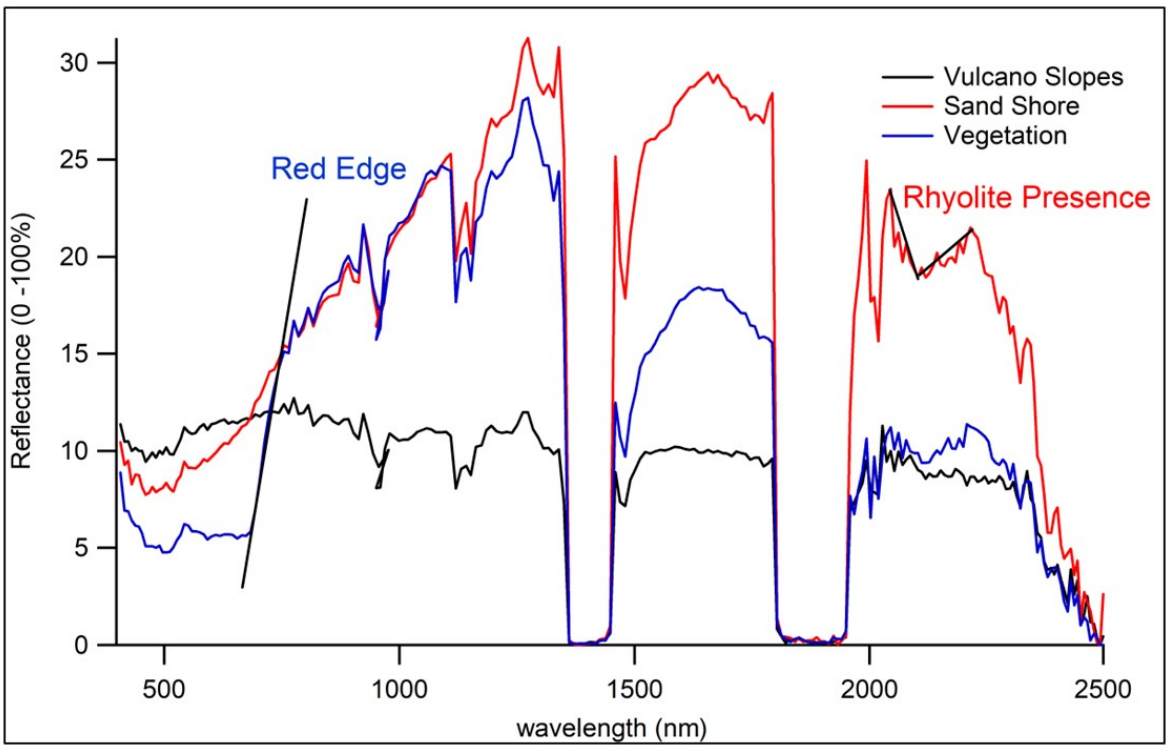

Figure 4.4: *The spectral signature acquired in the PRISMA satellite image of Lipari for: a vegetation pixel that is easily characterized as vegetated pixel from its high slope in the red edge spectral range (blue solid curve), a pixel that contains the mineral of interest (red solid curve) and a pixel without the previous SWIR feature or high red edge slope so a non vegetated pixel that is not supposed to contain the mineral of interest (black solid curve).*

In figure 4.5 it is possible to see a general overview of the project results with a comparison of the True-color image of the PRISMA datacube (used as validation for vegetation mapping for green areas), the Score map of the discrete derivative algorithm of the slope in the red edge spectral range (red edge line of figure 4.4), the Lithological map (used as ground truth for mineral mapping), the Score map of the discrete derivative algorithm calculated in the rhyolite vibrational feature (the feature is marked as Rhyolite Presence of figure 4.4) and the Score map of the equation (4.2). The latter one shows, by looking at the area included in the cyan-colored circle, the progress of areas containing the mineral of interest but which are not effectively detected using the mineral mapping algorithm alone because they are partially covered by vegetation (while instead, due to the improvements made by the equation (4.2), they are clearly visible as a result of the algorithm).

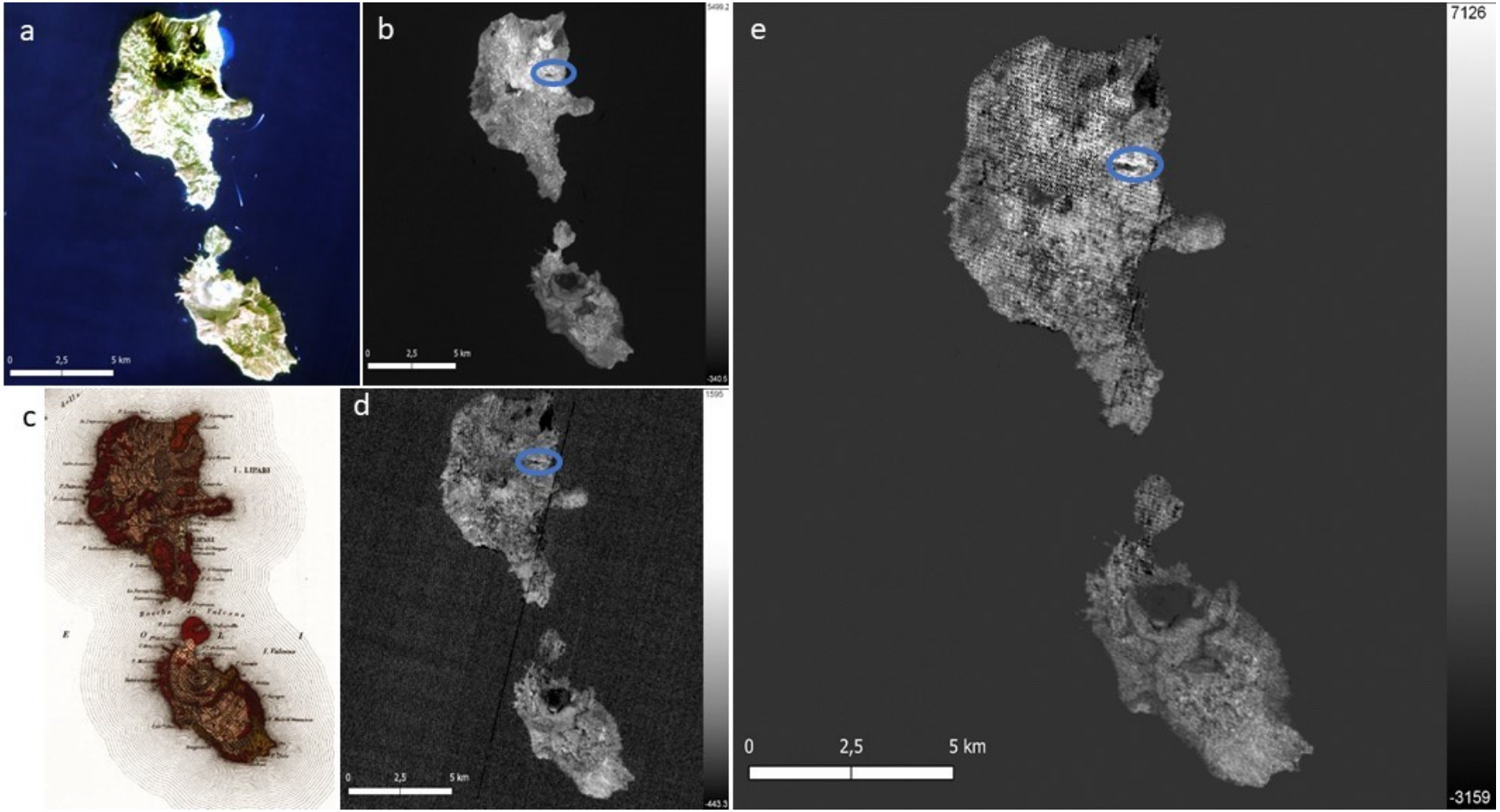

Figure 4.5: *An overview of the results of this section. (a)True-color image of the PRISMA datacube, the image is rearranged in the following Red Green Blue (RGB) bands: band 33 (centered at 674 nm) as Red, band 23 (centered at 584 nm) as Green and band 12 (centered at 497 nm) as Blue. (b) Score map of the discrete derivative algorithm of the slope in the red edge spectral range (red edge line of figure 4.4). Using green areas of figure 4.5 as validation, we can see that the algorithm effectively emphasize the vegetation areas. (c) Lithological map at the scale 1 to 100000 used as ground truth for mineral mapping. The chart is provided by Istituto superiore per la protezione e la ricerca ambientale (ISPRA) here is the hyperlink to the catalog [ISPRA hyperlink] (d) Score map of the discrete derivative algorithm calculated in the rhyolite vibrational feature (the feature is marked as Rhyolite Presence of figure 4.4).(e) Score map of the equation (4.2).The cyan circle emphasize an area that is barely visible in 4.5b (so partially but not totally covered by vegetation) and almost absent in 4.5c (due to the presence of vegetation in the pixels of this area), so the cyan circle in figure 4.5e represents an area where there is the presence of rhyolite, but it is not detected from the discrete derivative algorithm of map 4.5b due to the partial coverage of vegetation, while it is effectively detected from the equation (4.2) as we can see from the output 4.5e.*

Figure 4.6: *(Left) Score map of Rhyolite presence in a red color scale (dark red pixels have a low score and present no feature around 2100 nm, while light red pixels have a large score).(Middle) Score map of Red edge slope score in a green color scale used as vegetation mapping (dark green pixels have low score which means absence of vegetation, while light green pixels have a large score, this could be easily seen making a comparison with the true-color image (figure 4.5a). (Right) The RG image obtained by using image 4.6a as red component and 4.6b as green component, dark pixels has a low scores in both components, while yellow pixels have high scores in both components.*

To conclude this part of the work we can show that we investigated the possibility of curbing one of the biggest problems of hyperspectral imaging: the fact that it is not penetrative, i.e. if the object of analysis is covered by vegetation, the spectral signature acquired by satellite will be related to the vegetation and not the object of interest. To resolve this issue, we personally developed an algorithm that acted as spectral unmixing between the mineral that must be classified and the vegetation in the pixels where both these components were present.
The result, validated with the RGB PRISMA acquisition for the green cover and a lithological map for the presence of the mineral, was satisfactory and highlighted areas that were not present in the mineral presence map alone and not evident in the vegetation map (therefore avoid mistaking vegetation for mineral, class differentiation is a main problem in spectral unmixing algorithms).
In addition to this algorithm, there is also a further linear unmixing spectral algorithm which uses the map of the presence of the mineral as a Red component, and the map of the vegetation as a Green component. This to create an image with two components in which it is highlighted where a component is dominant compared to the other (red pixels indicate the dominant presence of mineral while green pixels the dominant presence of vegetation), where both components are very high (yellow pixels) and where both components are very low (dark pixels)

4.4 Monuments made of marble with laboratory ground truth (Rome)

In this case of study, we decided to measure the absolute lineshape of vibrational features by applying a spectroscopy reference to produce an absolute reflectance spectrum, similar to what is done for laboratory FTIR spectroscopy.
The FTIR extracts spectral signature by performing a normalization of the power spectrum of the reflection of the normal incidence on the sample with the power spectrum of the reflection of the normal incidence on a reference (a material with high broadband and spectrally flat reflection in the electromagnetic spectrum range of interest). In this way it is possible to emphasize vibrational spectral features, obtaining the absolute spectral signature of the sample.
The aim is to perform the same spectral reference procedure that is typically done in a FTIR laboratory but starting from satellite data and then making a comparison with the results in laboratory. The sample in the laboratory is a fragment of a brick of travertine limestone. For what concerns the reference, we use a polished plate of aluminum.
The spectral signature extracted with the FTIR is shown in Figure 4.7. The green rectangle indicates the operative range of the PRISMA satellite (from visible to the SWIR range) while the red rectangular indicates the thermal infrared region in which it is possible to observe pure phonons signal of the sample. We are interested in the two spectral features emphasized by the green lines, in particular only the green line at 2.3 μm is detectable from the satellite because the other feature present in the SWIR at 1.9 micrometer is covered by the atmospheric absorption. From literature ([4]-[5]) the line at 2.3 μm ($4290 cm^{-1}$) is a pure phonon of calcium carbonate ($CaCO_3$) at 7 μm ($1430 cm^{-1}$) in the medium infrared range promoted to higher energy by the overtone phenomenon ($3\nu CaCO_3$). From the fact that figure 4.7 is a plot in wavelength, qualitatively, the precise calculus has been performed in frequency, it is possible to recognize the feature at 2.3 μm dividing the

feature at 7 μm for three.
The reasons that force the operative range of the satellite to stop at 2.5 μm losing the large quantity of structural information that are present in the thermal infrared range are basically two:
- i) the signal to noise ratio could be too low due to the photon energy and the relatively dense spectral sampling and, from the fact we are interested in localizing regions projected on the ground, the option to worsen the spatial resolution, increasing in this way the number of photons that are caught from the detector, is not viable (except for rare cases of large areas in the world constituted only by one or few materials, in almost all observations too many elements could overlap their spectral signatures with each other)
- ii) even if the reason i) alone could be enough to make direct measurements of hyperspectral data beyond the SWIR range impossible, to this problem we have to add the spectrum of sunlight and the presence of the atmosphere that absorbs the signal more than along the SWIR range
- iii) in laboratory the sample could be lapped or chosen as composed by only one mineral and it is possible to perform an optimization of the orientation of the sample respect to the light of incidence of the source.

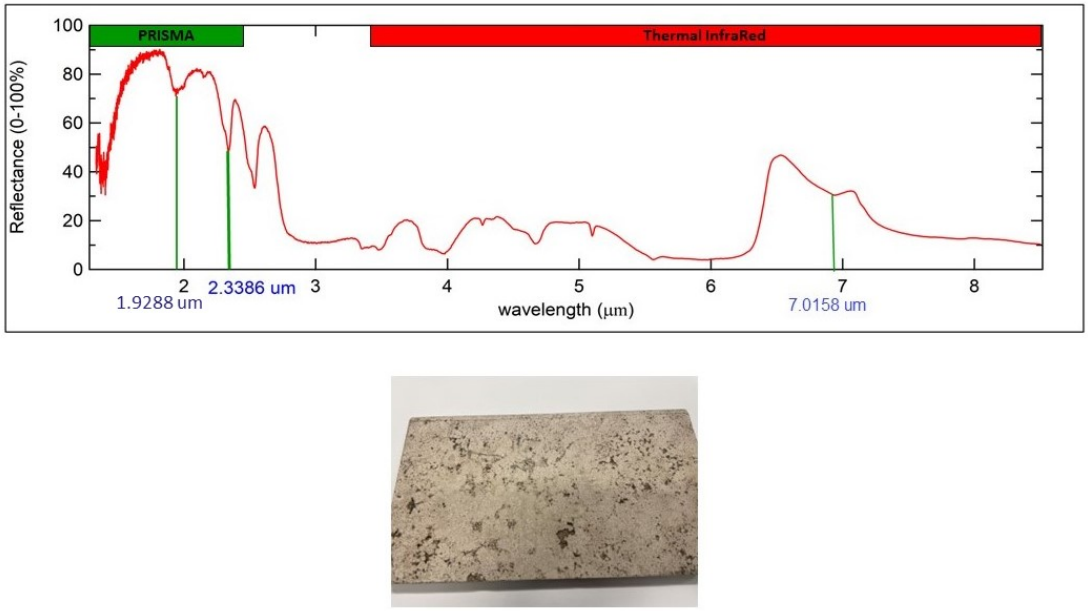

Figure 4.7: *The spectral signature of the travertine limestone extracted by the FTIR with an image of the source of the fragment used as sample. The green rectangle emphasizes the operative spectral range of the PRISMA satellite (from visible to SWIR) while the red rectangle emphasizes the range in which pure phonons are detected in laboratory but not accessible from the satellite. In the spectral signature, a green bar emphasizes the pure phonon concerning the calcium carbonate at 7 μm ($\nu_{CaCO_3} = 1430cm^{-1}$) and its overtone at 2.3 μm ($3\nu_{CaCO_3} = 4290cm^{-1}$). Another feature within the PRISMA operational range (1.9 μm) is highlighted, but this feature is not detectable by the satellite because it is absorbed by the atmospheric presence.*

From satellite data, we have chosen a case study that is composed almost exclusively of travertine limestone: a very large monument in the center of Rome (130 $\times$ 135 meters) called "Altare della Patria" composed by "botticino marble", a form of the travertine stone.

As reference, we used the coverage of the Olympic stadium, of the city of Rome. This coverage consists in a paste of glass fiber as the substratum of a polytetrafluoroethylene (PTFE) layer. This layer reflects the radiation in a broadband and spectrally flat manner in the spectral range of interest (there are no absorption peaks and we assume no transmission, so it results in a total reflection of the signal).

Before showing the results of "Altare della Patria," we checked the validity of this experiment using another monument in Rome as a test: the "Marble Stadium." This monument not only has targets of the same material as "Altare della Patria" but also falls in the same satellite acquisition as the Olympic Stadium by PRISMA (i.e., it is contained in the same satellite footprint as we can see from figure 4.8) to try to reproduce the same measurement conditions between sample and reference during the extraction of the spectral signature from the satellite image.

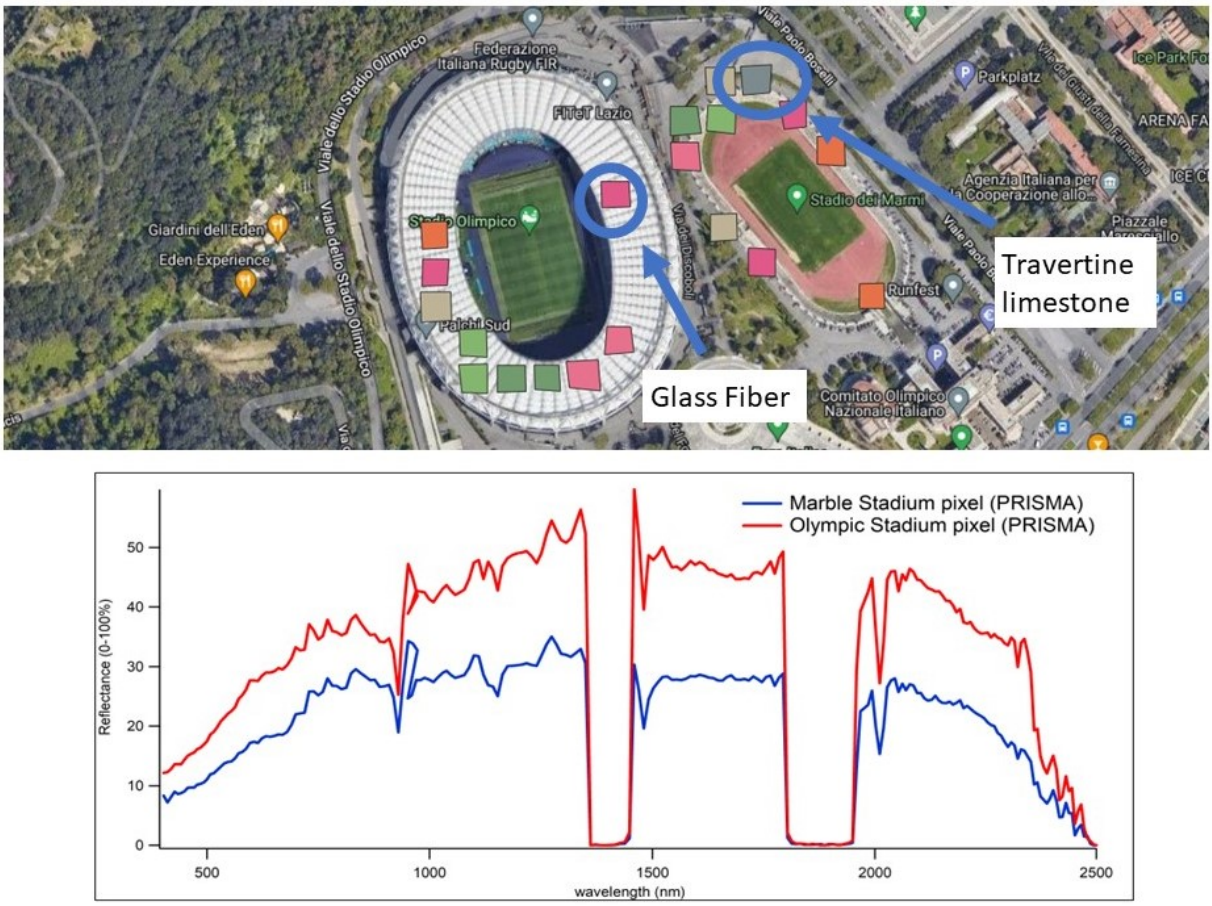

Figure 4.8: *(Top panel) The pixels of the marble stadium, built with Travertine limestone and the pixels of the Olympic stadium, covered with a glass fiber and PTFE. Cyan circles emphasize the pixels in which spectral signatures has been extracted and shown in the bottom panel. (Bottom panel) Spectral signature of a travertine limestone pixel (blue solid curve) and spectral signature of a PTFE pixel used as mirror (red solid curve), as expected we can see that the reflection of PTFE pixel is greater than travertine pixel and for this reason the choice to use it as mirror of reference for the travertine pixel is valid*

.

In fig 4.9 we showed a comparison between two spectral signatures on the overtone of calcium carbonate at 2.3 μm ($3\nu_{CaCO_3} = 4290cm^{-1}$): travertine limestone in laboratory (its entire spectral

signature, and the source from which the sample was taken, is shown in Figure 4.7) and travertine stone from satellite (the pixel from which the spectral signature was taken, is marked as "Travertine limestone" in the upper panel of figure 4.8. As we can see from fig 4.9). The signal is clear in both spectral signatures, reveling that SWIR features detected in laboratory can be detected also from satellite.

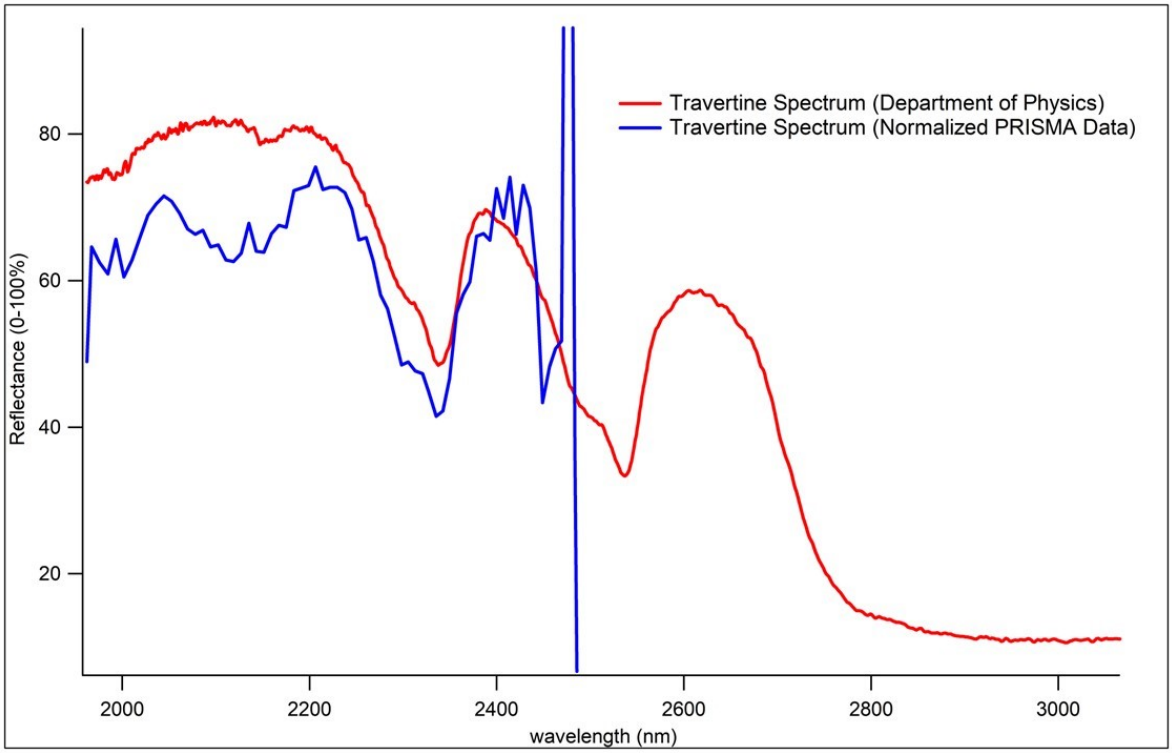

Figure 4.9: *A comparison between the normalized power spectrum of the travertine of a brick in laboratory with aluminum (red solid curve) and the power spectrum of travertine of Altare della Patria monument from satellite with the PTFE upper layer of Olympic stadium (blue solid curve).*

A common operation that is used in laboratory to characterize and extract the general spectral signature of a material is the averaging. Averaging consists in the multiple acquisition of spectral signatures of the sample and, after that, a mean of these measurements. With only one satellite image (PRISMA satellite is not a constellation and for this reason the revisit time is relatively poor and affected by different conditions of acquisition) this averaging is provided by acquiring spectral signatures of different pixels that share a similar spectral signature that it is supposed to be formed by the same material.

In figure 4.10 it is possible to see 20 pixels (we remember that each pixel is a projection of 30 m on the ground) that cover the entire monument and a part of a nearby church (Basilica di Santa Maria in Ara Coeli). These pixels are used to make an average of the travertine pixels that compose the monument in order to perform a smoothing of the satellite travertine spectral signature. This will make the spectral signature less noisy and more comparable with the measurement made in the laboratory. The center of the 20 pixels (represented by dots) and their spectral signatures are divided and colored by the different behavior in the different slope of the raw reflectance, in this way it is possible to distinguish the travertine pixels of the monuments (red dots with red spectral

signatures) from the brick pixels of the church present in the satellite image (blue dots with blue spectral signatures). The cyan dot in the upper right corner of the monument is a pixel covered by vegetation (and in the spectral signatures panel it is represented with the same cyan color, showing lower reflectance than the other pixels in the swir). The green dot of the monument represents a pixel in which the spectral feature of travertine limestone is particularly evident (its spectral signature is depicted with the same color in the spectral signatures panel).

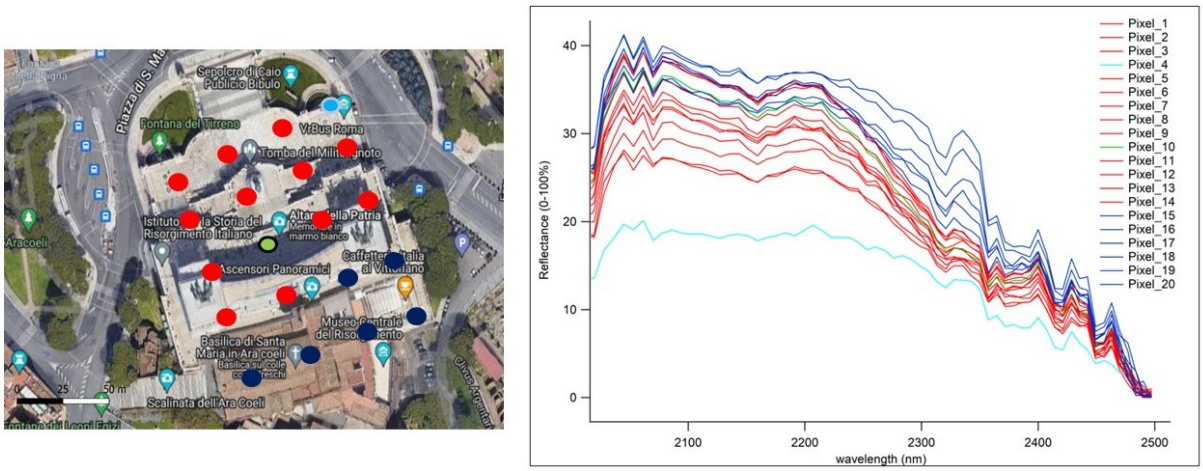

Figure 4.10: *(Left) Pixels of this monument in the center of Rome, red dots represent pixels that belong to Altare della Patria, blue dots pixels that belong to Santa Maria, the cyan dot is a vegetation pixel while the green dot is a pixel in which the spectral feature of travertine limestone is particularly evident.(Right) The spectral signatures of the pixels of left panels, red, blue, cyan and green curve belong to the same color dots of the left panel. Markers present outside the monument are meaningless for the purposes and belong to the geographical reference layer of Google hybrid satellite.In this figure we can already see how the different slope of the raw reflectance of the blue dots compared to the red dots allows us to distinguish the travertine pixels (red dots) from the brick pixels of the church present in the satellite image (blue dots), the subsequent normalization that will be shown in the next figure will highlight the presence of this feature that is around 2340 nm.*

In image 4.11 we can see the comparison of the results of Altare della Patria with the results of the laboratory. As we can see, if we normalize a pixel that has not the feature given by the overtone of calcium carbonate (i.e a vegetation pixel) after the normalization the feature is not emphasized at all (green solid curve in figure 4.11). The result of smoothing performs better in this case rather than the marble stadium (the smoothing is the red solid curve while the normalized single spectral signature is represented by the pink solid curve). In fact the smoothing not only erases some noisiness from the signal but also emphasizes the spectral feature compared to the spectral feature of a normalized single pixel (not smoothed pixel).

It would have been possible to apply the DDA to this data, but with less than 16 pixels for the monument we did not need a score to be calculated and visualized in GIS.

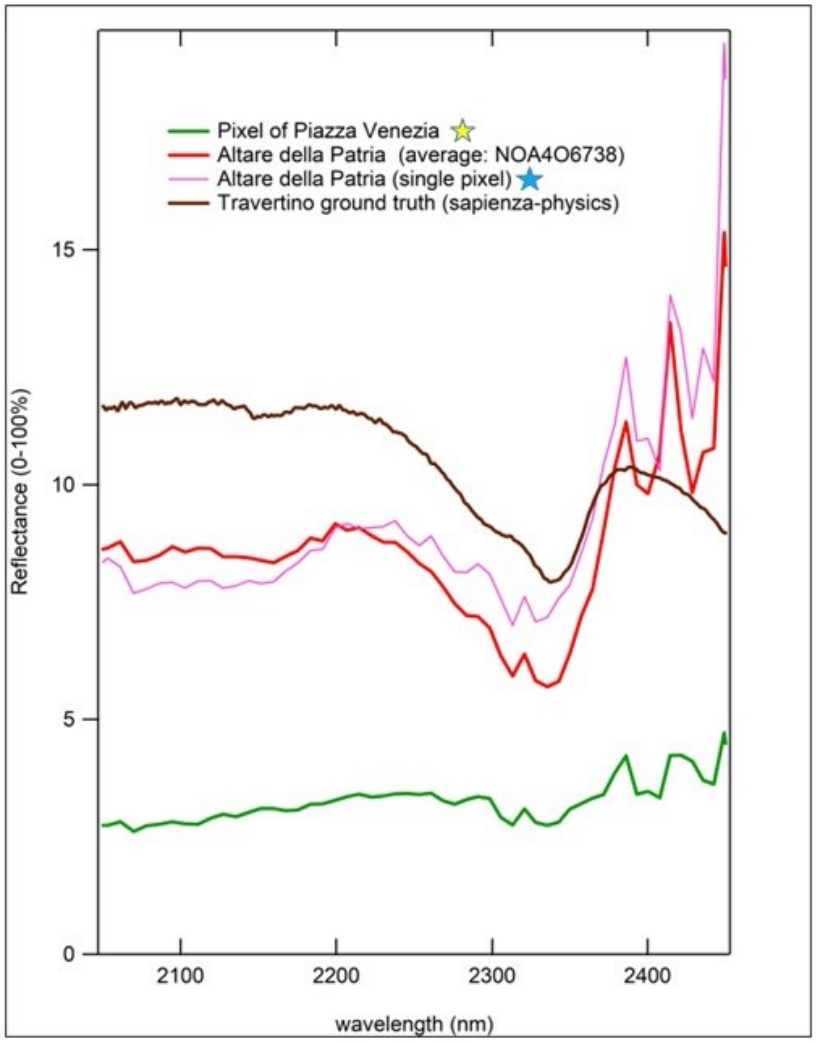

Figure 4.11: *(Left) A 3D google satellite image of the case study (the markers present outside the monument are meaningless for the purposes and belong to the image taken from Google Earth), the yellow star on the grass near the monument represents the pixel of the PRISMA satellite acquired as non travertine pixel to make a comparison with the travertine pixels (red dots of figure 4.10), the cyan star on the monument represents the pixel of in which the spectral feature of travertine limestone is particularly evident (cyan dot of figure 4.10).(Right) A comparison between the normalized spectral signature (green solid curve: not travertine normalized pixel, pink solid curve: single travertine normalized pixel, red solid curve: smoothing travertine normalized collection obtained as average of the red dots pixels of figure 4.10) with the spectral signature of the travertine extracted in laboratory (brown solid curve).*

As the final result of this section, we can make a comparison between the different acquisitions of the spectral signature of travertine limestone. In figure 4.12 there is a zoom in between different extraction of the spectral signatures of travertine limestone on the spectral feature at almost 2340 nm, the number is not exact because this number accorded different detectors with different spectral resolution in different conditions of acquisition (dust or rocky sample, laboratory in vacuum and satellite imaging) but for the object of this thesis, that is the hyperspectral imaging from satellite, it is not important that the feature is located at 2340 or 2342 nm because is smaller than the satellite spectral resolution (9 nm).

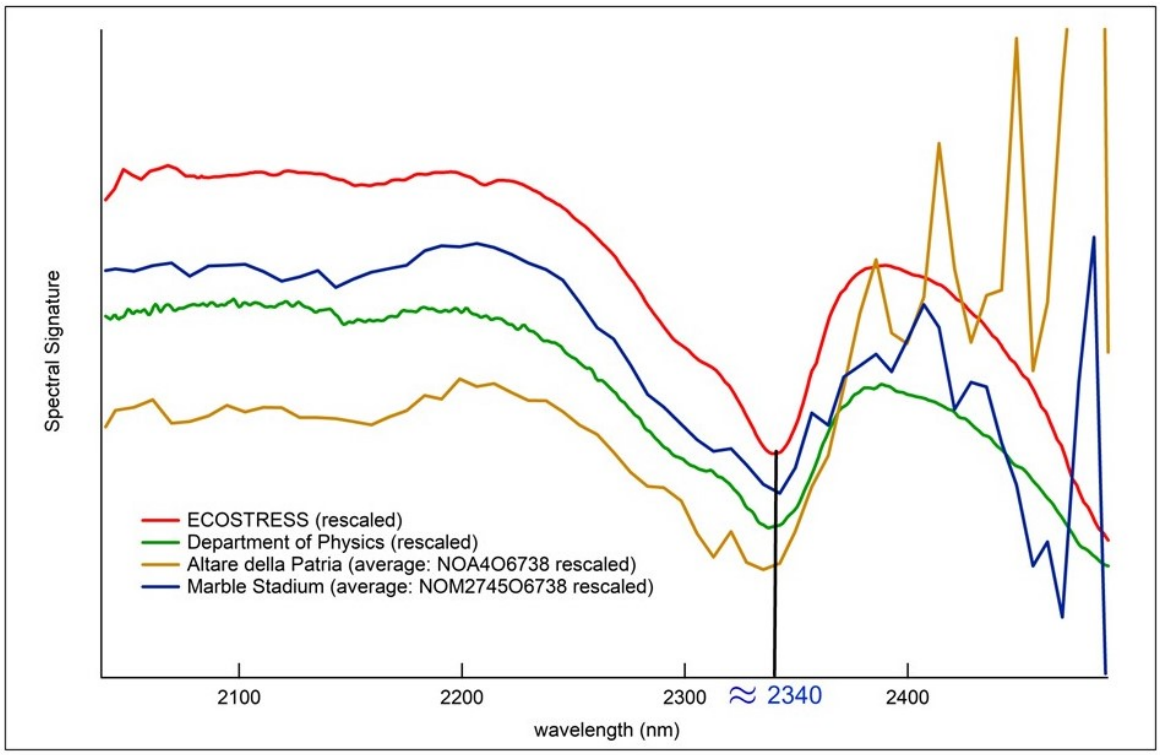

Figure 4.12: *A comparison of the travertine vibrational spectral feature measured from laboratory and satellite. Red solid curve: spectral signature of the travertine limestone from the ECOSTRESS spectral library database (from the information of the metadata, the experiment seems to be conducted with a dust sample). Green solid curve: spectral signature of the travertine limestone from the FTIR analysis of the department of physics (experiment conducted with a rocky sample inside the interferometer). Blue solid curve: smoothed spectral signature extracted by PRISMA from a collection of pixels that composing the Marble Stadium monument, Dark Yellow solid curve: smoothed spectral signature extracted by PRISMA satellite from a collection of pixels that composing the monument Altare della Patria.*

In conclusion to this work, and reassuming what has been done in this section, we can summarize the content as follows: in this part of the work, a direct comparison was made between the spectroscopic analysis conducted in the laboratory and the spectroscopic analysis of hyperspectral satellite data.
The laboratory part consists in extracting the spectral signature of a travertine sample with the spectrometer present in the laboratory and normalizing it with the spectral signature extracted in the laboratory of a material that acts as a reference in the spectral area of interest, therefore having high reflectivity in the SWIR and LWIR (in our case we chose a polished plate of aluminum).
The part relating to satellite data is carried out with the same methodology used in the laboratory, but using objects of interest and spectral references on the typical scale of satellite images. In this

case the object of interest to be analyzed in a pre-phase of feasibility testing is, in analogy with the fragment of travertine in the laboratory, a monument (the Marble Stadium) composed of Botticino marble which is the non-scientific name of travertine. The reference used to normalize the spectrum of the Marble Stadium was the coverage of the Olympic stadium which was within the same satellite image (i.e. it fell within the same footprint, which is the area framed by the satellite). The roof of the Olympic stadium is in fact made of a glass paste composed mainly of Polytetrafluoroethylene (PTFE commonly known as Teflon) which does not absorb infrared radiation and therefore has high reflectivity in this region of the electromagnetic spectrum.
Given the satisfactory results and in agreement with each other in this pre-test phase, we then proceeded to analyze a larger and more homogeneous monument in Rome (Altare della Patria) which was located outside the footprint of the Olympic stadium. On this last work, a smoothing of the spectral signature of the satellite data was also performed by averaging the spectral signatures of the pixels that made up the monument in the satellite image.
A general comparison was also carried out between the normalized satellite data of Altare della Patria, the normalized satellite data of Marble Stadium, the laboratory data extracted with the spectrometer of the physics department, and the laboratory data present in the ECOSTRESS Spectral Library database provided (from the info contained in the metadata of the spectral signature of the database) by reducing the sample to powder.

4.5 Open pit mine: detection of excavated areas (Bingham Copper Mine)

Another SWIR case study is the analysis of the largest open pit mine of the world: the Bingham Copper Mine. This case study has been chosen to demonstrate how hyperspectral imaging on the SWIR spectral range can perform mineral mapping operations better than the optical imaging in the case of a large case study composed mainly by only one material.

In figure 4.13 there is the RGB image of PRISMA acquisition of the case study and spectral signatures of three different clusters of pixels: one of the unexcavated rock of the mine that shows a broad structural feature (probably due to the combinations of multiple elements that they settled over time in these zones), one of the excavated rock (that represents the vibrational feature that we are looking for at around 2200 nm) and a cluster of pixels that shows no feature in the SWIR spectral range.

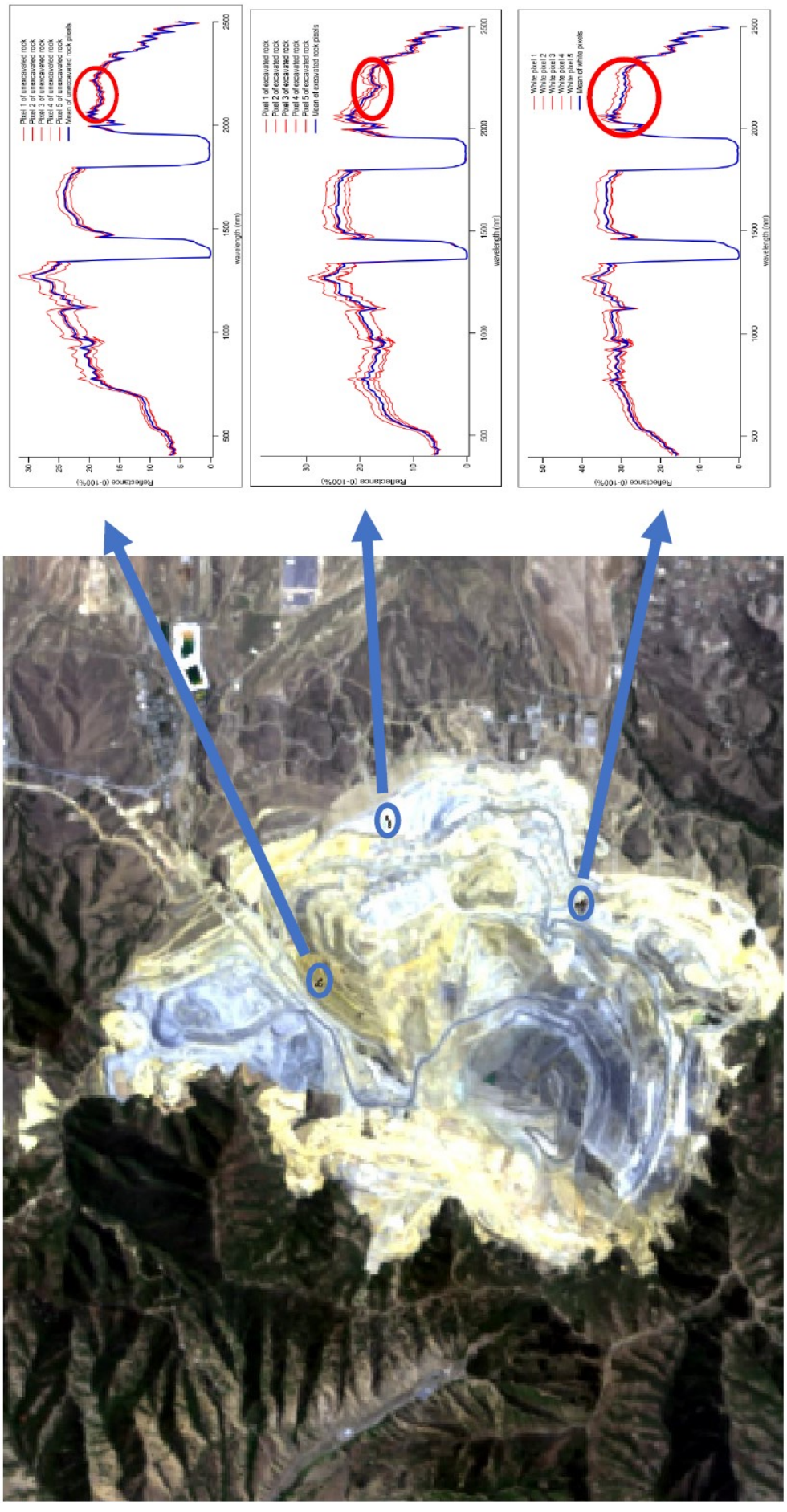

Figure 4.13: *(Left) True-color image of the PRISMA datacube, the image is rearranged in the following Red Green Blue (RGB) bands: band 33 (centered at 674 nm) as Red, band 23 (centered at 584 nm) as Green and band 12 (centered at 497 nm) as Blue. (Right) Spectral signatures of the clusters of pixels studied enclosed in cyan circles. From top to bottom, the classes of pixels enclosed by the circles are: (Unexcavated rock) that acts as contrast signal respect the excavated rock, (Excavated rock) that represents pixels in which the vibrational feature is present and (no spectral feature pixels) which have neither the vibrational characteristics of the excavated rock nor the characteristics of the unexcavated rock.*

To analyze the spectral feature we produced a score map of the vibrational line at 2200 nm and a score map of the broad vibrational line at 2130 nm (probably the combinations of multiple elements that sum each other in a linear and nonlinear combinations), these maps and the position of the spectral signature, in which the discrete derivative is calculated are shown in figure 4.14.

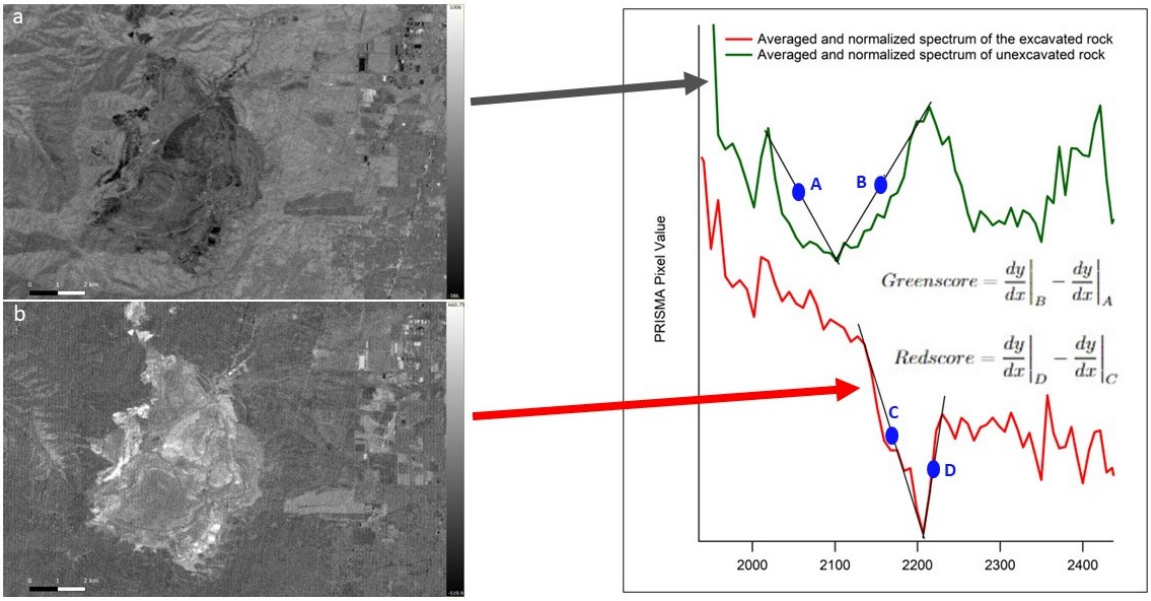

Figure 4.14: *(Left) (a) Score maps of the broad spectral feature around 2130 nm black pixels represent a low value while white pixels represent a high value, (b) Score maps of the vibrational line at 2200 nm.(Right) Spectral signature detail of where the Discrete Derivative Algorithm was calculated to make maps on the left side of the figure. These score maps are used to produce a RG image using the single spectral feature as first component (Redscore) and the broad combination of spectral feature as second component (greenscore).*

In figure 4.15 it is possible to see the final result of the mineral mapping calculated in this area: an RG image of the mine in comparison with the validation in the visible colors (provided by google hybrid satellite). As we can see from the figure, some areas that are barely distinguishable from the soil in the visible image are separated efficiently in the RG image, so there is no need to dig deeply the rock to detect minerals with hyperspectral imaging from satellite, it is enough that the rock is exposed to the air (while in the true-color imaging this could not change the visible color noticeably, and for this reason it could not be isolated and classified efficiently).

Figure 4.15: *(Left) A two-colors image produced using the score map of the feature at 2200 nm as component red and the score map of the feature at 2130 nm as the green component. (Right) RGB image of Google hybrid satellite. The cyan circle highlights an excavation area that is barely distinguishable from the surrounding terrain in the visible image, while it is correctly isolated and classified in the two-colors image. We further detect many more excavated areas that are not visible in the RGB image.*

To summarize the content of this work: a hyperspectral analysis of the excavated rock present in the largest open pit mine in the world (Bingham Copper Mine) is carried out. A spectroscopy classification map was performed for the vibrational feature of the excavated rock (object of interest) and the feature of the unexcavated rock (contrast signal in classification). After that, a two-colors image was created using the classification map of the excavated rock as the red component and the classification map of the unexcavated rock as the green component. The final result shows other areas outside the mine belonging to the excavated rock class and which are not easily distinguished in the PRISMA RGB image. This shows, apart from the effective recognition of excavated rock in the mine against the other pixels, that it is sufficient for the target to be exposed to the open air to be detectable by the satellite and distinguishable from unexcavated rock.

4.6 Mineral Mapping with laboratory ground truth (Elba Island)

As a final case study for what concerns the analysis of vibrational features in the SWIR from satellite images, we report a utilization of such hyperspectral data to highlight areas where the searched component is much more evident in an area of the same satellite image, far away from the place where the sample analyzed in the laboratory and used as ground truth was collected.
In this case, a fragment of the shores of Capobianco (Elba island, Italy) is collected as ground truth to be analyzed in laboratory. This sample of rhyolite is formed by two different components, as we can see in figure 4.16, a white matrix that surround black settings. The spectral signature of both components of the sample has been extracted and shown in figure 4.16.

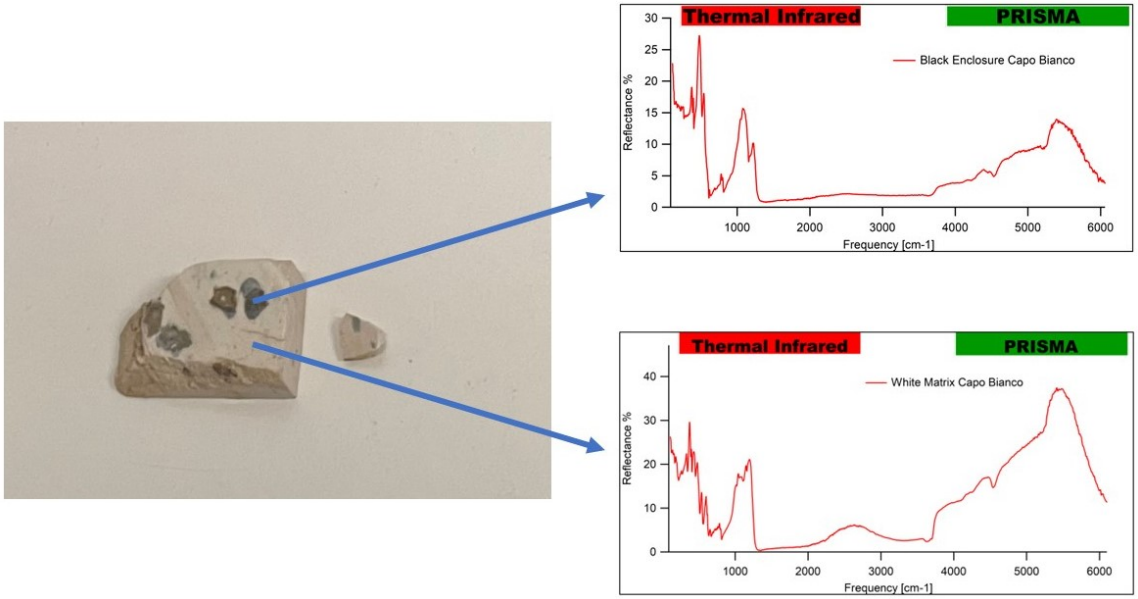

Figure 4.16: *The sample analyzed in laboratory in both its components, the green rectangle emphasizes the range in which PRISMA detector is sensitive, while the red rectangle emphasize the thermal infrared region, more interesting for vibrational features but out of the spectral satellite range of operability.*

From figure 4.16 it is possible to see that both components of the sample show a feature in the PRISMA spectral operative range at around 4540 $cm^{-1} = 2202\ nm$, for a better reading, this

feature is also highlighted n figure 4.17 together with a comparison with the PRISMA RGB image, and the analysis of the satellite pixel spectral signature of where the sample was taken.

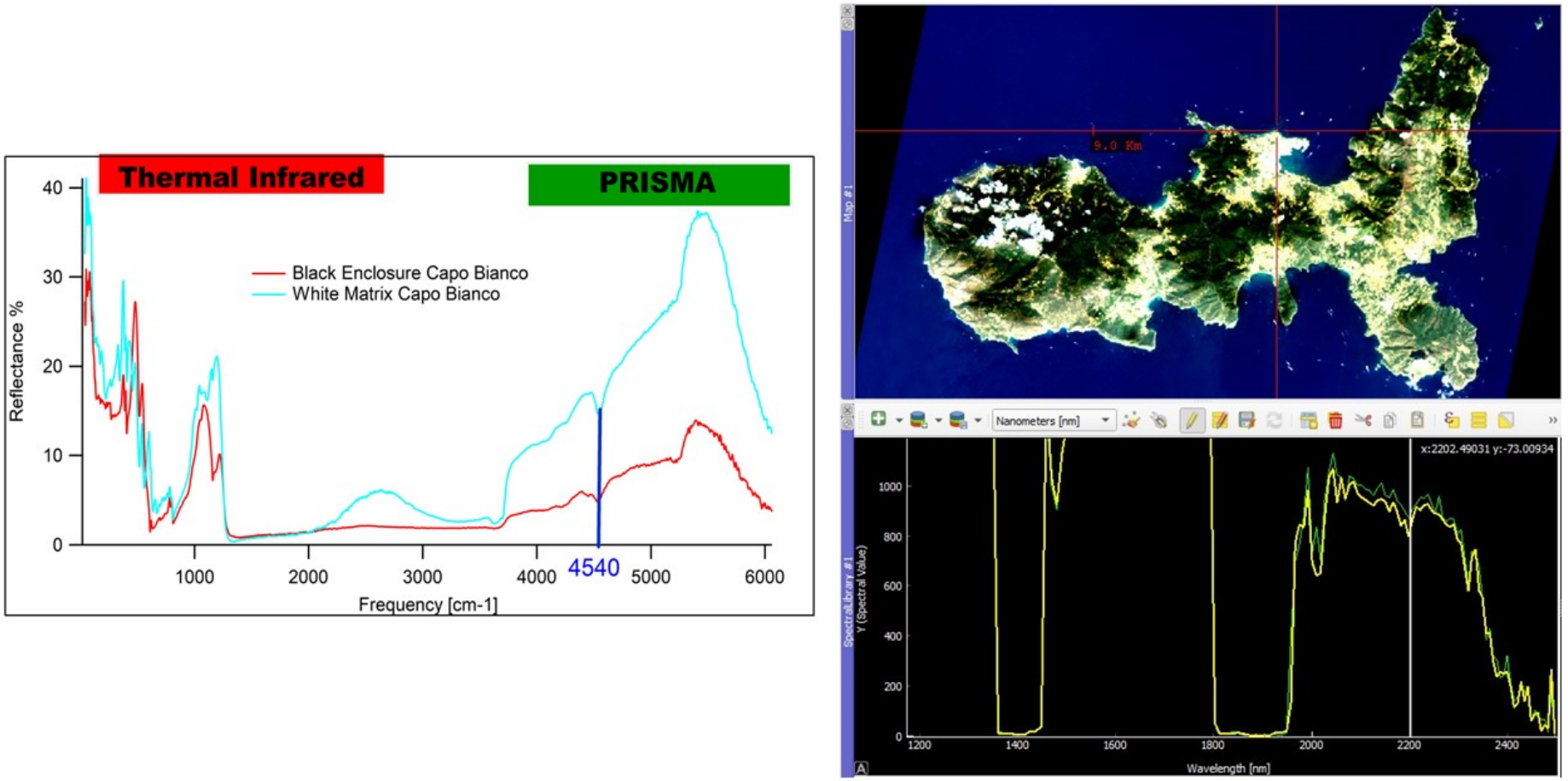

Figure 4.17: *(Left) The spectral signatures of figure 4.16 in one plot, the blue bar highlights the spectral feature of interest. (Right) The PRISMA RGB satellite image and two adjacent pixels of the place in which the sample analyzed in laboratory has been collected, the yellow solid curve indicates the pixel of the crosshair of the RGB image and a gray bar highlights the spectral feature of interest. As we can see, performing the conversion from* cm^{-1} *to nm, it is possible to notice that the feature highlighted in the laboratory is in the same position as the feature highlighted in the satellite data* $4540\ cm^{-1} = 2202\ nm$.

As the final result of this section, we perform the DDA on the spectral feature at 2202 nm of the satellite data. The result is shown in figure 4.18 where the analysis detected an area in which the feature is particularly intense. This location was validated with Google image and found to be an area of rock excavated by an Italian mining company (Eurit) providing a validation similar to what we have seen in the previous section with the excavated rock analysis.

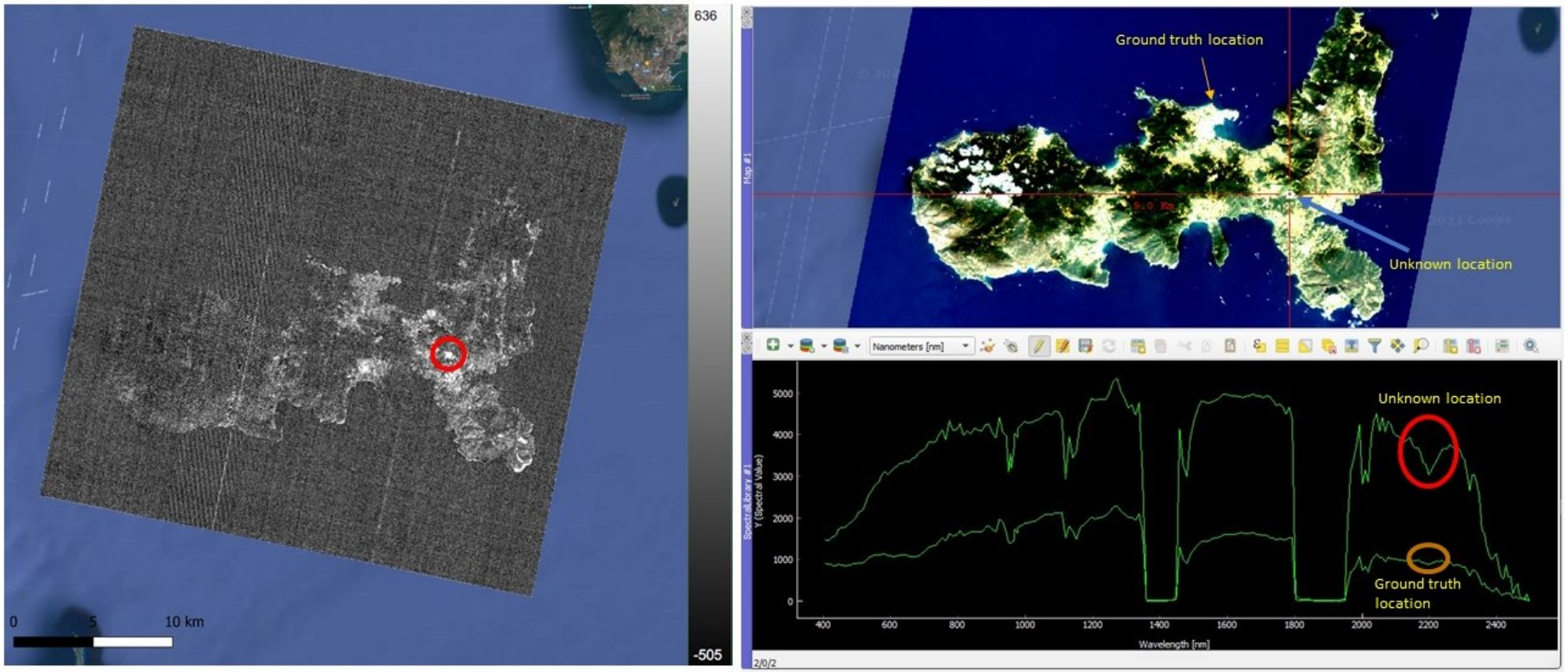

Figure 4.18: *(Left) The DDA on the spectral feature at 2202 nm in the satellite data projected on Google hybrid satellite image, white pixels indicate a high score while gray pixels a low score, the red circle emphasizes the area of anomaly detection. (Right) In the upper panel it is possible to see the RGB image of PRISMA acquisition with the geographical position of the ground truth location and the unknown location revealed by the DDA. In the bottom panel are shown the spectral signature of the pixel of the anomalous zone detection (green solid curve that has an overall high PRISMA pixel value and the spectral feature is emphasized by a red circle) and the spectral signature of the pixel from which the ground truth has been collected (green solid curve that has an overall lower PRISMA pixel value and the spectral feature is emphasized by an orange circle).*

To summarize what has been done in this part of the document: differently from the previous mineral mapping, and in addition to the satellite analysis, a part of ground truth analysis conducted in the laboratory is provided.
The fragment inserted and analyzed in the spectrometer of the laboratory was taken from a sample of rhyolite on the shores of Capobianco (Elba Island, Italy) and is made up of two distinct components from which the relative spectral signature has been extracted. Both components show a feature around 2202 nm and it was chosen to use this vibrational feature as a spectroscopic analysis of satellite images.
By making a comparison with the satellite images it can be seen that the same feature is clearly visible in the same pixel as where the sample was taken, from the classification obtained through the discrete derivative an area also emerged in which the line of the feature of interest it is particularly intense. The use of satellite data therefore made it possible to detect the mineral (mineral mapping) studied in the laboratory even in an area distant from the area where the sample was collected; this place was validated via Google Earth Images as a open pit mine.

4.7 Vegetation cover in Archeological Park

In this section we perform a direct comparison of multispectral and hyperspectral mapping of a very clear spectroscopic feature i.e. the absorption of chlorophyll in the red-to-infrared range (so-called Red Edge). This feature is employed in satellite EO to map the presence and the health of vegetation.
The vegetation state is typically obtained by change detection analysis of multi-spectral satellite images as a normalized difference vegetation index (NDVI) involving only two spectral channels. Here instead we utilize 10 channels from our PRISMA hyperspectral data across the chlorophyll absorption edge to show that the accuracy and information content can be drastically increased with respect to multispectral imaging. This comes at the cost of a lower spatial resolution.
The results show the benefits of these analyses in evaluating the state of landscape and in developing appropriate management projects.

Photomonitoring

In photomonitoring the operation that highlight changes between the two images is called Change Detection (CD), the first image is called "Master" while the second image is called "Slave".

The CD has been achieved through the IRIS software (see description in 3.3). IRIS performs in each image a Similarity Structure Index Measurement (SSIM) and, after that, makes a change detection of this quantity in a dynamic window between Master and Slave. SSIM is a technique of image analysis that consists in an index resulting from the combination of three contributions calculated on the whole image. These contributions are: the lighting contribution (l) given by equation (4.3), the contrast contribution (c) given by (4.4) and the texture (or structural component) contribution (s) given by (4.5), where the subscript x is referred to the Master image, the subscript y is referred to the Slave image, μ is the average, C_1 is the offset of l, σ is the standard deviation, C_2 is the offset of c, σ_{xy} the cross-covariance between Master and Slave and C_3 the offset of s.

$$l(x,y) = \frac{2\mu_x\mu_y + C_1}{\mu_x^2\mu_y^2 + C_1} \tag{4.3}$$

$$c(x,y) = \frac{2\sigma_x\sigma_y + C_2}{\sigma_x^2\sigma_y^2 + C_2} \tag{4.4}$$

$$s(x,y) = \frac{\sigma_{xy} + C_3}{\sigma_x\sigma_y + C_3} \tag{4.5}$$

The average μ_i, the standard deviation σ_i and the cross-covariance σ_{ij} are defined as

$$\mu_i = \frac{\sum_i I_i}{N_i} \tag{4.6}$$

$$\sigma_i = \frac{\sum_i (I_i - \mu_i)^2}{N_i - 1} \tag{4.7}$$

$$\sigma_{ij} = \frac{\sum_i (I_i - \mu_i) \sum_j (I_j - \mu_j)}{N_i - 1} \tag{4.8}$$

where I_i is the intensity of each pixel contained in the i-th window, N_i the total number of pixels contained in this area.

Combining the three contributions, we can define the SSIM between the x-Master and y-Slave images as

$$SSIM(x,y) = l(x,y)^\alpha + c(x,y)^\beta + s(x,y)^\gamma \tag{4.9}$$

where α, β and γ are coefficients used to weight each contribution.

Spectral signature of vegetation

Vegetation is composed of leaves that are characterized by carotenoids and pigments. These are responsible for the absorption and reflection in various range of energies (from the ultraviolet region to the short wavelength infrared region).
Limited to this project, we are interested in the pigments that absorbs in red and in near infrared range. Two different ways of monitoring these absorptions are used and compared each other to distinguish vegetation presence in the image. These methods are: i) the normalized difference vegetation index (NDVI [46]) given by the normalized difference between NIR and Red channel of the satellite (eq 4.10) for the multispectral data (from the multispectral satellite Sentinel 2 [47]) and ii) a personally developed Red Edge Score map that assigns to each pixel of the image a number that measures the slope of its spectral signature in the red edge range (using the PRISMA hyperspectral data) given by the equation 4.11.

$$NDVI = \frac{NIR - Red}{NIR + Red} \tag{4.10}$$

$$RE = \sum_{i=(M-4)}^{M-1} \frac{Ch_M - Ch_i}{M - i} + \sum_{j=M+1}^{M+4} \frac{Ch_j - Ch_M}{j - M} \tag{4.11}$$

Where Ch_M is the channel number 37 of the PRISMA satellite, centered at 713 nm and each channel is centered at 9 nm of resolution from each other.

Even if the Hyperspectral data have a lower spatial resolution (due to the greater spectral sampling) compared to multispectral data, they are able to trace more precisely the presence of vegetation, which are responsible for their characteristic reflectivity in the spectral zone of the red edge, allowing better quantitative and not only qualitative monitoring of vegetation areas, becoming a very effective tool in identifying and characterizing weed vegetation, which is the most widespread cause of damage of monumental heritage [48] - [49].

The study area (shown in Figure 4.19) is a cultural and urban context of great importance, the result of complex interactions between man and the natural environment (Ager Romanus).

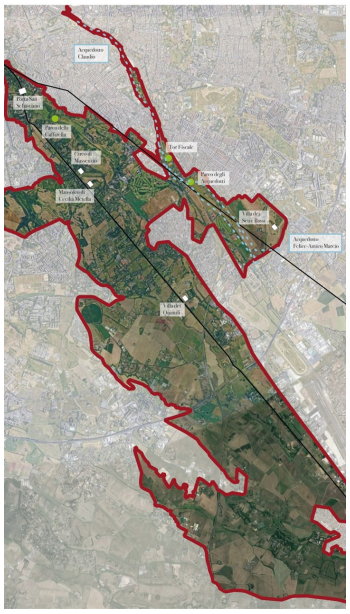

Figure 4.19: *Map of Appia Antica Regional Park with main locations, archaeological sites and roman streets.*

Figures 4.20 and 4.21 shown rasters of master and slave of Sentinel 2 and PRISMA rearranged in RGB channels (channel 3,2 and 1 for Sentinel 2 and channel 33, 23 and 12 for PRISMA satellite). In the tables 4.1 and 4.2 it is possible to see the dates of acquisition of the satellite images.

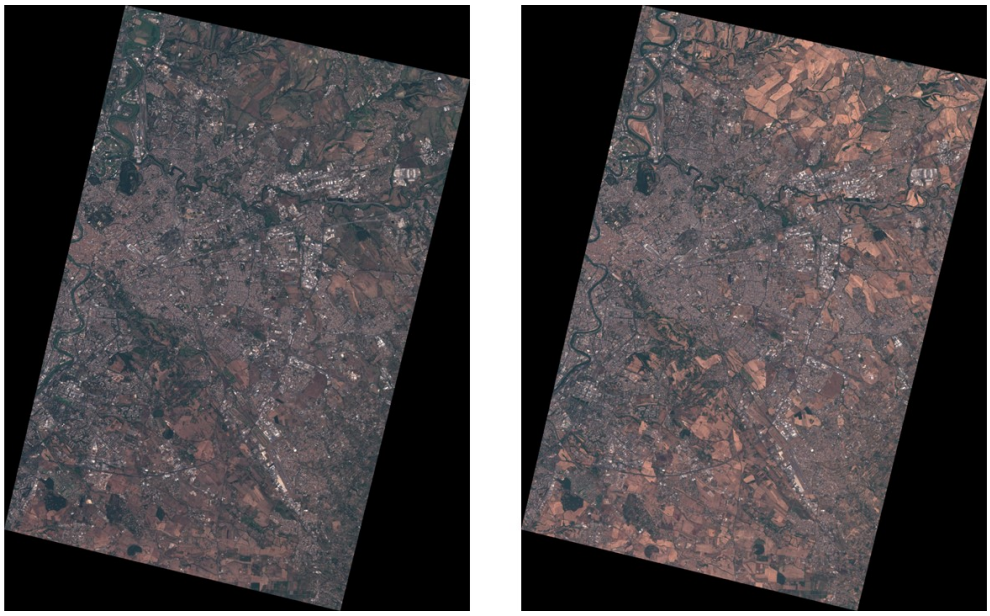

Figure 4.20: *Master (left) and Slave (right) Sentinel 2 images acquired on August* 18^{th}*, 2019 and July*19^{th}*, 2022, respectively.*

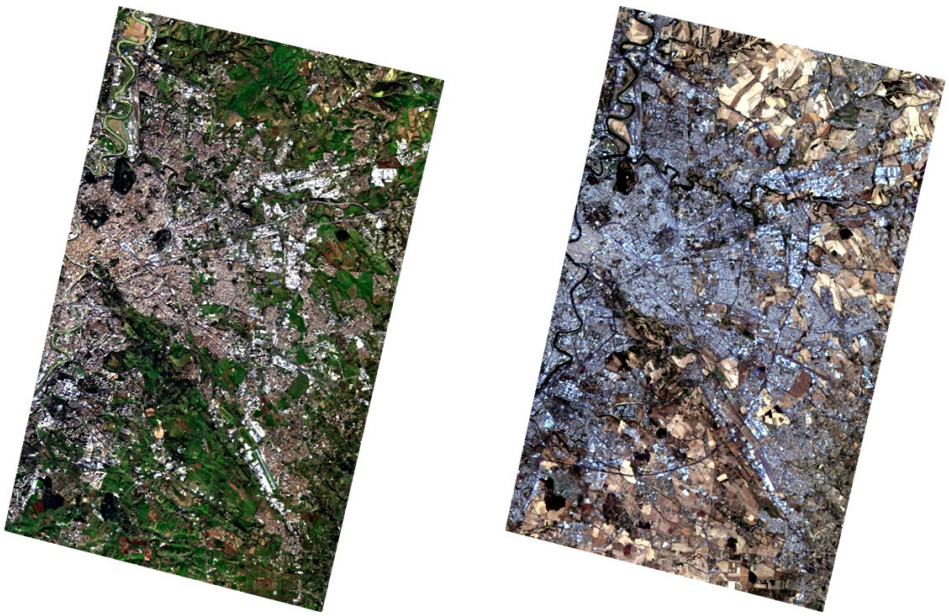

Figure 4.21: *Master (left) and Slave (right) PRISMA images acquired on August* 29^{th}*, 2019 and July*2^{nd}*, 2022, respectively.*

Table 4.1 shows data acquisition of master and slave images of Sentinel 2 with their NDVI score of pixel showed in fig 4.27 while table 4.2 shows the data acquisition of master and slave images of PRISMA satellite with the Red Edge Score of the same pixel in each acquisition.

Sentinel 2	Acquisition time	NDVI
Master	2019-08-18	0.5
Slave	2022-07-19	0.3

Table 4.1: *Sentinel 2 Data and NDVI.*

PRISMA	Acquisition time	Red Edge Slope Score
Master	2019-08-29	4479
Slave	2022-07-02	835

Table 4.2: *PRISMA Data and Red Edge Score.*

Fig. 4.22 shows the Normalized Difference Vegetation Index of master and slave of Fig. 4.20. These maps are used as input in the Change Detection performed by the IRIS software that is exposed in figure 4.23

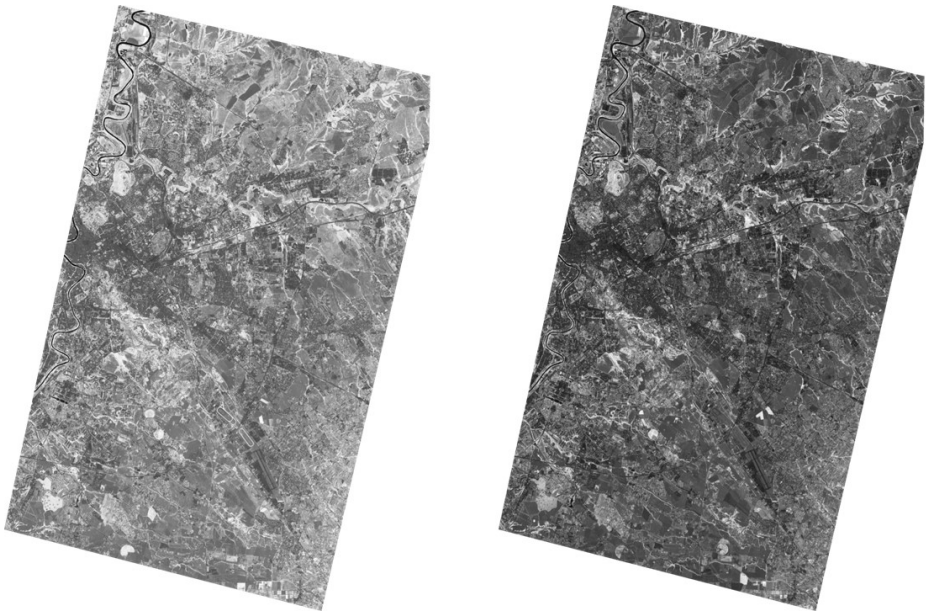

Figure 4.22: *a) NDVI score map of the master image of Sentinel 2. b) NDVI score map of the slave image of Sentinel 2.*

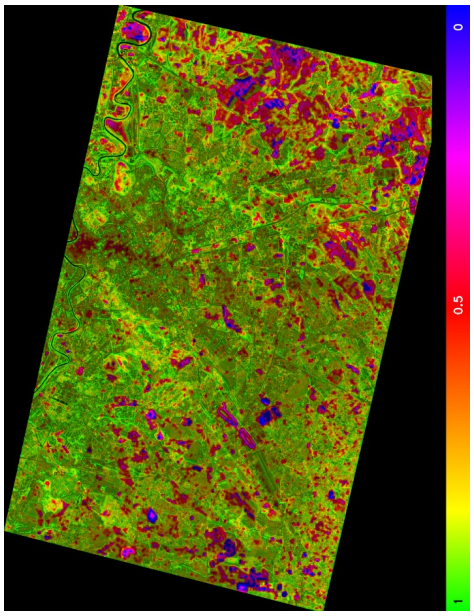

Figure 4.23: *Change detection performed by IRIS on the NDVI map score of years 2019 and 2022.*

Fig. 4.24 shows the Red Edge Slope score of master and slave of Fig. 4.21. These maps are used as input in the Change Detection performed by the IRIS software that is exposed in figure 4.25

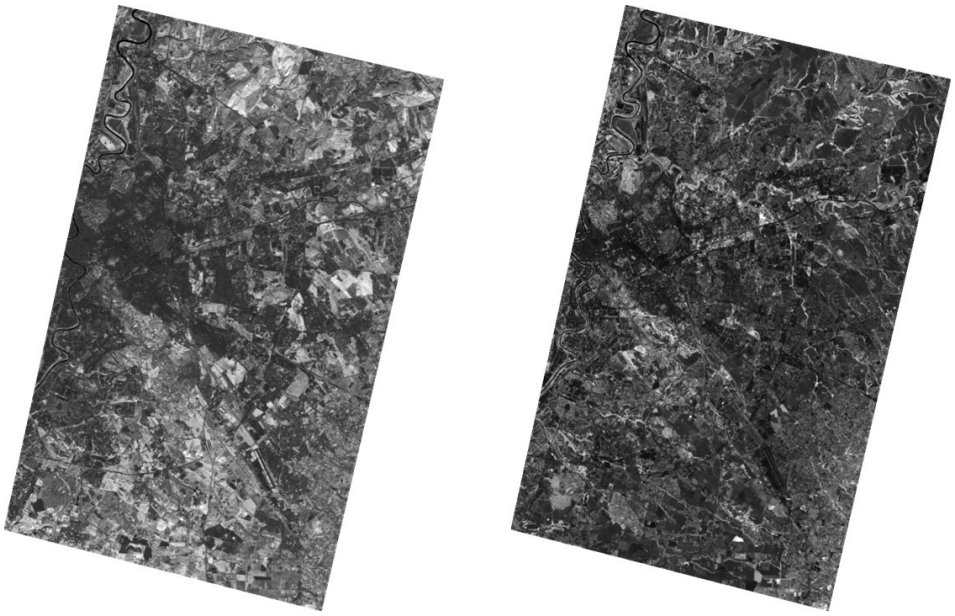

Figure 4.24: *Rasters of PRISMA in which Red Edge Score is calculated: master is on the left and slave is on the right.*

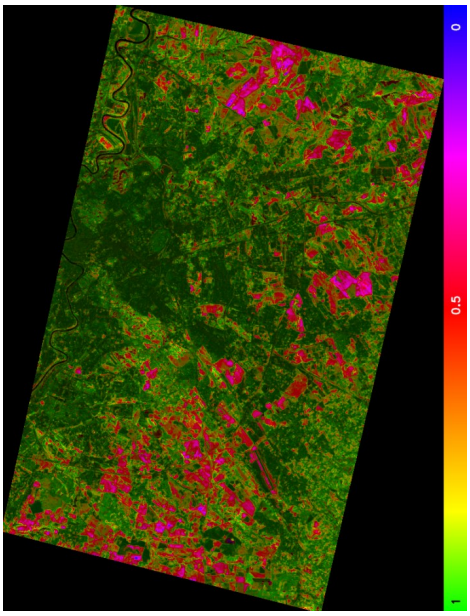

Figure 4.25: *Change detection performed by IRIS on the Red Edge Score map of years 2019 and 2022. As we can see, at a first comparison with image 4.23 the results are in agreement with each other.*

The red edge slope algorithm is able to provide a further detail of the state of health of the vegetation by studying the pigments of the leaves. Furthermore, it can detect changes that are not visible in the NDVI classification. This is because the NDVI algorithm is not able to trace these changes with only two bands centered in the spectral range of interest (even if they have a higher geometric resolution, as we can see from figure 4.26).
Using each band of this range, it is possible to evaluate the presence of vegetation in a more detailed way than with the NDVI. This is due to the fact that with only two points it is difficult to measure the red edge slope considering only the initial and the final values that characterize vegetation in a pixel. Instead, using a greater number of channels in this spectral range, it is possible to accomplish mathematical tools and calculations that evaluate the slope of the spectral feature in a broader scale.
As validation, we used the database of Google Earth. In Fig. 4.27 it is possible to view how vegetation cover is strongly reduced in the slave image. The white frame is a pixel of the PRISMA satellite in which the CD of the red edge slope indicates an important change.

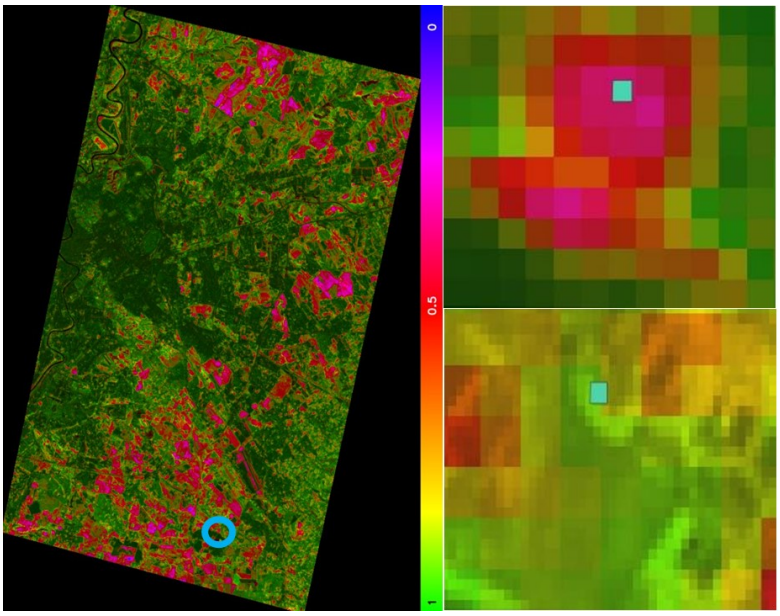

Figure 4.26: *A comparison between a zone of NDVI and Red Edge Score map, the cyan pixel identifies a pixel of PRISMA in which the validation in fig. 4.27 and the spectral signature in fig. 4.28 is calculated. (Left panel) the red edge score map of fig. 4.25, the cyan circle indicates the zone in which is performed the zoom in of middle and right panel of this figure. (Top right panel) a zoom in of the Red Edge Score map inside the cyan circle. (Bottom right panel) a zoom of the NDVI score map inside the cyan circle.*

Figure 4.27: *Google Earth images of 2019 (left) and 2022 (right) used as validation of this work. The framed area is the PRISMA pixel (white square) represented as the cyan pixel of fig. 4.26, in which the spectral signatures were calculated in fig. 4.28. As can be seen from the areas circled in red, in 2022 there are much fewer areas of vegetation than in 2019.*

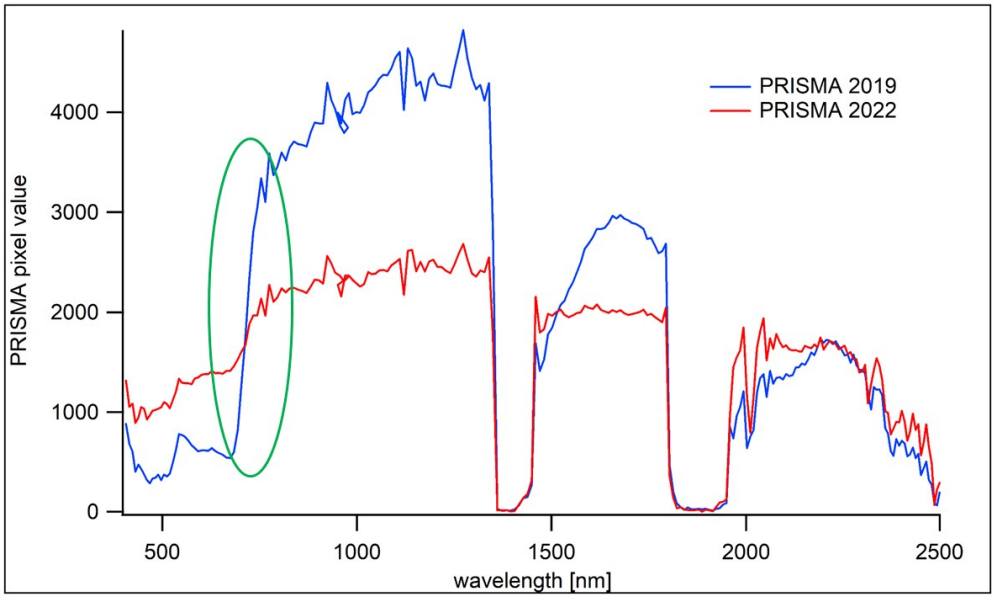

Figure 4.28: *Spectral signatures of the pixel present in Fig. 4.27: the signature of 2019 is dominated by vegetation due to the steepness of the red edge section, while instead that of 2022 is closer to the behavior of soils without vegetation (low steepness of the section red edge).*

As we can see from the tables 4.1-4.2, both NDVI and Red Edge Score note that vegetation cover decreases from master to slave. From the fact that the only possible values of NDVI are included in the range from -1 to 1 the algorithm is unable to detect little change of vegetation compared to the more accurate algorithm of Red Edge Score that is not limited by this numerical range. In Fig. 4.27 in fact the value of NDVI of master is 0.5 and decrease to 0.3 while the value of Red Edge Score of master image is 4479 and in the slave decreases to 835: this is the main reason that allows the change detection on the Red Edge Score to emphasize areas which are not evident in the change detection of the NDVI maps.
In Fig.4.28 the spectral signature of the pixel is very different between Master and Slave (and consequently the slope of the Slave pixel is closer to the typical behavior of soil in the red edge, as the cover vegetation is reduced).

In conclusion, the use of the Red Edge Score through hyperspectral data offers significant advantages compared to the use of NDVI. The primary benefit lies in the increased amount of vegetation information, as the Red Edge Score covers a much broader range of values compared to the limited range of NDVI (-1 to 1). This means that the Red Edge Score can provide information on vegetation within a range extending from positive values, even in the absence of vegetation, to infinity. This capability stems from its effectiveness in detecting vegetation reflectance within this spectral band. However, there is a noticeable drawback in utilizing the Red Edge Score: it results in images with lower geometric resolution compared to the multispectral satellite data. This limitation can be problematic if the primary objective is not only to analyze vegetation presence, but also to precisely assess the geometric extent of vegetation cover within a specific area and monitor changes over time.

Despite these disparities, it is feasible to merge data from both methods to obtain detailed images from both geometric (vegetation extent) and spectral (vegetation status) perspectives. This integration can represent a significant outcome of the study, facilitating a deeper understanding of vegetation conditions. Furthermore, it may be possible to establish parameters and thresholds based on the Red Edge slope that enable the classification of vegetation as healthy or unhealthy [50], thus contributing to effective monitoring of cultural heritage landscapes. If refined further, this approach could become a valuable tool for quantitative monitoring of vegetation health, proving highly effective in identifying and characterizing invasive vegetation, a prevalent cause of degradation to cultural heritage.

To conclude this part of the work: a comparison between hyperspectral imaging and multispectral imaging in the analysis of the chlorophyll absorption in the red-to-infrared range (red edge) is provided. Not only the acquisitions but also the different data processing methodologies are compared. In particular, for hyperspectral imaging the slope of the red edge is calculated through the discrete derivative calculation on the 8 characteristic bands of the signal, while for the multispectral imaging we used the Normalized Difference Vegetation Index (NDVI) which is nothing more than the difference of the two channels located at the beginning and the end of the red edge slope, normalized with their difference. A software of change detections calculates, through the Structure Similarity Index Measure (SSIM), the difference between a Red Edge Score map of 2019 and 2022 for the hyperspectral imaging and between a NDVI score map of the same period for the multispectral imaging. These two change detections are compared and it is highlighted that, in addition to being in good agreement with each other, the CD on the Red Edge Score map identified an area that had not been recognized by the CD on the NDVI. This result was validated using the catalog Google Earth images in the same period of satellite data acquisition.

Conclusion

This PhD dissertation is based on the concept of applying solid-state physics to satellite imagery as it relates to Earth Observations. This was made possible by the Italian Space Agency (ASI) PRISMA satellite, which provides satellite imagery with 30 m geometric resolution on the ground and continuous acquisition from 400 nm to 2500 nm with 239 bands (with a spectral resolution around 9 nm between the center of one band and the other).
The novelty of this work is precisely the investigation of the possibilities of spectroscopic measurements carried out by a hyperspectral satellite in the face of the various technological difficulties due to the lack of control over the source (sunlight), over the targets (the pixels of the satellite image as they appear in nature) and over the environment (presence of atmosphere between source and target and detector). The technical challenges in trying to perform infrared spectroscopy from a satellite can be summarized mainly in three issues:

- The semiconductor detector material: because vibrational spectroscopy has to be performed in the SWIR region of the electromagnetic spectrum where silicon is transparent, one cannot use silicon photodetector arrays such as CCD and CMOS, but discrete photodiode arrays (PDA) consisting of HgCdTe bound to a silicon circuit have to be employed instead. The use of PDA instead CCD or CMOS greatly affects the signal-to-noise ratio of the spectral lines acquired in satellite images.

- Sunlight and Atmosphere: Unlike in the laboratory, where one can work in a vacuum and use a suitable hot blackbody source, in satellite imaging one has no control over the source (sunlight) or the atmosphere between the sun and the target, and between the target and the detector. The atmosphere absorbs heavily at certain SWIR wavelengths (for example at 1480 nm and 2002 nm), completely masking the absorption of the target, and it is also opaque to radiation in the 1361 - 1450 nm range and 1803 - 1950 nm, thus preventing light from reaching the detector in these spectral ranges.

- Combination bands and Overtones: the detector of the PRISMA satellite stops at 2500 nanometers, where it reaches the noise floor, therefore it is unable to detect the fundamental vibrations of minerals that reside in the LWIR ($\lambda\, 8\mu m$), which have a much higher reflectance contrast than the combination bands and overtones that appear in the SWIR. In addition to a lower reflectance contrast, the detection of combination bands alone also sets a limit to the specificity of SWIR spectroscopy (it is possible to mistake spectral signatures that belong to different materials if one is not able to measure the fundamental vibrations in the LWIR) and to the list of possible minerals that can be analyzed by satellite (not every mineral presents strong overtones or combination bands that

promote spectral features from LWIR to SWIR).

In this work, we have tried six different cases of study with moderate success:

- Moraines / Glaciers (Gran Paradiso): A comparison between mineral mapping in satellite images obtained with spectroscopic and multispectral methodology is provided. A discrete-derivative algorithm has been developed in this PhD work to obtain the intensity of spectral features in a GIS environment. This analysis, due to the different ice coverage between the lithological chart and the satellite data, also represents a valid result in the field of climate change (the analysis could be repeated every year).
In the study of moraines and glaciers, it can be noted that hyperspectral analysis, compared to multispectral analysis, has improved the classification of the satellite image by exploiting the vibrational spectral characteristic of the specific mineral in the SWIR. This made the recognition of glacial moraine pixels distinguishable and not unstable inside the classification map. Furthermore, an additional feature is obtained: snow or ice pixels, whose reflectivity would be zero in the SWIR and therefore would not be identifiable in a multispectral procedure, are instead perfectly identifiable as pixels with very low reflectance in our discrete derivative algorithm.
The potential applications of this part of the work are glaciology studies and variations in the surface actually covered by glaciers from month to month depending on the passages of the hyperspectral satellites that will be made available with future missions. In fact, for PRISMA it is essential to note that the rock has recently been exposed to atmospheric agents ("weathering" that can completely erase the vibrational lines) and is also lacking of significant vegetation and soil. For this reason this application can be defined as "moraine mapping".
In a more general way, one could think of exploiting our algorithm for a more detailed and accurate analysis of the lithology of vast mountainous areas compared to the multispectral analysis techniques used so far [51], in which the presence of vegetation it is relatively sparse and there are areas of ice/snow due to the altitude.

- Silicates under vegetation (Vulcano and Lipari islands): An analysis of the hyperspectral data was conducted in order to obtain a qualitative analysis of the extension of the areas covered by volcanic sand, here identified spectrally as the silicate species called rhyolite. This study has been performed in an environment such as volcanic islands in which (unlike of the previous case of the moraines study) there was a poor but non-zero vegetative component.
In this part of the work, we attempted to weigh the quantitative data of the presence of rhyolite (given by the intensity of the silicate spectral line) with the data of the vegetative presence (given by the slope of the spectral signature in the "red edge" area).
The future application would be that of measuring the areas covered by ash or volcanic sand in the presence of poor vegetation, which can also be quantified in terms of covered area, even at the subpixel level. It provided mostly satisfactory results, identifying at least one area that is not easily detectable using the only silicate map and which is absent in the vegetation map, giving rise to the assumption that the area in question may host silicates in which a vegetative component is partially present.

This work leads to the path of development of mineral identification algorithms far more complex than the one created in this work. Subsequently, these algorithms will hopefully be able to quantify the area covered by the minerals exposed in a satellite image even if a vegetative component is simultaneously present that disturbs the result. Clearly, with this technique, the satellite hyperspectral imaging will not become a spectroscopic measurement capable of penetrating vegetation (which is impossible), but it will increase the range of areas in which it will be possible to effectively perform mineral mapping in a satellite image.

- Monuments made of marble (Rome) with Laboratory Ground Truth: Using the analysis of a travertine sample in laboratory as ground truth, we calculated the absolute reflectance of the mineral from the hyperspectral satellite data, exploiting normalization and averaging techniques on the data collected by PRISMA in order to emphasize the characteristic absorption line of the third overtone of calcium carbonate ($3\nu\ CaCO_3 = 2340\ nm$).
This work is the first to compare hyperspectral satellite data, obtained on an architectural building made predominantly with one material, with the spectral data obtained in the laboratory (ground truth) on a sample made of exactly the same material (Botticino marble or travertine). Furthermore, the need to normalize the hyperspectral data similarly to the laboratory procedure was demonstrated for a highly reflective surface contained in the same raster. This result is qualitatively different from the mineral mapping of natural terrains of previous works, in which the ground truth is necessarily taken from samples (existing in spectroscopic databases available online) similar but not necessarily identical to those of the hyperspectral data.
The possible applications of Botticino marble mapping find their place in the monitoring of architectural assets located in remote areas, in order to analyze their vegetative cover or chemical variation following atmospheric events and weathering.

- Open Pit Mine, Detection of excavated areas (Bingham Copper Mine): A two-color spectroscopic map (map of excavated/unexcavated rock signals based on two different spectral features in the SWIR) is provided. In addition to the mine that is at the center of the acquisition, the two-color SWIR image shows also areas of the excavated rocks outside the mine area, which were not detected in the standard true-color images in the visible.
We created a contrast capable of highlighting the vibrational feature that has to be classified (areas subjected to excavation) compared to the vibrational feature of the surrounding environment (different mineral that constitutes the soil not subjected to excavation). This demonstrates that ground motion can be effectively visualized in the hyperspectral map even if it is not immediately detectable in a true-color map.
This contribution highlights the fact that even if hyperspectral analysis is not penetrative, it is sufficient for the mineral to be analyzed to be exposed to the open air to make an effective satellite classification.

- Mineral Mapping (Elba island) with laboratory ground truth: We perform the spectroscopic map of rhyolite using the spectral signature of a pixel, from which a physical sample was collected, brought to the lab and measured to be used as ground truth. The result shows good agreement between laboratory and satellite data and provide also a result of anomaly detection with the spec-

troscopic map that emphasize a quarry in which the spectral feature is particularly intense.
This further application of satellite mineral mapping shows its ability to identify with high certainty even small regions of anomalous ground movement over a relatively large territory (one pixel signal, or an area of $30 \times 30\ m^2$, over a footprint of 900 square km). We have also provided further evidence on a natural material that the ground truth are in good agreement with the measurements carried out by satellite.

- Vegetation cover in archeological parks (Rome): we made a comparison of the imaging and methodology between multispectral and hyperspectral satellites in the analysis of a very clear spectroscopic feature in the red-to-infrared range: the absorption of chlorophyll (red edge). A software of change-detection developed by NHAZCA srl (IRIS) elaborates the difference between the two techniques and in addition to proving a good agreement of the final results of the two modalities, it also highlights how the vegetation description is more effective using the spectroscopic analysis of hyperspectral data rather than the multispectral data, even if at the cost of a lower geometric resolution.
In this example we have left the specific scope of this thesis (the vibrational analysis of SWIR spectral characteristics), to address a topic of much broader interest: the detection of vegetative cover by carrying out a comparison between hyperspectral data and multispectral data (with their characteristic analysis algorithms, red edge score for hyperspectral data and Normalized Difference Vegetation Index (NDVI) for multispectral data).
For the hyperspectral index we developed, we achieve much higher sensitivity and a higher dynamic range than the NDVI used for multispectral data. In particular, we have applied this method of mapping vegetative cover to the preservation and monitoring of green areas adjacent to cultural heritage. We also addressed the temporal evolution of hyperspectral data (time series), which represents a fundamental step for expanding hyperspectral analysis to environmental monitoring. The application of this analysis over time could be further improved thanks to the hyperspectral missions following PRISMA (such as, for example, EnMAP and PRISMA2G) which will increase the revisit time of the area to be monitored.

In all the cases outlined above we can add that the availability of hyperspectral data at higher spatial resolution (for example the possibility for PRISMA2G to create mosaics at both high spatial and spectral resolution) will allow a more effective data fusion with the other satellite data available in the scope of geomonitoring.

Appendix A

Thermal Infrared Imaging of a Landslide (Poggiobaldi)

This section reports a published article [52] in which new methods are presented for physical interpretation and mathematical treatment of the contrast observed in the thermal images of the rocky slope of the Poggio Baldi landslide (Italy), which is part of a natural laboratory.
The part of Image Analysis was written in collaboration with the Department of Basic Applied Engineering Sciences (SBAI) (prof Vittoria Bruni and Domenico Vitulano).
The article (that is listed in bibliography as [52]) is available at this link, https://www.mdpi.com/2072-4292/15/4/907.

Thermal images have been acquired with a high-performance camera at a distance around 500 meters, in a geometry where reflection is expected to dominate over thermal emission (as described for the geometry of the system in Figure A.1b and A.1d). The digital pixel intensities have therefore been considered as wavelength-integrated infrared spectral reflectance, irrespective of the temperature scale loaded into the camera software.
Sub-portions of the scarp producing lower signal have been identified by a multiscale image segmentation algorithm and overlaid on the visible image to provide an interpretation for the different thermal imaging contrast mechanisms that may be exploited for landslide monitoring in the future.

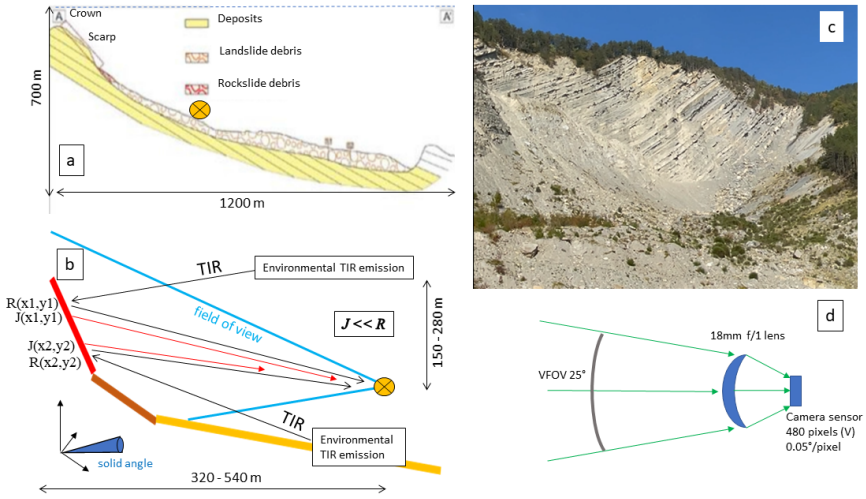

Figure A.1: *(a) Sectional view of the landslide and its constituents with the distance of the zone that is affected by the landslide and the height of the landslide. (b) Theoretical model of the reflection and the emission of the elements of the landslide projected in the pixel (x,y) of the LWIR camera detector with the distance and height of the detector respect the landslide. (c) Area corresponding to the field of view of the LWIR camera, cropped from a photograph in the visible range taken with the smartphone in Fig. A.2c. (d) Geometrical optics model of the vertical field of view of the LWIR camera.*

The landslide and its geological map are shown in Fig A.2. Using the high-performance LWIR camera in Fig A.2-b a monitoring distance of around 500 meters is demonstrated. The high-performance TIR camera objective has a very broad field of view of the upper scarp, comparable to that of a standard VIS/NIR imaging camera, which enables the overlap of real-time analyzed TIR images and archived VIS/NIR images.

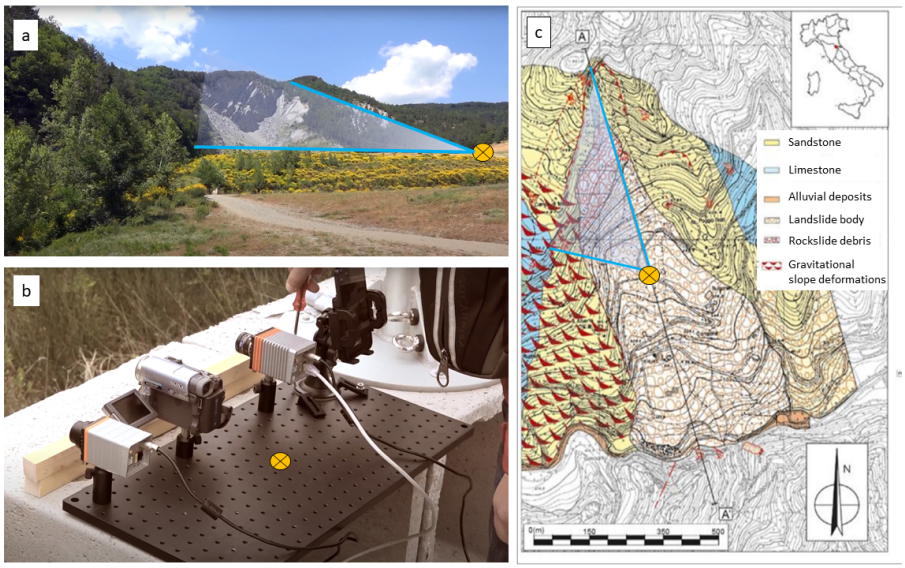

Figure A.2: *(a) Image of the landslide with its surrounding environment. (b) Optical system used for multi-wavelength imaging. From left to right: Thermal infrared (TIR) camera, low- resolution visible camera for image selection and alignment among sensors, short wavelength IR (SWIR) camera, and smartphone for high-resolution visible imaging. (c) Geological map of the Poggio Baldi landslide; [53] modified from [54]. In each panel a yellow black-crossed dot indicates the position of the optical system including the TIR camera.*

Landslide description

The Poggio Baldi landslide is one of the largest rock and debris phenomena in the Italian Apennines and a permanent natural monitoring site managed by the Department of Earth Sciences of the Sapienza University of Rome [54]. Advanced remote sensing tools are installed in order to monitor the activity of the main rocky scarp, which is often source of rockfalls, and the related debris talus at the toe [53].
The landslide has an estimated volume of about 4×10^6 m^3, and it is currently active in its upper scarp due to frequent rockfall events. The main rock slope, which is the target of this study, is a sub-vertical scarp with a rise of about 100 m and a width of 250 m and it is characterized by high-frequency rockfall processes. Since the first activation in 1914, despite the following steady state of the main landslide body, the newly formed vertical rock cliff has always been frequently affected by rockfalls. The instability is predisposed by geologic, geomorphological and structural factors, such as the alternation of arenaceous and clayey strata and the presence of several discontinuities. Moreover, considering the progressive erosion of the clay strata, which gradually increases the overhang of the arenaceous strata, rockfalls are mainly triggered by: (i) the breaking of the arenaceous mass due to shear strength surplus and, (ii) the intersection of a joint with the exposed surface of the cliff. The detached debris and blocks often find deposition surfaces over the underlying arenaceous strata. Over time, the volume of fallen material increases on the overhanging strata till the debris friction angle (39 degrees) is exceeded, with the consequent remobilisation. These conditioning factors, combined with each other, are the main cause of the widespread instability throughout the vertical rock cliff. As a matter of fact, estimates the general loss of volume from the vertical rock cliff to be in the range of 2.0 to 2.8 $\times 10^3$ m^3 per year.

Physical Model

For a given object with volume and surface orientation, the integrated spectral emittance $e(\lambda)$, displaying a material-specific dependence on the TIR wavelength in the $\lambda \approx 8 - 13\mu$m range, is defined as follows:

$$\epsilon = \frac{1}{\Delta\lambda} \int_{8\mu m}^{13\mu m} e(\lambda) d\lambda \tag{A.1}$$

where $\Delta\lambda$ is the spectral range of integration for TIR remote sensing and $e(\lambda)$ is the adimensional product of the absorption coefficient $\alpha(\lambda)$ and a penetration length scale of TIR radiation in the material, which is of the order of 1 μm for rocks and minerals. We approximate the spectral dependence of Planck's blackbody emission law at $T \sim 300$ K as almost wavelength-independent in the 8-13 μm range. This considerable conceptual simplification is justified because the Planck's law at $T = 300$ K peaks at around $\lambda = 10$ μm (about 30% of the total TIR emitted by a blackbody at $T = 300$ K lies in this relatively narrow wavelength range), but it should be noted that it would be straightforward to include the Planck's law in our model to increase its quantitative accuracy. In the case of a rocky scarp almost free of biomass, it is possible to obtain, from a TIR image, information on the different materials contained in the different pixels of the image (different rocks, sand, minerals, water, or a combination of these) not from their thermal properties (i.e. from the equilibrium temperature that they assume given their thermal capacitance and conductivity) but

from their optical properties (their different TIR emissivity and/or, as we shall see, reflectivity). This identification is especially accurate if one can assume temperature homogeneity across the TIR image:

$$J(x,y) = \epsilon(x,y) \cdot \sigma T^4(x,y) \approx \epsilon(x,y) \cdot \sigma T^4 \tag{A.2}$$

where the last approximation (homogeneous temperature) holds in the case of the present work, because the exposure of the scarp to sunlight is homogeneous and the thermal conductivity along the marly-arenaceous strata is expected to be high, thereby forcing a similar T for all portions of the scarp.

We estimate that, in the present case of a steep rocky scarp and with a TIR camera objective with broad field of view (fov), the reflected TIR power $R(x,y)$ can easily overcome the TIR power emitted by the element of the scarp itself $J(x,y)$. We can therefore write for the total TIR power $P(x,y)$ reaching each pixel of the camera:

$$P(x,y) = J(x,y) + R(x,y) \approx R(x,y) \tag{A.3}$$

where $R(x,y)$ is defined by another optical property of the materials contained in each element of the scarp corresponding to a pixel in the TIR image: the spectral reflectance $r(\lambda)$. The spectral reflectance is distinct from the spectral emittance $e(\lambda)$ but it can be derived from the same physical model of the optical constants, called the Lorentz oscillator model. In general, $R(x,y)$ can be calculated from the known $r(\lambda,x,y)$ of the materials in each pixel, from the solid angle fraction $\int d\Omega$, corresponding to the number of specular reflection paths connecting the environmental thermal sources to the reflecting surface and then to the TIR camera within its fov, and from the environmental temperature T_{env}, which is in this case the same for all pixels in the image.
For an ideal scarp with constant inclination across the inspection area, we can assume that the integration domain in $d\Omega$ is the same for all pixels corresponding to the scarp, and we can reduce the x,y dependence to $r(\lambda,x,y)$:

$$R(x,y) = \frac{1}{2\pi^2}\frac{1}{\Delta\lambda}\int_{fov} d\Omega \int_{8\mu m}^{13\mu m} r(\lambda,x,y)\cdot\sigma T_{env}^4 d\lambda. \tag{A.4}$$

and therefore the TIR image becomes a map of the optical properties of the materials forming the surface of the scarp.
In the present case, however, the overhanging arenaceous strata constitute sub-portions of the scarp with completely different orientation angle, therefore they will reflect less TIR radiation towards the camera if compared to steep sub-portions, as we shall see in figure A.4 and A.7. For each element of the scarp imaged by one pixel of the camera, one should therefore adjust the solid-angle integration domain $\Omega(x,y)$ quantifying the reduced number of specular reflection paths within the fov. In general, less reflected TIR power is expected from sub-portions of the scarp with anomalous inclination angle (less photons reach the detector), such as the overhanging strata of the present scarp.

In Fig. A.3, left panel, we show the spectral emittance $e(\lambda)$ and reflectance $r(\lambda)$ calculated

from the optical constants of argillaceous sandstone, which were obtained with a fit to the Lorentz oscillator model of the diffuse reflectance spectrum reported by the NASA-Ecostress spectral library (sample No. Ward63). One can see two prominent spectral peaks at 8.3 and 9.2 μm wavelength corresponding to two strong vibrational modes of the Si-O-H octahedral network of the silicate rock. A third smaller peak is seen at 12.5μm, related to vibrations involving the cation (as we can seen from section 2 Fe, Al and Mg are the most common cation in silicate rocks for what concerns this vibrational feature). The specific spectral shape of the reflectance of sandstone in Fig. A.3 will be considered in this work as the relevant spectral dependence for the calculation of TIR image contrast.

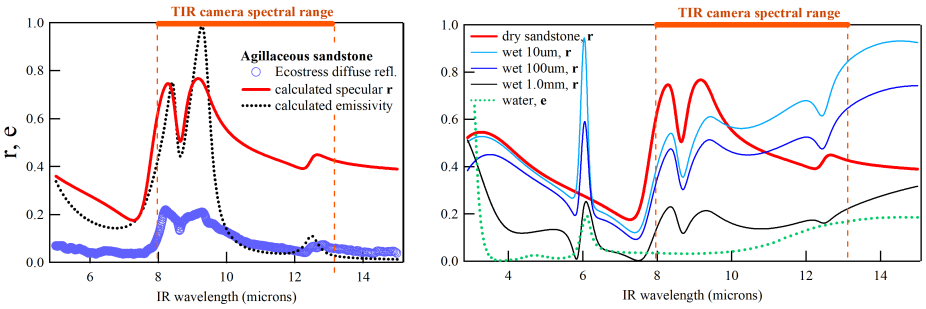

Figure A.3: *Left Panel. Blue circles: diffuse reflectance data (spectral signature) of the argillaceous sandstone (sample No. Ward63 from the ECOSTRESS Spectral Library); calculated specular reflectance (red curve) and emittance (black dotted curve) of the same argillaceous sandstone sample. The Lorentz oscillator model has been used to fit the data and to perform the calculations. Right Panel: calculated reflectance of dry argillaceous sandstone (red curve, same as left panel), with 10, 100 micrometers of water on top of the rock surface (light, dark cyan line) and with 1 mm of water on top (black line). The green dotted line is the emittance of liquid water (green dots).*

As we shall see below, in our images we have surprisingly observed different TIR signal levels from neighboring portions of the scarp featuring nominally identical mineral composition. In the case of overhanging arenaceous strata, this contrast can be tracked down to a different spatial orientation impacting on the total reflected TIR power towards the detector. In other cases where the different spatial orientation cannot be invoked, we hypothesize that the lower TIR signal may correspond to a thin layer of liquid water inhomogeneously covering the rocky surface. This hypothesis is also based on the geological history of the Poggio Baldi landslide (2010 event triggered by water pressure increase [53]). In other words, we propose that TIR imaging may be used to identify the scarp locations that are more wet, or more prone to water absorption and retention, hence possibly to (past or future) rockfall [55], [56]). To demonstrate this hypothesis, we have produced a multilayer optical model of the reflectance of an infinitely thick sandstone layer coated with a very thin water layer, which we show in Fig. A.3b. It is apparent that the presence of a water layer of 100 μm thickness or more, can sensibly decrease the observed spectral reflectance integrated in the 8-13 μm range. This peculiar spectral behavior derives from the complex interplay between the sandstone optical constants and the optical constants of liquid water. It can be understood in terms of a refractive index matching effect: the high reflectance of rocks in the TIR is due to the high value of the refractive index n (in this case, we calculate in the 8-13 μm range values of $n(\lambda)$ between 2.1 at $\lambda = 8.8$ μm and 8.3 at $\lambda = 9.5$ μm, with an average value of 4.5). The refractive index of water in the 8-13 μm range is $\sim$ 1.3, higher than that of air (1.0); therefore, a thin water layer on top

of the rock surface decreases the refractive-index difference (i.e. the electromagnetic wave velocity impedance mismatch) between the rock and the external space. It is crucial that water is weakly absorbing in the 8-13 μm range: for example, at $\lambda \simeq 6$ μm liquid water has a spectral emittance peak that would completely reverse the TIR imaging contrast (higher reflectance for rocks covered by a water layer), however this behavior cannot be observed with standard TIR cameras because it is outside the atmospheric transparency window 8-13 μm (and in fact the thermal camera is sensitive only in the same range).
Orange lines in Fig. A.3 identify the atmospheric transparency window, which defines the spectral range of integration $\Delta\lambda$.
Finally, one should notice that, in all cases where emissivity dominates over reflectivity in Eq. A.3, the effect of water layers is probably not observable, as the spectral emittance of water in the 8-13 μm range is negligible if compared to that of rocks (compare the dotted curve in Fig. A.3a with the dotted curve in Fig. A.3b).

Experimental Results

Thermal images have been acquired with a high-performance TIR camera (Gobi 640 by Xenics) with 640×480 pixels. The sensor is a microbolometer array made of amorphous silicon sensing elements, with pixel pitch of 17 μm, processed on a complementary metal – oxide semiconductor (CMOS [57]) readout integrated circuit (ROIC [58]) featuring an analog-to-digital converter (ADC) that provides fully digital images in raw intensity format, i.e. ADC counts per each pixel. The camera mounts a germanium lens-objective with focal length of 18 mm, and f/1 optics corresponding to a horizontal and vertical field of view full-angle of 33^o and 25^o respectively (see Fig. 2d). The spectral range of sensitivity of the microbolometer array is limited by a long-pass filter to TIR $\lambda > 8\mu$m and it is effectively limited to $\lambda < 13\mu$m by atmospheric absorption.
The data acquisition time is 11:38 am on the 27^{th} of October 2021, in clear sky conditions at the terrestrial coordinate of 43.910538° N, 11.807625° E. The ambient temperature value is of 14°C and the position of the sun at the time of image acquisition was of 30.23° of altitude and 156.84° of azimuth. The approximate azimuthal angle between this solar radiation direction and the scarp plane (which is oriented at 15° from the north-south direction, see Figure 1c) is then 40°. The distance of the camera from the landslide crown varies from $\sim$ 300m at the southern end to $\sim$ 540 m at the northern end (higher elevation point, 280 m above the camera). The lateral sizes of the elements of the scarp imaged by each pixel varies between 0.3 and 0.6 m, depending on view angles, distance and elevation. Due to the high elevation and short distance of the camera from the scarp, many specular reflection paths at the scarp surface exist, connecting the surrounding environment to the camera (Fig. 2b). A typical resulting image, acquired with a frame rate of 19 Hz (0.53 seconds per frame, suitable for real-time monitoring), is shown in Fig A.4. In the left panel, we show the image in a commonly used temperature color-scale that assigns a temperature value to each pixel using the equation of Stefan-Boltzmann. While the TIR image can certainly be utilized, e.g. to qualitatively detect structural features, this temperature scale is not meaningful in the present case because the reflected power R dominates over the emitted power J, see Eq. A.3. We will therefore not use further the temperature scale in this work. In the right panel we therefore

show the raw Analog to Digital Converter (ADC) values. As expected, the TIR signal from the sky is null and the vegetation reflects far less than rocks due to diffuse light scattering that takes place also at TIR wavelengths. Vegetation areas (approximately corresponding to the greenish pixels in the left panel) are identified by comparison with the visible image in Fig. A.1 c). The interesting portion of the image is the rocky scarp not covered by vegetation (approximately corresponding to the reddish pixels in the left panel). In the rocky scarp, the different sandstone and clay strata are apparent, as their real size is larger than the imaged pixel size of $0.3 - 0.6$ m depending on view angle. The foot of the scarp close to the lowest white dot is very evident in the TIR images but it is just the dividing line between the rocky scarp and its own debris. Beyond the "fast" TIR intensity modulation due to the strata, which can be rigorously canceled as we shall see in the next section, a much weaker modulation of the TIR signal intensity summed over larger sub-portions of the rocky scarp is observed. The sub-portions are difficult to see at naked eye, therefore we will resort to multiscale segmentation to highlight it, but we can anticipate that in some cases they will correspond to overhanging strata with surface orientation different from the rest of the scarp, and in other cases a contrast independent of the orientation of the strata has been observed. We note that the average surface orientation with respect to the sunlight direction is uniform across the scarp, resulting in similar solar irradiation levels.

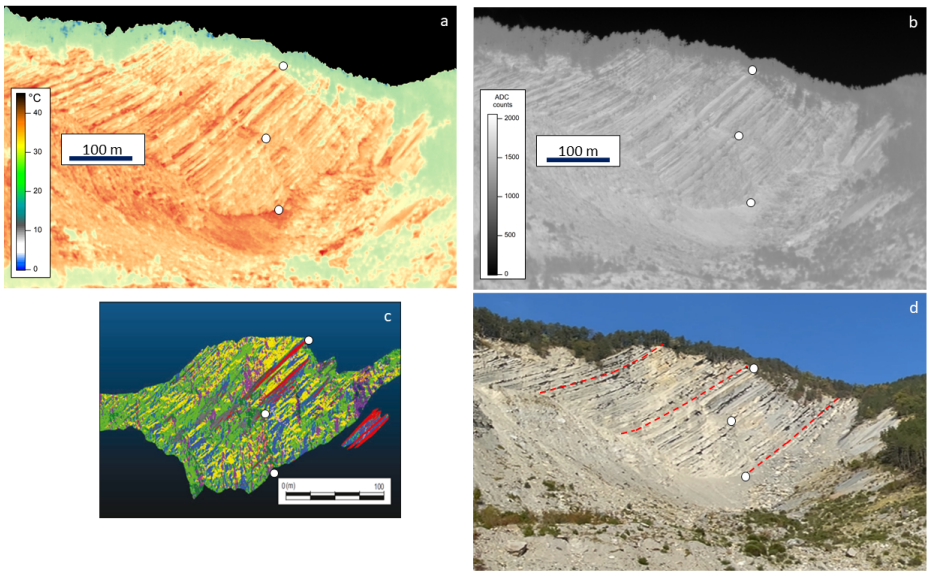

Figure A.4: *(a) Thermal image represented in the false-colour temperature scale loaded in the camera software. The sky pixels have low values and have been manually set to black. (b) Thermal image in gray scale, corresponding to the raw image data in analog-to-digital-converter (ADC) counts. Note the stacking fault in the middle of the scarp, almost perpendicular to the strata, which is very clearly visible in the TIR images (c): point-cloud image of the same rocky scarp, obtained by stroboscopic imaging with an unmanned aerial vehicle (reproduced from Ref. [59]): the different colors highlight the discontinuity systems enclosed within rock joint lines, which may be taken to correspond to different homogeneous rocky areas (e.g. the stripes in red color represent the sandstone overhangs mentioned in the paper text). The angle of observation is slightly different in the thermal/visible image and in panel c, therefore we added three reference points to all panels (white dots). (d): visible image of the scarp showing the three different members of the marly-arenaceous formation separated by dashed red lines, more details can be found in [60]*

.

Image Analysis

As a matter of fact, processing the TIR image resembles the problem of the detection of slightly visible regions in an image, that can be successfully solved by employing some concepts, as contrast sensitivity and multiscale filtering [61]. The former is the ability to distinguish an object (luminance) from its surrounding background; the latter corresponds to the ability in perceiving or disregarding details. It turns out that there are three main phases that characterize the proposed approach:

- *Spatial regularization.* A change of scale of the image under study oriented to eliminate a spurious single-pixel classification that makes human eye to be confused. This step can be further stressed using more than one scale where the resulting matrices are then multiplied each other (multiscale regularization).
The change of scale of the input image can be seen as simple application of the Multiresolution Analysis theory. The latter involves the formal definition of how producing different scales of a given function that are correlated each other by some mathematical properties [62]. This representation is oriented to highlight specific details of a given signal in agreement with the pioneering studies on multiresolution pyramids by Burt and Adelson [63] first and the formal construction of orthogonal wavelets then [64].
Coarsely speaking, a given function f at a resolution 2^{-j} can be seen as a (discrete) grid of samples where local function averages are considered — the size of the average domain is proportional to 2^j. It turns out that a multiresolution approximation of f is composed of different and embedded grids. Very often, this operation becomes more intuitive by considering each one of these grids (say that at resolution 2^{-j}) as the orthogonal projection on the space $V^j \subset L^2(R)$. The latter includes all possible approximations at the resolution 2^{-j}. Hence, starting from a given function f, its approximation f_j at resolution 2^{-j} is the projection on the space V^j constrained to minimize the following quantity: $||f - f_j||$. Usually, this operation can be achieved by convolving f with dilated and translated version of a scaling function Φ.
The Haar scaling function [62] has been used in this study. The Haar scaling function computes local averages of f with on a fixed window, different for each multiresolution level. Keeping in mind that in our study case $f \in \mathbf{R}^2$ as it is a 'thermal image' $I(x, y)$, we can consider $I(x, y)$ at a given resolution 2^{-j} i.e., $I_j(x, y)$. The desired resolution is the one at which local details (e.g. the arenaceous strata) are disregarded while contrast sensitivity for the wet region is enhanced, as shown in Fig. A.5-a.

- *False intensities distribution regularization.* A histogram equalization of the resulting image in order to make the image constrast 'uniform' to be better analyzed by human visual system.
To perform this step, two additional operations have been performed: histogram equalization and a suitable segmentation (that represents the next step). The former aims at emphasizing homogeneous regions, the latter aims at separating those regions. Their combined use resembles a non linear segmentation. Histogram equalization of an L levels (i.e., $\log_2(L)$ bits) image $I(x, y)$ consists

of defining a new image J having a flat histogram [65], i.e.

$$J = T(I), \tag{A.5}$$

where T is a proper transformation that depends on the discrete (L-levels) cumulative distribution function of I. A simple rescaling operation maps values back to the original range of values:

$$\bar{J} = J \cdot (\max\{I\} - \min\{I\}) + \min\{I\} = J \cdot (L-1). \tag{A.6}$$

and Fig. A.5-b shows the equalized low-resolution image.

- *Intensity multiple thresholding.* A suitable segmentation of the resulting image is then necessary to partition the resulting image in homogeneous regions characterized by the same physical properties.

This last step is based on scalar segmentation [65], whose objective is to reduce the set of possible image values, as shown in Fig. A.5-d. A segmentation function, or quantizer $Q(x)$, is:

$$Q : \mathbf{R} \to C \tag{A.7}$$

where $\mathbf{R}$ is the real axis while $C \equiv \{y_1, y_2, ..., y_N\} \in \mathbf{R}$ is the codebook, with $y_1 < y_2 < ... < y_N$ and $\Delta_k \equiv (y_{k-1}, y_k]$ the segmentation bins. C has finite cardinality, i.e. $|C| = N$. In the present study, a uniform and scalar quantizer has been considered. Hence, the range for image intensity value $[a, b]$ is split into K sub-intervals $\{(y_{k-1}, y_k]\}_{1 \leq k \leq K}$ having the same size and

$$\forall x \in (y_{k-1}, y_k], \qquad Q(x) = x_k \tag{A.8}$$

with $x_k \in (y_{k-1}, y_k]$ — x_k is usually set equal to the middle value of $(y_{k-1}, y_k]$. The choice of how many scale levels as well as how many segmentation bins to select must be adapted to each study case. Figure 5 represents the intermediate steps of the image segmentation analysis (regularization, equalization, quantization) from the raw data of the thermal image. These steps "simulate" image processing steps that are believed to happen in the human brain (not in the eye itself) to transform an image into useful information for decision-making. For the final image of the present work (Fig. A.7), we have employed the finer multiscale segmentation result shown in Fig. A.6. Image analysis can be refined in the future by fine tuning the number of scales to be used for image regularization, and the number of segmentation bins. Methods based on the minimum description length are particularly well suited for this purpose.

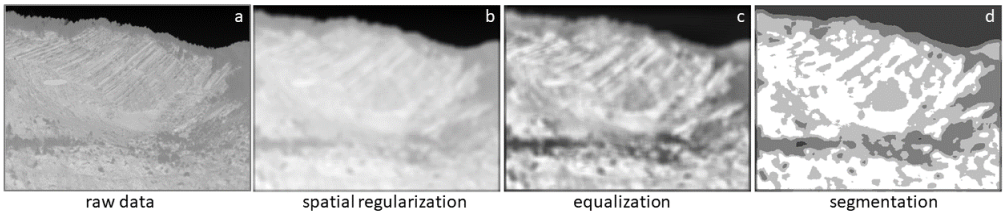

Figure A.5: *(a) raw TIR image data; (b) low-resolution version of panel a; (c) output of the histogram equalization, regions having homogeneous local luminance values are now emphasized; (d) segmented image using a choice of four bins.*

.

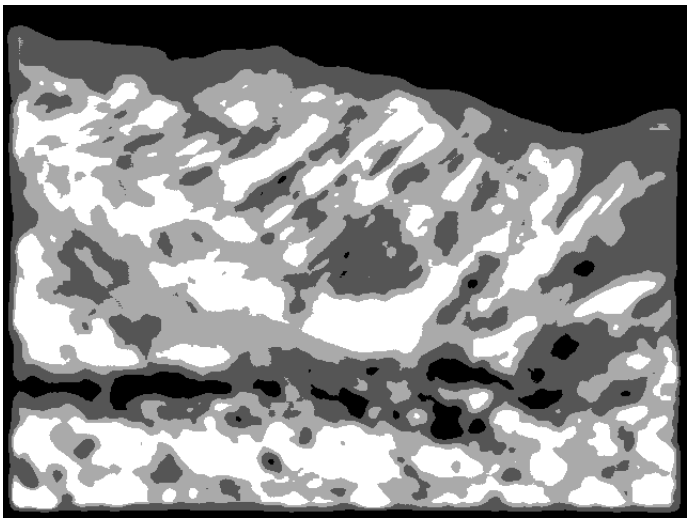

Figure A.6: *Output of the proposed image analysis procedure where four scales have been properly combined in the spatial regularization step, before applying histogram equalization. A more detailed segmentation is provided in this case.*

Interpretation of the results

The image in Fig. A.7 can be considered the final result of this section. The two lowest levels of the chosen multiscale segmentation are identified with vegetation areas (to be discarded) and monitoring target sub-portions of the scarp that produce an anomalously low TIR signal. The two highest levels are interpreted as normal scarp sub-portions not relevant for hazard monitoring purposes, and therefore they have been set as transparent layers in Fig. A.7. A baseline is defined within the output of the segmentation algorithm, which includes all pixels with uniform intensity value and spatial distribution so sparse that they cannot be identified as a single geological unit, and therefore as a specific hazard cause. For this reason the two highest segmentation levels have been made transparent because their TIR image provides no information, at least within our segmentation analysis.

The lowest segmentation level (dark blue zones in Fig. A.7a and A.7 b) identifies vegetation areas at the foot of the rocky scarp. Vegetation is assumed to reflect far less TIR intensity in the specular direction than the rocky scarp due to scattering from the "rough" surface constituted by leaves, branches etc.

The second-lowest segmentation level (purple zones in Fig. A.7a and A.7b) identifies sub-portions of the scarp that are relevant for hazard monitoring because their TIR signal is anomalously low. The first class of relevant areas are those with high humidity. According to our physical model, thin layers of liquid water (hundreds of μm thickness, compatible with local humidity of the rock surface) can decrease the TIR reflectance substantially. The valley marked with the number "1" in Fig. A.7 and the rocky areas under the vegetation are very likely to be more humid in the morning hours, indeed. The connection between humidity and rockfall hazard is yet to be established in full in this case, but it is likely considering the landslide history.

A second class of relevant areas obviously correspond to the overhanging arenaceous strata, one of them marked with number "2" in Fig. A.7 a. Following our physical model, reflectance is expected to dominate over emittance, unless the surface orientation angle of some sub-portions is different from the average scarp orientation. The orientation angle of these overhanging strata is certainly very different from the average scarp orientation. We expect therefore that the TIR power reflected by these sub-portions of the scarp would not reach the TIR camera but rather be reflected outside the field of view. This TIR contrast mechanism can be considered as a useful marker of overhanging strata that are known to be the origin of rockfall events.

The wide purple zone in the middle of the scarp marked with "3" in Fig A.7 cannot be trivially identified as humid or overhanging. Looking at the detailed geological studies of the upper scarp [54]-[53], we have identified this area as a freshly cleaved site of a large rockfall event. It is possible that freshly cleaved minerals present a different TIR spectral signature if compared to the weathered minerals that we considered up to now (including the argillaceous sandstone sample of the ECOSTRESS library). The evidence for changes in the TIR reflectance spectra of minerals with weathering can be found in the literature ([66] - [67] and [68]).
The structural characterization of the freshly cleaved surface section labelled with the number “3” in Figure A.7 a,b,c is provided in Figure A.7 d from [60] in the form of a point-cloud image difference between two acquisitions at distant times (3 years) with the algorithm Model to Model Cloud Comparison (M3C2) of ref [69]. This image highlighting the rock volumes lost and gained by different parts of the slope, the scarp sub-portion labelled with “3” in Figure A.7 has been identified as a freshly cleaved surface because of high volume loss. A similar identification has been made from terrestrial-laser-scanner (TLS) data in ref [54].

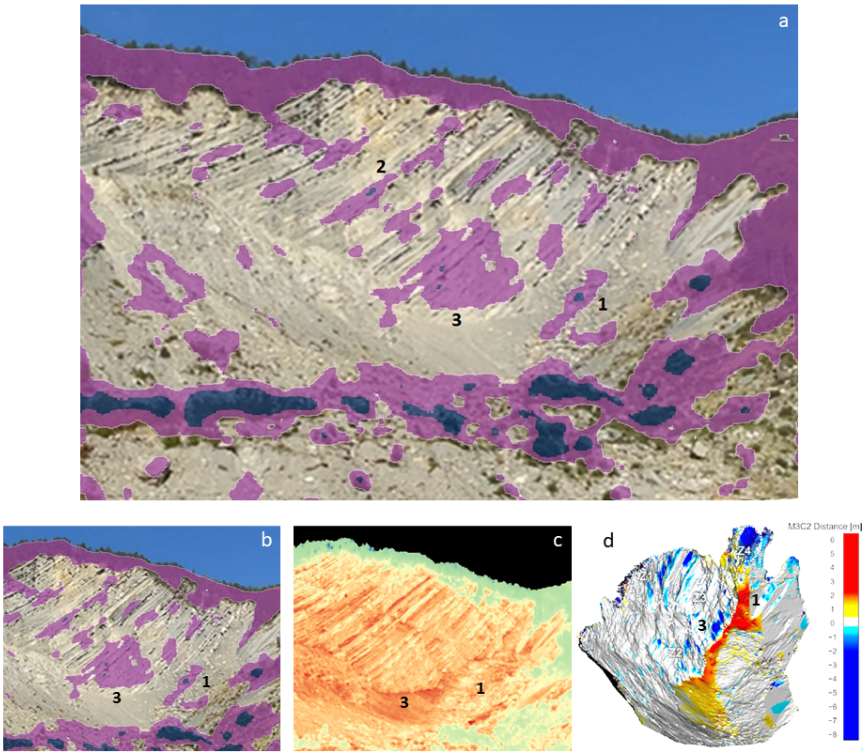

Figure A.7: *Visible image of the upper scarp with overlapping of multiscale segmentation map in false purple colour scale: only the two lowest levels are shown, while the two highest levels are set as a transparent layers. The result is an overlayed map of areas of the rocky scarp with anomalously low TIR signal, relevant for rockfall hazard monitoring. The lowest level in dark purple almost entirely corresponds to vegetation-covered areas, for which our physical model does not hold, and therefore it should not be considered as relevant areas, but rather simply as low TIR reflectance areas. b) zoom in of a detail in the image a), c) the sam FOV of image b in false colour in TIR range, d) a stroboscopic point-cloud performed by Unmanned Aerial Vehicle (UAV) photogrammetry, image from [60].*

Discussion and Conclusions

In this work we present a first study of an automatic remote-sensing method for monitoring landscapes. At present, our thermal imaging-based sensing method could be used for a preliminary screening and extensive evaluation of rocky scarps, with the aim of producing a potential hazard map; basing on this map, the hazard map can be complemented with local observation with different remote sensing techniques (e.g. laser scanner, unmanned aerial vehicle analysis etc.) and, if needed, with invasive techniques (e.g. stress sensors). To reach the goal of preliminary screening of rocky scarps by thermal imaging, it is essential to identify, emphasize and extract the informative features, to detect the possible artifacts, and the information-lacking background pixels. Our image segmentation algorithm has been designed to perform the above tasks.

We have applied an advanced image analysis technique, based on multiscale segmentation, to enhance the contrast of thermal infrared (TIR) images of the upper scarp of a landslide taken at a distance of 500 meters. We have found that the TIR image contrast analysis can highlight different physical mechansims behind TIR contrast: (i) a different local orientation of the rocky wall if compared to the average scarp surface orientation, due to the fact that reflectance will in general

dominate over emittance of rocky walls, but more so for properly oriented scarp sub-portions; (ii) a different grade of humidity of scarp sub-portions, because, according to our physical model of the optical constants in the TIR wavelength range, even a surface water layer of 100 micrometer thickness can decrease the TIR signal to an extent that can be observed by a high performance TIR camera; (iii) a different mineral content in scarp sub-portions, due to the high sensitivity of TIR spectral reflectance to the specific mineral oxidation state, which is related to the exposure time to weathering agents.

Appendix B

List of Research Outputs

Publications

- First author of a published article in date 2023/02/06 on the journal "MDPI, Remote sensing" entitled *Enhancing the thermal images of the upper scarp of the Poggio Baldi landslide (Italy) by physical modeling and image analysis.*
Abstract: We present new methods for physical interpretation and mathematical treatment of the imaging contrast observed in thermal images of the rocky upper scarp of the Poggio Baldi landslide (Italy), which is part of a natural laboratory. Exemplar thermal images have been acquired with a high-performance camera at a distance of around 500 m, in a geometry where reflection is expected to dominate over thermal emission. The digital pixel intensities have therefore been considered as wavelength-integrated infrared spectral reflectance, irrespective of the temperature scale loaded into the camera software. Sub-portions of the scarp producing a lower signal have been identified by a multiscale image segmentation algorithm and overlaid on the visible image to provide an interpretation for the different thermal imaging contrast mechanisms that may be exploited for landslide monitoring in the future.
The article (that is listed in bibliography as [52]) is available at the following link
https://doi.org/10.3390/rs15040907

Conferences and seminars

- First author of a poster contribution which summarizes the results of sections 4.2, 4.3 and 4.6 entitled *Vibrational Spectral Line Detection in GIS Environment for Mineral Mapping Applications of Hyperspectral Data of the PRISMA satellite* in the workshop "ShareScience: Multidisciplina e Trasferimento Tecnologico" of Sapienza university from 2024/02/15 to 2024/02/16 in Rome.

- First author of the oral contribution which summarizes the results of section 4.7 entitled *Change Detection analysis of Cultural and Landscape Heritage based on Multispectral and Hyperspectral remote sensing data and algorithm: the case of Appia Antica Park* of the "IMEKO International Conference On Metrology for Archeology and Cultural Heritage 2023" (MetroArcheo2023) from

2023/10/19 to 2023/10/21 in Rome.
Abstract: In remote sensing, multispectral and hyperspectral imaging are a valid method to analyze Earth Observation (EO) data. If multispectral imaging is largely used and well knew in EO and refers to the scomposition of the spectral range of the instruments onboard in few channels (typically from 6 to 12), hyperspectral imaging gains a greater spectral resolution and refers to obtain the spectrum for each pixel in the image, with the purpose of finding objects, identifying materials, or detecting processes through the structural analysis of the source (in SWIR range) or chemical behavior (in VIS range). In this work, a multispectral (NDVI) and hyperspectral (red edge slope) technique is used to perform a Change Detection (CD) on the vegetation of the Appia Antica Regional Park in Rome. The results show the benefits of these analyses in evaluating the state of landscape and in developing appropriate management projects.

- First author of the oral contribution which summarizes the results of sections 4.2, 4.3, 4.4, 4.5 and 4.6 within the context of hyperspectral satellite imaging in EO, entitled *Vibrational Spectral Line Detection in GIS environment for Mineral Mapping Applications of Hyperspectral Data of the PRISMA satellite* in the "International Geoscience and Remote Sensing Symposium 2023" (IGARSS 2023) from 2023/07/16 to 2023/07/21 in Pasadena, California (USA).
Abstract: We have developed a mathematical algorithm that calculates the discrete spectral derivative of the hyperspectral data of the satellite mission PRISMA in a Geographic Information System (GIS) environment. Vibrational fingerprints of minerals appear in the reflectance spectra as local "dips" centered at a resonance wavelength that characterizes some classes of minerals. The algorithm is then applied twice to each spectrum in each image datacube: once on the descending slope of a known vibrational feature, and once on the ascending slope. The sum of the absolute value of the two derivatives, obtained from a total of several tens of hyperspectral channels, is then combined in a vibrational line intensity score, which is then used to build mineral abundance maps. We apply the method to a mountain area, mapping freshly exposed gneiss under molten glaciers (vibrational resonance at 2222 nm), and to volcanic islands mapping rhyolite deposits on shores (resonance at 2104 nm).

- Second author of the poster contribution which summarizes the results of the article reported in Appendix A entitled *Enhancing the terrestrial thermal images of a landslide by physical modeling and image analysis* in the "International Workshop on High Resolution Thermal EO" from 2023/05/10 to 2023/05/12 in Rome.
Abstract: We present new methods for physical interpretation and mathematical treatment of the imaging contrast observed in thermal infrared (TIR) images of the rocky upper scarp of the Poggio Baldi landslide (Italy), which is part of a natural laboratory. Exemplar thermal images have been acquired with a high-performance camera at a distance around 500 meters, in a geometry where reflection is expected to dominate over thermal emission. The digital pixel intensities have therefore been considered as wavelength-integrated infrared spectral reflectance, irrespective of the temperature scale loaded into the camera software. Sub-portions of the scarp producing lower signal have been identified by a multiscale image segmentation algorithm and overlaid on the visible image to provide an interpretation for the different thermal imaging contrast mechanisms that may be exploited for landslide monitoring in the future. We have found that the TIR image contrast analysis

can highlight different physical mechanisms behind TIR contrast: (i) a different local orientation of the rocky wall if compared to the average scarp surface orientation, due to the fact that reflectance will in general dominate over emittance of rocky walls, but more so for properly oriented scarp sub-portions; (ii) a different grade of humidity of scarp sub-portions, because, according to our physical model of the optical constants in the TIR wavelength range, even a surface water layer of 100 micrometer thickness can decrease the TIR signal to an extent that can be observed by a high performance TIR camera; (iii) a different mineral content in scarp sub-portions, due to the high sensitivity of TIR spectral reflectance to the specific mineral oxidation state, which is related to the exposure time to weathering agents.

- First author of the oral contribution entitled *Hyperspectral Change Detection: New Way of Earth Observation Monitoring* at the "Workshop on Hyperspectral Image and Signal Processing: Evolution in Remote Sensing" (WHISPERS 2022) from 2022/09/13 to 2022/09/16 in Rome.
Abstract: In image analysis, Change Detection (CD) refers to the capability to identify the location and magnitude of changes between a couple of images acquired at different times, while Hyperspectral Imaging refers to obtain the spectrum for each pixel in the image of a scene, with the purpose of finding objects, identifying materials, or detecting processes through the structural analysis of the source. In this work, we want to show a possible result of Multivariate Alteration Detection (MAD) of the Orfeo Toolbox in the GIS framework in order to make a CD in the branch of the Hyperspectral Imaging.

Courses and Certifications

- *Beyond the visible — Imaging Spectroscopy for Agricultural Applications* (achieved on date 2023/02/24) and *Beyond the visible — Introduction to Hyperspectral Remote Sensing* (achieved in date 2022/03/04) are courses provided by HyperEDU, an online learning initiative for hyperspectral remote sensing that is developed as part of the EnMAP mission science program.

- *Deep Learning Methods in Physics* (achieved on December 2021): a course for PhD students provided by professor Stefano Giagu.

-*Condensed Matter Physics* (achieved on December 2021): a course for Master students provided by professor Antonio Polimeni.

Refereeing

- Referee of the article published in date 2023/12/20 on the journal "Elsevier, Engineering Geology" entitled *Dissolution feature differences of carbonate rock within hydro-fluctuation belt located in the Three Gorges Reservoir Area.*
Abstract: The stability of geological environment in the Three Gorges Reservoir Area (TGRA) has experienced severe challenges due to the 30 m hydro-fluctuation belt (HFB). The vertical dissolution features vary with the mechanism of water and rock interaction. Although dissolution features have been adequately explained by physical and mechanical parameters, the characterization of

chemical changes in dissolution is vital but frequently neglected information. For this purpose, the hyperspectral characteristics and mineralogical composition variation of rock HFB in different areas of the Triassic Daye Formation are tested to elucidate the dissolution behaviors. Then, the deterioration degree of dissolution is quantified by a multi-objective data integration based on Random Forest Regression (RFR) model. The spatial distribution of dissolution and the seasonal deterioration characteristics are identified depending on the spectral response of carbonate. Specifically, the dissolution degree is proportional to elevation, and inverse to the bedding angle at 0–40° in the investigated stratum. Combined with the hydrological characteristics of the study area, the corresponding regional phenomena can be distinguished as reservoir water dominated, rainfall dominated, and coupled action. Affected by reservoir water and acid rainfall, the HFB may deteriorate most severely from January to April. In addition, the contribution of RFR model integrated spectral and geometric data to the deterioration evaluation of the HFB is discussed, which can effectively enhance the identification of rock mass boundary in a single spectral data model. Thus, these results are conducive to the rapid evaluation of regional geomorphological characteristics and the monitoring of geological disasters in the TGRA.
The article is available at the following link
https://doi.org/10.1016/j.enggeo.2023.107362

- Referee of the article published in date 2022/09/25 on the journal "IET Image Processing" entitled *Hybrid Network Model Based on 3D Convolutional Neural Network and Scalable Graph Convolutional Network for Hyperspectral Image Classification.*
Abstract: Hyperspectral images (HSIs) contain hundreds of continuous spectral bands and are rich in spectral-spatial information. In terms of HSIs' classification, traditional convolutional neural networks (CNNs) extract features based on HSI's spectral-spatial information through 2D convolution. However, 2D convolution extracts features in 2D plane without considering the relationships between spectral bands, which inevitably leads to insufficient feature extraction. 3D convolutional neural networks (3DCNNs) take account of the correlations among spectral bands and outperform 2D convolutional networks in feature extraction, but the computational cost is rather expensive. To address the above problem, a light-weight three-layer 3D convolutional network Module (3D-M) for HSIs' spectral-spatial feature extraction is proposed. Another challenge is that neither 2D convolution nor 3D convolution utilizes the structural information inherent in the data. Graph convolution networks (GCNs) can model and utilize such information through the similarity matrix, also known as adjacency matrix. However, traditional GCNs cannot handle large-scale data because they construct an adjacency matrix on all data, which results in high computational complexity and large storage requirement. To conquer this challenge, this article proposes a batch-graph strategy on which a scalable GCN is developed. Finally, a hybrid network model (HNM) based on the proposed light-weight 3D-M and scalable GCN is presented. HNM extracts spectral-spatial features of HSIs with low computational complexity through the light-weight 3D convolution network and leverages the structural information in data via the scalable GCN. The experimental results on three public datasets with different sizes demonstrate that the proposed HNM produces better classification results than other state-of-the-art hyperspectral images classification models in terms of overall accuracy (OA), average accuracy (AA) and kappa coefficient (Kappa).
The article is available at the following link

https://doi.org/10.1049/ipr2.12632

Bibliography

[1] D.P. Roy, M.A. Wulder, T.R. Loveland, C.E. Woodcock, R.G. Allen, M.C. Anderson, D. Helder, J.R. Irons, D.M. Johnson, R. Kennedy, T.A. Scambos, C.B. Schaaf, J.R. Schott, Y. Sheng, E.F. Vermote, A.S. Belward, R. Bindschadler, W.B. Cohen, F. Gao, J.D. Hipple, P. Hostert, J. Huntington, C.O. Justice, A. Kilic, V. Kovalskyy, Z.P. Lee, L. Lymburner, J.G. Masek, J. McCorkel, Y. Shuai, R. Trezza, J. Vogelmann, R.H. Wynne, and Z. Zhu. Landsat-8: Science and product vision for terrestrial global change research. *Remote Sensing of Environment*, 145: 154–172, 2014.

[2] F. Spoto, S. Omar, P. Laberinti, P. Martimort, V. Fernandez, O. Colin, B. Hoersch, and A. Meygret. Overview of sentinel-2. *International Geoscience and Remote Sensing Symposium*, pages 1707–1710, 2012.

[3] O. Kurniawan and E. Li. Study of a single coaxial silicon nanowire for on-chip integrated photovoltaic application. *International Symposium on Integrated Circuits*, pages 314–317, 2009.

[4] H.H. Adler and P.F. Kerr. Infrared study of aragonite and calcite. *American Mineralogist*, 47.

[5] S. J. Gaffey. Spectral reflectance of-carbonate minerals in the visible and near infrared (0.35-2.55 microns): calcite, aragonite, and dolomite. *American Mineralogist*, 71:151–162, 1986.

[6] J.W. Zeller, H. Efstathiadis, G. Bhowmik, P. Haldar, N.K. Dhar, J. Lewis, P. Wijewarnasuriya, Y.R. Puri, and A.K. Sood. Development of ge pin photodetectors on 300 mm si wafers for near-infrared sensing. *International Journal of Engineering Research and Technology*, 8:23–33, 2015.

[7] G. Vane, A.F.H. Goetz, and J.B. Wellman. Airborne imaging spectrometer: A new tool for remote sensing. *Transactions on Geoscience and Remote Sensing*, 6:546–549, 1984.

[8] G. Vane, R.O. Green, T.G. Chrien, H.T. Enmark, E.G. Hansen, and W.M. Porter. The airborne visible/infrared imaging spectrometer (AVIRIS). *Remote Sensing of Environment*, 44:127–143, 1993.

[9] A.F.H. Goetz. Three decades of hyperspectral remote sensing of the earth: A personal view. *Remote Sensing of Environment*, 113:1707–1710, 2009.

[10] J. Pearlman, S. Carman, C. Segal, P. Jarecke, P. Clancy, and W. Browne. Overview of the hyperion imaging spectrometer for the nasa eo-1 mission. *International Geoscience and Remote Sensing Symposium*, 7:036–3038, 2001.

[11] C. Laukamp. Short wave infrared functional groups of rockforming minerals. *CSIRO*, EP115222, 2011.

[12] S. Marinez-Alonso, J.R. Rustad, and A.F.H. Goetz. Ab initio quantum mechanical modeling of infrared vibrational frequencies of the oh group in dioctahedral phyllosilicates. part i: Methods, results and comparison to experimental data. *American Mineralogist*, 87:1215–1223, 2022.

[13] R.G. Burns and R.G.J. Strens. Infrared study of the hydroxyl bands in clinoamphiboles. *Remote Sensing of Environment*, 153:890 – 892, 1966.

[14] G.R. Hunt. Spectral signatures of particulate minerals in the visible and near infrared. *Geophysics*, 42:501–513, 1977.

[15] G.R. Hunt and J.W. Salisbury. Visible and near-infrared spectra of minerals and rocks—I. silicate minerals. *Modern Geology*, 1:283, 1970.

[16] G.R. Hunt, J.W. Salisbury, and C.J. Lehnoff. Visible and near infrared spectra of minerals and rocks: III, oxides and oxyhydroxides. *Modern Geology*, 2:195–205, 1971.

[17] G.R. Hunt, J.W. Salisbury, and C.J Lehnoff. Visible and near-infrared spectra of minerals and rocks: V. halides, phosphates, arsenates, vanadates and borates. *Modern Geology*, 3:121–132, 1972.

[18] R.N. Clark. Spectral properties of mixtures of montmorillonite and dark carbon grains implications for remote sensing minerals containing chemically and physically adsorbed water. *Journal Of Geophysical Research*, 88:10635–10644, 1983.

[19] R.B. Singer. Near-infrared spectral reflectance of mineral mixtures: Systematic combinations of pyroxenes, olivine, and iron oxides. *Journal Of Geophysical Research*, 86:7967–7982, 1981.

[20] P.E. Johnson. A semiempirical method for analysis of the reflectance spectra of binary mineral mixtures. *Journal Of Geophysical Research*, 88:3245–3578, 1983.

[21] R.N. Clark and P.G. Lucey. Spectral properties of ice-particulate mixtures and implications for remote sensing: 1. intimate mixtures. *Journal Of Geophysical Research*, 89:5669–6354, 1984.

[22] R.N. Clark. The spectral reflectance of water-mineral mixtures at low temperatures. *Journal Of Geophysical Research*, 86:2495–3132, 1981.

[23] R.N. Clark and T.L. Roush. Reflectance spectroscopy: Quantitative analysis techniques for remote sensing applications. *Journal Of Geophysical Research*, 89:6329–6340, 1984.

[24] R. G. J. Strens. *The Common Chain, Ribbon, and Ring Silicates.* Mineralogical Society of Great Britain and Ireland, 1974.

[25] W. Vedder. Correlations between infrared spectrum and chemical composition of mica. *American Mineralogist*, 49:736–768, 1964.

[26] A. Meunier. Clays. *Springer Science & Business Media*, 2005.

[27] R.L. Frost and U. Johansson. Combination bands in the infrared spectroscopy of kaolins—a drift spectroscopic study. *Clays and Clay Minerals*, 46:466 – 477, 1998.

[28] T.J. Cudahy and E.R. Ramanaidou. Measurement of the hematite:goethite ratio using field visible and near-infrared reflectance spectrometry in channel iron deposits, western australia. *Australian Journal of Earth Sciences*, 44:411–420, 1997.

[29] J.K. Crowley and N. Vergo. Near-infrared reflectance spectra of mixtures of kaolin-group minerals: use in clay mineral studies. *Clays and Clay Minerals*, 36:310 – 316, 1988.

[30] J.L. Post and P.N. Noble. The near-infrared combination band frequencies of dioctahedral smectites, micas, and illites. *Clays and Clay Minerals*, 41:639 – 644, 1993.

[31] R.N. . Clark, T.V.V. King, M. Klejwa, and G.A. Swayze. High spectral resolution reflectance spectroscopy of minerals. *Journal Of Geophysical Research*, 95:12653–12680, 1995.

[32] P. A. van Aken and B. Liebscher. Quantification of ferrous/ferric ratios in minerals: new evaluation schemes of fe l23electron energy-loss near-edge spectra. *Physics and Chemistry of Minerals*, 29:188 – 200, 2002.

[33] K. Langer and M. Raith. Infrared spectra of al-fe (iii)-epidotes and zoisites, ca2 (al1-p fe3+ p) al2o (oh)[si2o7][sio4]. *American Mineralogist: Journal of Earth and Planetary Materials*, 59: 1249–1258, 1974.

[34] L. H. Roach, J.F. Mustard, G. Swayze, R.E. Milliken, J.L. Bishop, S. L. Murchie, and K. Lichtenberg. Hydrated mineral stratigraphy of ius chasma, valles marineris. *Icarus*, 206:253–268, 2010.

[35] C. Laukamp, K.A. Termin, B. Pejcic, M. Haest, and T. Cudahy. Vibrational spectroscopy of calcic amphiboles–applications for exploration and mining. *European Journal of Mineralogy*, 24:863–878, 2012.

[36] S.J. Gaffey. Spectral reflectance of carbonate minerals in the visible and near infrared (0.35-2.55 microns). and calcite, aragonite, and dolomite. *American Mineralogist*, 71:151–162, 1986.

[37] E. A. Cloutis, F. C. Hawthorne, S. A. Mertzman, K. Krenn, M. A. Craig, D. Marcino, and F. Vilas. Detection and discrimination of sulfate minerals using reflectance spectroscopy. *Icarus*, 184:121–157, 2006.

[38] M. J. Jeon, S. R. Lee, E. Kim, S. B. Lim, and S. W. Choi. Launch and early operation results of kompsat-3a. *International Conference on Space Operations*, 113:2394, 2016.

[39] V. Laparra and R. Santos-Rodrıguez. Spatial/spectral information trade-off in hyperspectral images. *2015 IEEE International Geoscience and Remote Sensing Symposium (IGARSS)*, pages 1124–1127, 2015.

[40] C.E. Shannon. A mathematical theory of communication. *The Bell System Technical Journal*, 27:379–423, 623–656, 1948.

[41] S. Jimenez and J. Malo. The role of spatial information in disentangling the irradiance reflectance transmittance ambiguity. *IEEE Transactions on Geoscience and Remote Sensing*, 52, 2014.

[42] M. Bethge. Factorial coding of natural images: how effective are linear models in removing higher-order dependencies? *J. Opt. Soc. Am. A*, 23:1253–1268, 2006.

[43] B. C. Smith. Fundamentals of fourier transform infrared spectroscopy. *CRC press*, 2011.

[44] P. R. Grifiths and J. A De Haseth. Fourier transform infrared spectrometry. *John Wiley and SonsJohn Wiley and Sons*, 2007.

[45] L. Guanter, I. Irakulis-Loitxate, J. Gorroño, E. Sánchez-García, D.H. Cusworth, D.J. Varon, S. Cogliati, and R. Colombo. Mapping methane point emissions with the prisma spaceborne imaging spectrometer. *Remote Sensing of Environment*, 265:112671, 2021.

[46] G. M. Gandhi, S. Parthiban, N. Thummalu, and A. Christy. Ndvi: Vegetation change detection using remote sensing and gis – a case study of vellore district. *Procedia Computer Science*, 57: 1199–1210, 2015.

[47] D. Phiri, S. Simwanda, M. andSalekin, V. R. Nyirenda, Y. Murayama, and M. Ranagalage. Sentinel-2 data for land cover/use mapping: A review. *Remote Sensing*, 12:14, 2020.

[48] I.D. Negula, C. Moise, C.E. Mihalache, and A. Badea. Satellite remote sensing for the analysis of the micia and germisara archaeological sites. *MDPI Remote Sensing*, 12, 2020.

[49] A. Agapiou. Estimating proportion of vegetation cover at the vicinity of archaeological sites using sentinel-1 and-2 data, supplemented by crowdsourced openstreetmap geodata. *Applied Sciences*, 10:4764, 2020.

[50] M. Pepe, L. Pompilio, L. Ranghetti, F. Nutini, and M. Boschetti. Mapping spatial distribution of crop residues using prisma satellite imaging spectroscopy. *European Journal of Remote Sensing*, 56:2122872, 2023.

[51] M. Avian, C. Bauer, M. Schlögl, B. Widhalm, K. Gutjahr, M. Paster, C. Hauer, M. Friebenbichler, A. Neureiter, G. Weyss, P. Flödl, G. Seier, and W. Sulzer. The status of earth observation techniques in monitoring high mountain environments at the example of pasterze glacier, austria: Data, methods, accuracies, processes, and scales. *Remote Sensing*, 12, 2020.

[52] A. Massi, M. Ortolani, D. Vitulano, V. Bruni, and P. Mazzanti. Enhancing the thermal images of the upper scarp of the poggio baldi landslide (italy) by physical modeling and image analysis. *Remote Sensing*, 2023.

[53] S. Romeo, A. Cosentino, F. Giani, G. Mastrantoni, and P. Mazzanti. Combining ground based remote sensing tools for rockfalls assessment and monitoring: The poggio baldi landslide natural laboratory. *Sensors*, 21:2632, 2021.

[54] P. Mazzanti, P. Caporossi, A. Brunetti, F.I. Mohammadi, and F. Bozzano. Short-term geomorphological evolution of the poggiobaldi landslide upper scarp via 3d change detection. *Landslides*, 18:2367–2381, 2021.

[55] H. Ochiai, Y. Okada, G. Furuya, Y. Okura, T. Matsui, T. Sammori, T. Terajima, and K. Sassa. A fluidized landslide on a natural slope by artificial rainfall. *Landslides*, 1:211–219, 2004.

[56] Y.J. Liu, Y.Y. Chiu, T. Frank, C. Tsai, and S.C. Chen. Analysis of landslide occurrence time via rainfall intensity and soil water index ternary diagram. *Landslides*, 19:2823–2837, 2022.

[57] S.K. Kurinec. Complementary metal oxide semiconductor field effect transistors. *Encyclopedia of Materials: Science and Technology*, 1343, 2001.

[58] J. D. Vincent, S. Hodges, J. Vampola, M. Stegall, and G. Pierce. Fundamentals of infrared and visible detector operation and testing. *John Wiley and Sons*, pages 191–236, 2015.

[59] C. . Esposito, E. Di Luzio, M. Baleani, F. Troiani, M. Della Seta, F. Bozzano, and P. Mazzanti. Fold architecture predisposing deep-seated gravitational slope deformations within a flysch sequence in the northern apennines (italy). *Geomorphology*, 380:107629, 2021.

[60] C. Robiati, G. Mastrantoni, M. Francioni, M. Eyre, J. Coggan, , and P. Mazzanti. Contribution of high-resolution virtual outcrop models for the definition of rockfall activity and associated hazard modelling. *Land*, 12:191, 2023.

[61] S. Winkler. Temporal dynamic analysis of a mountain ecosystem based on multi-source and multi-scale remote sensing data. *Digital Video Quality: Vision Models and Metrics*, 2005.

[62] S. Mallat. A wavelet tour of signal processing. *Elsevier*, 1999.

[63] P. I. Burt and E. H. Adelson. The laplacian pyramid as a compact image code. *IEEE Trans Commun.*, pages 532–540, 1983.

[64] S. Mallat. Multiresolution approximations and wavelet orthonormal bases of l2(r). *Trans. Amex Math. Soc.*, pages 69–87, 1989.

[65] R. C. Gonzalez. Digital image processing. *Richard E. Woods (4th ed.). Pearson, New York*, page 138–140, 2018.

[66] R. H. Lara, M. Mallet, M. Dossot, and M.A. González-Lozano. An experimental study of iron sulfides weathering under simulated calcareous soil conditions. *Environmental Earth Sciences*, 73:1849, 2014.

[67] J. R. Michalski, M. D. Kraft, T. G. Sharp, L. B. Williams, and P.R. Christensen. Emission spectroscopy of clay minerals and evidence for poorly crystalline aluminosilicates on mars from thermal emission spectrometer data. *Journal Of Geophysical Research*, 111:E03004, 2006.

[68] J. R. Michalski, S. J. Reynolds, T.G. Sharp, and P.R. Christensen. Thermal infrared analysis of weathered granitic rock compositions in the sacaton mountains, arizona: Implications for petrologic classifications from thermal infrared remote-sensing data. *Journal Of Geophysical Research*, 109:E03007, 2004.

[69] D. Lague, N. Brodu, and J. Leroux. Accurate 3d comparison of complex topography with terrestrial laser scanner: Application to the rangitikei canyon (n-z). *Journal of Photogrammetry and Remote Sensing*, 82:10–26, 2023.

Ringraziamenti

Sono molte le persone che dovrei ringraziare in questo documento che rappresenta il culmine di tre anni di crescita e lavoro come mai ho sperimentato finora.

Prima di tutto vorrei ringraziare le persone che mi hanno sostenuto da molto prima di questo dottorato e che non hanno fatto venir meno il loro supporto, insostituibile, neanche in questi ultimi tre anni.
Parlo ovviamente dei miei genitori, che mi hanno aiutato notevolmente in questo periodo di grandi cambiamenti (tanto nell'abitazione quanto nel mondo del lavoro e della ricerca) con la pazienza e l'amore che mi hanno sempre dimostrato, e dei miei due migliori amici che sono da sempre presenti sia per festeggiare i successi quanto per consolarmi nelle sconfitte. Il contributo di queste quattro persone è stato fondamentale per trovare le forze per affrontare questo percorso.

Ringrazio ovviamente anche la mia ragazza che oltre alla mia personalità testarda e a volte troppo rigida ha dovuto anche sopportare i miei frequenti momenti di euforia e sconforto scanditi da ogni tappa del dottorato. Il suo è stato un contributo costante ed è stato rifugio e conforto al termine di ogni giornata di lavoro.

Ringrazio infine, prima di passare alle persone che sono entrate nella mia vita proprio grazie al dottorato, gli amici che il vortice del tempo non ha spazzato via. Non ne sono rimasti moltissimi, ma quelli che sono rimasti sono persone su cui posso sempre contare e sono per me molto preziosi. Il confronto con il loro punto di vista in aree di lavoro ed esperienze diverse, ma a volte simili, mi ha permesso di non fossilizzarmi, anzi immobilizzarmi, sulle difficoltà che ho incontrato in questi tre anni e di condividere con i loro successi i miei.

In questa seconda parte di ringraziamenti, voglio ringraziare le meravigliose persone che ho conosciuto durante il mio dottorato e che si suddividono nei tre gruppi di: NHAZCA, dipartimento di scienze della terra e Infrared Spectroscopy Lab (che abbrevierò come IRS). Mi ritengo davvero molto fortunato a riguardo perché posso dire che in tutti e tre gli ambienti ho sempre trovato un'accoglienza davvero calorosa nonostante provenissi da un mondo molto differente che è quello in astrofisica dello studio dell'universo a larga scala. In particolare:

vorrei ringraziare tutti i nhazchiani perché mi hanno da subito accolto nella loro famiglia aziendale tanto nel lavoro, con gli innumerevoli progetti in cui mi hanno coinvolto (ma *mai* abbandonato), quanto al di fuori, nei team building e nelle altre occasioni di ritrovo che conserverò con piacere per tutta la vita. A loro devo molto e non parlo solo delle conoscenze che mi hanno generosamente fornito sul settore privato e su tutto quello che c'è da sapere su un mondo che mi era totalmente sconosciuto prima del dottorato.

Vorrei ringraziare poi i colleghi del dipartimento di scienze della terra di Sapienza con cui ho collaborato e collaboro tutt'ora su molti progetti. Anche da loro ho appreso un'enorme quantità di conoscenze che non avrei mai studiato se non avessi intrapreso questo dottorato ed è altrettanto

inestimabile il valore dei momenti spesi con loro al di fuori del lavoro come ad esempio la festa di Santa Barbara del loro dipartimento nel quale mi hanno accolto come uno di loro (ed è solo uno dei tanti esempi dei meravigliosi momenti che ricordo con grande piacere).

Infine ringrazio tutte le persone dell'IRS che sono state presenti nel mio dottorato. La loro presenza è stata principale in questi tre anni e a loro sono molto grato per l'accoglienza ma soprattutto per la pazienza nell'insegnarmi il mondo della spettroscopia che non conoscevo prima di intraprendere il dottorato. Di questi momenti altamente formativi (e che sono sicuro mi accompagneranno anche dopo il dottorato) voglio anche mantenere il ricordo dei pranzi sul prato dell'ateneo, del German Thursday e di tutti gli altri momenti, a volte davvero incredibili, che hanno costellato questi tre anni.

Un'ultima persona voglio ringraziare in particolare, la più importante ai fini della stesura di questo lavoro. Il mio relatore. A lui, la mia guida, dedico questo lavoro.
Senza i suoi insegnamenti, consigli, suggerimenti, aiuti teorici, aiuti pratici, incoraggiamenti, elogi e giusti rimproveri che hanno costellato il mio dottorato, permettendomi di crescere, non credo che avrei potuto produrre da solo i risultati di questo documento e voglio dedicargli questo spazio personale all'interno di questa tesi:

Vorrei ringraziare Michele, la persona che mi ha guidato sapientemente in questo lungo viaggio in cui per la prima volta ho smesso di studiare su un libro per essere io stesso il libro da studiare

Roma, Aprile 2024